8423728

Moghadam, Mahmoud Mobara

PARTICLE DEPOSITION DUE TO POINT OR LINE SOURCE DIFFUSION

Iowa State University PH.D. 1984

University
Microfilms
International 300 N. Zeeb Road, Ann Arbor, MI 48106

PLEASE NOTE:

In all cases this material has been filmed in the best possible way from the available copy. Problems encountered with this document have been identified here with a check mark __✓__.

1. Glossy photographs or pages _____
2. Colored illustrations, paper or print _____
3. Photographs with dark background __✓__
4. Illustrations are poor copy _____
5. Pages with black marks, not original copy _____
6. Print shows through as there is text on both sides of page _____
7. Indistinct, broken or small print on several pages __✓__
8. Print exceeds margin requirements _____
9. Tightly bound copy with print lost in spine _____
10. Computer printout pages with indistinct print _____
11. Page(s) _____ lacking when material received, and not available from school or author.
12. Page(s) _____ seem to be missing in numbering only as text follows.
13. Two pages numbered _____. Text follows.
14. Curling and wrinkled pages _____
15. Other _____

Particle deposition due to point or line source diffusion

by

Mahmoud Mobara Moghadam

A Dissertation Submitted to the
Graduate Faculty in Partial Fulfillment of the
Requirements for the Degree of
DOCTOR OF PHILOSOPHY

Major: Aerospace Engineering

Approved:

Signature was redacted for privacy.

In Charge of Major Work

Signature was redacted for privacy.

For the Major Department

Signature was redacted for privacy.

For the Graduate College

Iowa State University
Ames, Iowa

1984

TABLE OF CONTENTS

LIST OF SYMBOLS

A_{test}	Cross sectional area of the test section
A_1	Numberical constant
A	Empirical constant
B_1	Numerical constant
C	Empirical constant
C_1	Particle concentration in mass per unit volume
D_1	Numerical constant
D	Particle diameter
$\bar{D}$	Average particle diameter
e	Coefficient of restitution
F	Conversion factor (3.727×10^{-2} μg/#)
F_1	Conversion factor (2.683x10 #/μg)
g	Gravitational acceleration
H	Full scale height
h	Model scale height
$\vec{i}$	Unit vector in the x direction
$\vec{k}$	Unit vector in the z direction
k_x	Longitudinal coefficient of diffusivity
k_y	Lateral coefficient of diffusivity
k_z	Vertical coefficient of diffusivity
K	Von Karman constant = 0.4
L	Full scale length
L*	Monin-Obukhov length or atmospheric stability parameter

$L_{IT-Trap}$	Length of the test section
L_1	Particulate characteristic flight path length
N	Number of particles per square millimeter field of view
N_A	Average number of lateral particles per square millimeter
N_L	Number of particles per millimeter longitudinal position
N_{NU}	Number of particles per square millimeter determined numerically
$N'(x)$	Number of particles per unit longitudinal distance
Q	Source strength
Q_{AS}	Area source strength
Q_{LS}	Line source strength (per unit length) determined from the total number of particles
Q_{LSM}	Line source strength determined from the total mass loss of the source
Q_{PS}	Point source strength determined from the total number of particles
Q_{PSM}	Point source strength determined from the total mass loss of the source
t	Time
u	Lateral component of the wind velocity
V_∞	Free stream velocity
V	Longitudinal component of the wind velocity
V_*	Friction speed
V_D	Deposition velocity
V_f	Particle terminal speed
V_R	Reference wind speed

$V_R(H)$	Reference wind speed at height H
$V_R(Z)$	Reference wind speed as a function of height
V_{*t}	Particle threshold friction speed
W	Vertical component of the wind velocity
$\overline{X}$	Longitudinal position of the obstacles
$\overline{Y}$	Lateral position of the obstacles
Z_0	Roughness length
α	Empirical constant
ΔT	Run time of each test
ΔW_E	Mass loss of each source
ν	Air kinematic viscosity
ρ	Particle density
ρ_A	Air density
τ	Friction drag
#	Number of particles

CHAPTER I. INTRODUCTION

Particles of sufficiently small size become airborne when exposed to a turbulent wind of sufficient strength. The wind transport of small particles is, in a general sense, a cause of numerous environmental problems. Air and water pollution via gaseous and smoke release from industrial areas, wind erosion of deserts and agricultural areas, pollution due to coal particle transportation and drifting of sand and snow on roadways around the world are a few examples.

The goal of this research is to provide empirical particle deposition distributions for line and point source geometries due to emission from sources containing small particles, and then to determine source strength magnitudes by comparison with numerical solutions. Numerical schemes have been shown to be successful when the topographic geometry downstream of the source is simple. However, the abilities of such schemes to solve practical problems are limited. The major difficulty is due to the effect of complex topographic obstructions within the atmospheric boundary layer on the wind and resulting turbulent diffusion of these topographic obstructions. Mathematical representation of wind in the vicinity of obstructions of various shapes and sizes (i.e., trees, buildings, bushes, etc.) is necessary for further steps in the development of the numerical methods. The importance of experimental technique is underscored by

the difficulty of this mathematical representation as well as problems with computer storage capacity.

On the other hand, in order to predict particle concentration and the total mass loss due to wind erosion of a source, the source strength variation with wind speed has to be known (1,2). Previous studies have indicated that source strength variation with wind speed follows a power law (i.e., the source strength has been shown to vary as the wind speed raised to an exponent with a value between one and nine). From purely dimensional consideration, however, the source strength should vary with the cube of the wind speed. The discrepancy may be due to an improper mathematical representation of the source strength.

The purpose of the present study is to achieve the following: (1) to show that the cubic power law relation between source strength and wind speed holds but that the equation is more complicated than a simple power law; (2) it is desirable to demonstrate the ability of the numerical methods compared with the experimental concentration predictions due to diffusion from known sources over flat and complicated regions (unfortunately due to time limitations the numerical concentration diagrams over complicated regions, including a two and a three-dimensional obstructions were not completed); (3) qualitative comparisons are made with available field and experimental data (concentration is plotted as a function

of down wind and lateral distances over flat and complicated regions).

An experimental investigation has been conducted at Iowa State University in the open circuit wind tunnel of the Aerospace Engineering Department. A point source and a two-dimensional line source were utilized as scale models of areas containing small particles. The effects of two-dimensional and three-dimensional obstructions on the down wind surface deposition of lycopodium spores due to diffusion from the sources were investigated. The experiments were performed with and without the obstructions at different wind speeds during various time durations. The isolines of constant concentration as well as the lateral and the longitudinal variations of concentration are presented for all cases. Using the correlation between strength and concentration and from direct measurements of the total mass loss, a relation between source strength and friction speed is presented. It is shown that source strength varies as a cube of friction speed times a nondimensional exponential function of friction over threshold speed (i.e., $Q \alpha \frac{\rho V_*^3}{g} f(V_*/V_{*_T})$). This presentation of source strength with wind speed seems to fit the present data and also correlates well with previously available field and experimental results. The form of the equation obviates the necessity for a

proportionality coefficient which is dimensional (contrary to many previous results).

A numerical scheme (Crank-Nicolson) was used to solve the diffusion equation.[1] When obstructions are not present, some qualitative comparison exists between the numerical and the experimental results. On the other hand, due to the complexity of wind profile in the vicinity of the obstructions and due to time limitations, no numerical results will be presented for cases when obstructions were tested. However, the wind profiles in the vicinity of the obstructions were measured for various upstream, downstream, and lateral distances, using hot-wire anemometry. The wind profiles are documented here for future studies.

Related Problems

Increasing air pollution due to expansion of industry during the late twenties started a world wide concern. Air contaminated with chemical pollutants capable of being transported to distances as far as ten kilometers and of depositing toxic materials on the surface was not considered healthy to life and the living. Something had to be done! Soon, research

---

[1]Numerical analysis presented in this dissertation were completed by Chin-Shun Lin of Iowa State University, Ames, Iowa, as a part of his Ph.D. research.

funds were provided for extensive investigation into the cause and the means of reducing atmospheric pollution. Parallel to these studies, interest was shown in understanding the physics of large particle transportation by the wind, such as those found in deserts, in coal dust piles, mine tailings, etc.

Since the mid-thirties many papers have been published on the subject. The success of the mathematical models used (3-13) were usually subject to the accuracy of experimental and environmental data such as, velocity profile, turbulent stability parameters, source strength, source height and density of the emitted substance, depending on the method in hand. Without the help of fast digital computers, it was not possible to solve the diffusion equation. As a result, many empirical solutions were derived for special cases such as smoke concentration downwind of a factory (3). With the aid of fast numerical computation, efforts in solving problems such as smoke diffusion over a surface of irregular configuration have met with good success (14). Yet, many practical problems associated with diffusion are only explored through an experimental approach. One difficulty is of course due to the complex flow in the three-dimensional space in and around various obstructions of different shapes and sizes.

The mathematical models representing gaseous point and line source diffusion are really a limiting case of particles

with no net inertial force due to gravity. Modification of these models with nonzero gravity constraints have proven to be useful in theoretical particle concentration predictions (1,15-17).

As mentioned before, the problems associated with atmospheric turbulent diffusion are not limited to polluting gases. Due to the interaction of small eddies of turbulent wind with the surface of loose particulates, a lifting force will be exerted on the most exposed particles. The particles are then either lifted up to higher levels and are kept aloft for long periods of time (particles in suspension), or they will be dropped along their flight paths at relatively calculable distances downwind of their original location (particles in saltation). The third type of motion which is really not a direct result of diffusion, but rather a direct consequence of saltation, is called creep (18). Creep is the motion along the surface of larger particles which earn their forward momentum by impact from falling particles in saltation (18).

The problems which are encountered due to particle drift and transport by wind could be categorized by the type of particles. Sand and dust transportation are the main reason for desert erosion and visibility difficulties (18-20) as well as pollution (21). Snow drifting on roads and highways

around the world is another example (22,23). Coal particles blown by the wind from power plant storage piles to nearby towns and cities is another cause of pollution (1,2,24). Recently, attention has been given to radio active diffusion from dumping sites in and around deserts (25). In another paper, an experimental study was carried on into better understanding of pollen deposition to vegetated surfaces due to atmospheric turbulence (26). The research associated with the subject of diffusion is not limited to the earths atmosphere, but is also of interest on other planets (27).

Previous Work

The entrainment rate or source strength of a two-dimensional tray (length = 34.0 cm, height = 2.24 cm) containing coal particles was obtained experimentally as a function of wind speed (1). Figure 2 of reference 1 shows that source strength is strongly dependent on wind speed. For low humidity the source strength from the same figure could be approximated as

$$Q_{AS} = 0.813\ V_R^{6.35}\ \frac{\mu g}{m^2\text{-sec}}\ . \qquad (1)$$

Chemical crusting on the surface of the coal in the same source decreased the source strength by a factor of 10^3 to $10^4\ \frac{\mu g}{m^2\text{-sec}}$ (1). The relationship between Q_{AS} and V_R in the case of the crusty surface was not presented, however.

By modification of a heavy gas model to compensate for any coal particle fallout due to gravity Smit et al. (1) compared experimental vertical distribution of relative concentration fifty meters downwind from the center line of a source. The results (1) showed good agreement between the experimental and the theoretical concentration predictions in which relative concentration dropped from 0.04 at a height of 5.0 meters to 1.0 at ground level.

Using a high volume air sampler, the concentration of zinc sulfide around the stockpiles at Budelco Budel, the Netherlands, were compared with the predicted values of concentration (1) as shown in Figure 1. It can be seen that there is some agreement between the two sets of predictions.

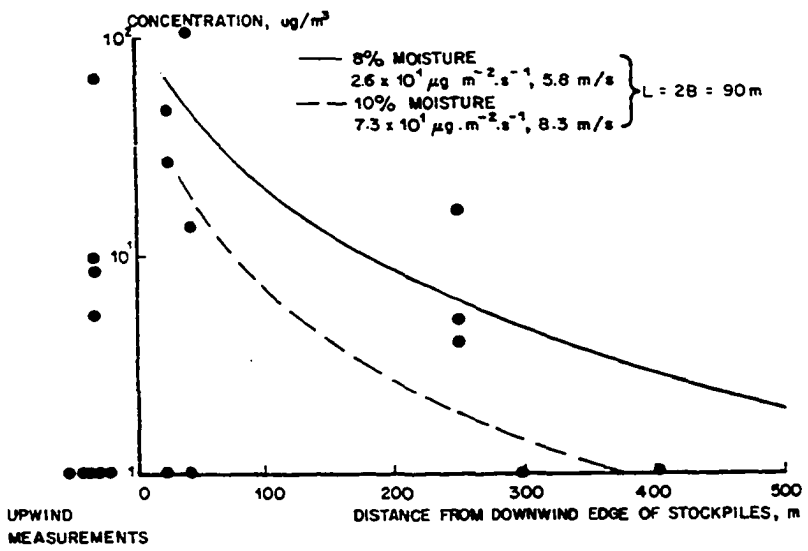

Figure 1. Measured and predicted zinc sulfide concentration (Smit et al. (1))

The discrepancy can probably be explained by the degree of accuracy of the air sampler used in an atmosphere of varying wind direction and magnitude.

During the handling process when coal is dropped as a stream on dumping sites, some dust emission occurs. It was shown that coal concentrations, due to this type of dust source, were low since the stream area was small while the dispersion from it was fast. This area source had a strength of $3.7 \times 10^6 \frac{\mu g}{m^2\text{-sec}}$ based on a stream or source area of $18.0\ m^2$ and a turnover rate of 10,000 tons per hour (1).

The satisfaction of similitude parameters ought to be attempted as nearly as possible when small scale experiments are performed. When a model of a two-dimensional wing section is under experimental investigation for determination of lift and drag coefficients, for example, it is desirable to test under the same Reynolds number as the full scale. In environmental experiments, the number of such dimensionless parameters becomes large because of the number of significant variables. The following parameters were suggested to be of some importance when a small scale model of a coal utilizing power plant was under investigation by Iversen (2).

$\frac{D}{L}$	Ratio of particle diameter to length
$\frac{V_R(H)}{V_f}$	Ratio of reference speed to particle terminal speed
$\frac{V_R^2(H)}{gL}$	Froude number
e	Restitution coefficient
$\frac{l}{L}, \frac{h}{H}$	Topographic geometric similarity
$\frac{z_0}{L}$	Roughness similitude
$\frac{H}{L}$	Reference height ratio
$\frac{z_0}{L^*}$	Stability parameter
$\frac{V_F}{V_{*t}}$	Particle property similitude
$\frac{V_{*t}D}{\nu}$	Particle friction Reynolds number
$\frac{V_R(H)L}{\nu}$	Flow Reynolds number
$\frac{V_*}{V_{*t}}$	Friction speed ratio
$\frac{\rho_A}{\rho}$	Density ratio
$\frac{V_R(H)t}{L}$	Time scale

In addition, the moisture content of particles and the particle sizes distribution are also considered important when experimental predictions are to be made. It is, however, impossible to satisfy all these parameters when model tests or small scale experiments are performed.

Since the properties of lycopodium spores are closer to coal dust (see Table 2, Chapter II), than many other available powders, this material was used to represent coal dust in a small scale model test of a Danish power plant (2). The lateral distribution of concentration downwind of the model power plant was determined for different wind structures (land wind-more turbulent, and sea wind-less turbulent) at different speeds and during short test runs (60.0 or 300.0 seconds). Lycopodium spores were trapped on oiled glass slides downwind of the plant site. By counting the number of particles along various lateral and two longitudinal positions, the lateral and the maximum longitudinal concentration diagrams were obtained (2). These diagrams reflect a very clear effect of buildings and obstructions in the model plant site. Further, the turbulent structure of the wind and the ratio of the wind speed to threshold speed was shown to be of great importance in relation to its effect on the mass flux of the particles. For a line source, a land wind threshold reference wind spread of 6.27 m/sec was

obtained as opposed to 3.97 m/sec for the sea wind. The mass flux due to the land wind was considerably more than that of the sea wind.

The results of reference 2 on pile configuration design are: First, for a line source, the maximum wind erosion from the top of the pile will occur when the wind direction is perpendicular to the long axis of the line source. Second, when several line sources are parallel to each other, but are all perpendicular to wind direction, the upwind source pile will experience more wind erosion. Third, vortices shed by upwind obstructions increase the wind erosion downwind, while due to high winds in these vortices the particles migrate farther down wind, compared to the cases with no obstructions.

Smit (24) presented coal dust concentration in the air downwind of a 200.0 x 200.00 m stockpile as shown in Figure 2.

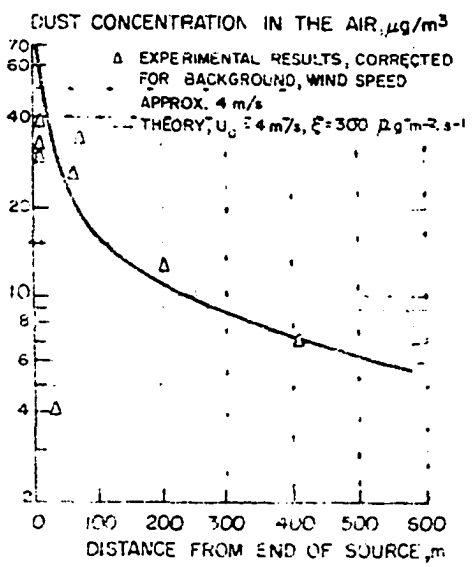

Figure 2. Dust concentration downwind of a large coal stockpile (Smit (24))

The theoretical approach for concentration prediction was based on a heavy gas theory described in reference (1). The source strength Q_{AS} at 4.0 m/sec was estimated at $1000.0 \frac{\mu g}{m^2\text{-sec}}$ when coal was recently dumped. The source strength of the same coal pile at 4.0 m/sec changed to $10.0 \frac{\mu g}{m^2\text{-sec}}$ six months later. This reduction of Q_{AS} was due to natural crusting of the coal surface.

The concentration diagrams of another stockpile some 150.0 x 120.0 m in area at wind speed of 6.0 m/sec was presented in Figure 2 of reference 24. Qualitatively speaking, the concentration diagrams from both piles were the same. On the other hand, since there were more fine particles in the first pile, the effective source strength was higher than that of the second pile.

The relative source strength under comparable conditions (same moisture content and same age) was shown to be linearly proportional to wind speed (24). However, there were only four data points relating Q_{AS} with V_R. It is difficult to draw a solid conclusion on the basis of only four data points.

It is indicated (18,28-30) that source strength Q is proportional to V_R to a power n. The value of n on the other hand has been determined to change, depending on unclear and unexplained reasons. Table 1 compares the experimental values of n due to area source diffusions.

Table 1. The empirical values of n for $Q \alpha V_R^n$

Reference	n	Type of dust
Blackwood and Wachter (28)	2.7-3.0	Coal
Janssen (29)	8.0	Ores
Gillette (30)	3.0	Loose soil
Bagnold (18)	3.0	Loose soil
Smit et al. (1)	8.0	Coal
Present work	6.30 point source 10.30 line source	Lycopodium spore

It will be shown in Chapter III that the variation of Q can indeed be made to vary with the cube of the wind speed. The coefficient in such an equation, however, instead of a simple constant, becomes a more complicated function of a wind speed ratio.

CHAPTER II. EQUIPMENT AND PROCEDURE

Experimental Set-up

Wind tunnel

The experiments were performed in the open circuit wind tunnel of the Aerospace Engineering Department at Iowa State University, Ames, Iowa. An environmental test section (A_{test} = 1.22 x 1.07 m, $L_{In-trap}$ = 6.5 m) equipped with a trap mechanism downwind of the test section was used (the trap collects particles which would otherwise be leaving the tunnel exit). The plates shown in Figure 3 are approximately at 45° relative to the wind direction. When a mass of particles reaches this trap mechanism, due to flow retardation, the consequent drag forces on the particles get smaller. The

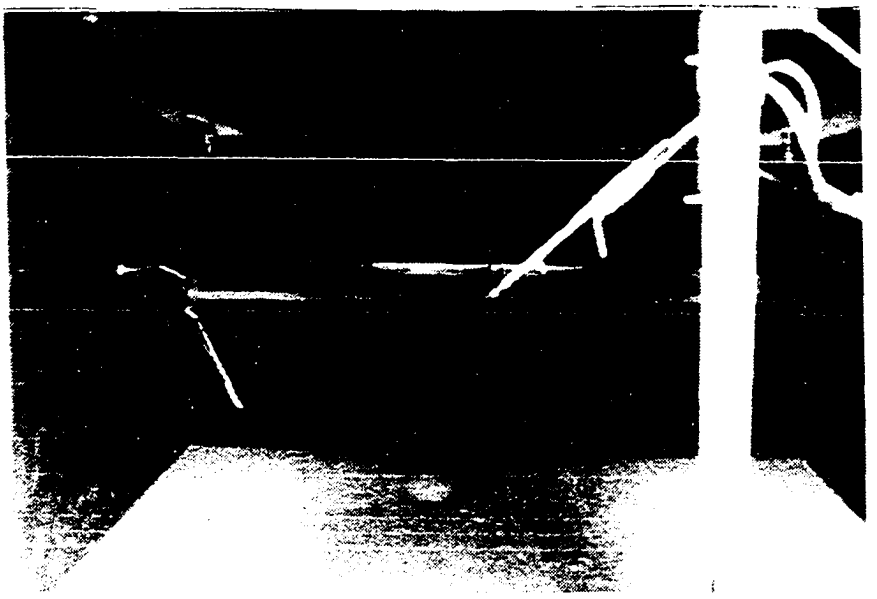

Figure 3. The trap mechanism downwind of the test section (downwind view)

wind can no longer carry all the particles, thus many get trapped into a chamber immediately downwind and underneath the plates.

This mechanism was used during the early part of the study when due to lack of information on source strength in many instances too much mass was diffused from the sources. Later, during the study, the emission was kept at lower rates, and it was soon realized that in many instances, the particles do not even reach the trap mechanism.

The wind tunnel was equipped with a remote control boundary layer surveillance mechanism shown in Figures 3 and 4. The measuring devices mounted on this system are used to make measurements of wind speed at any longitudinal, lateral and vertical location when proper adjustments of the system are made. The vertical travel is commanded by a remote control switch outside of the test section. The drive mechanism is a small electric motor which is connected to a threaded shaft. The rotation of this shaft about its longitudinal axis provides the vertical movement of the measuring systems. A potentiometer was also used to calibrate the vertical variations of height in units of length.

The lateral and the longitudinal adjustments were performed manually. This was accomplished by bolting the traverse mechanism to a horizontal support which itself was bolted to the rails on the walls of the test section (Figure 4). By

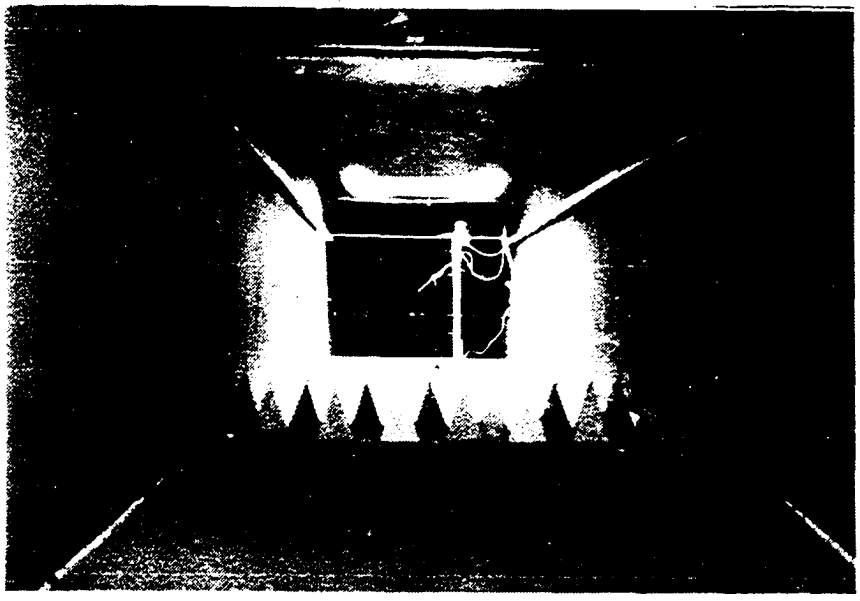

Figure 4. The inlet of the test section

loosening the bolts on the horizontal support and on the rails, the mechanism becomes free and can be positioned at any desired lateral and/or longitudinal location.

During this study, the heads of the measuring systems used were kept along the center line of the tunnel. The reference speed was measured 50.0 cm above the tunnel floor. The longitudinal position was kept at a distance 1.38 m from the leeward edge of the sources. However, the boundary layer profiles due to the two and the three-dimensional obstructions

were measured at a distance 35.0 cm from the leeward edge of the sources.

The tunnel was also equipped with vortex generating elements shown in Figure 4. The purpose of these were to increase the turbulence intensity of the wind. Measurements made with hot wire anemometer reflected larger peaks of instantaneous fluctuations when the elements were in. The generating elements were not removed during the course of this study.

Equipment

The instrumentation, the tools, and the equipment used during this study along with a brief explanation of their particular purposes are presented below.

1. An analytical balance with 310.0 gram capacity and 0.01 gram precision made by Ohaus was used to measure weight losses of the line source after the test runs.

2. A precision balance with chainomatic dial, capacity of 100.0 gram and precision up to 0.01 milligram made by Christian Beckers was used to measure weight losses of the point source.

3. Laboratory glass slides (75.0 x 25.0 x 1.0 mm) positioned in slot cuts in plates which had the same thickness at the slides, were greased to trap particles on ground levels. Several figures (7,8) show the slides and the plates.

4. A microscope made by Spencer was used for magnifying the particles trapped on the slides. The field of view of this microscope at its highest magnification was a circle of diameter 0.635 cm. The counting of the trapped particles in each field of view was either done under the microscope (less populated slides similar to Figure 5) or a picture of the view was taken by a Polaroid camera (more populated slides similar to Figure 6) for more careful analysis. Note that some of the slides were analyzed by an image dissector/image analyzer computer while most of them were analyzed manually.

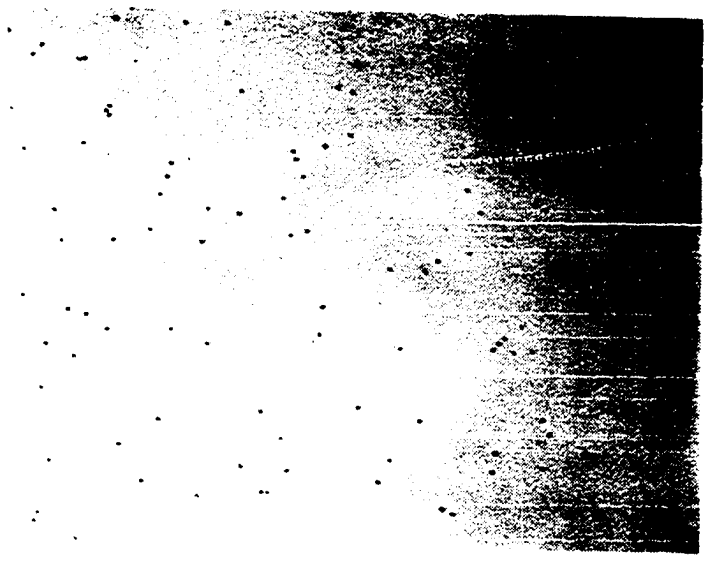

Figure 5. Lycopodium spores in a low concentration region (magnified 19.5 times)

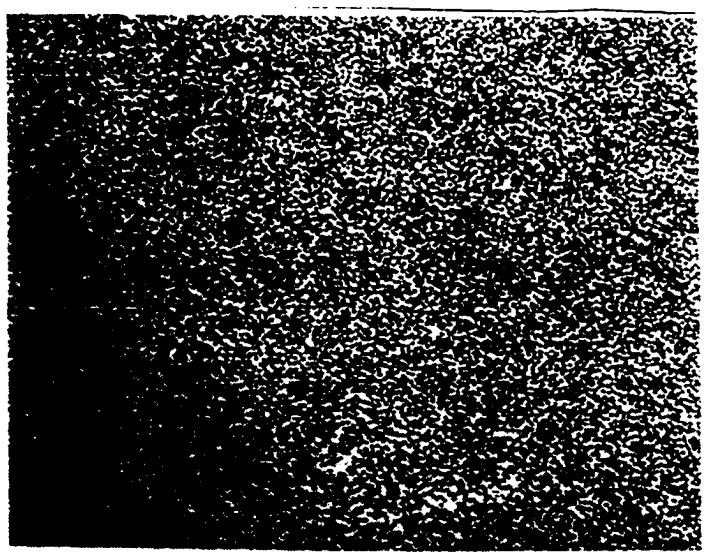

Figure 6. Lycopodium spores in a high concentration region (magnified 19.5 times)

5. A Polaroid Land Instrument camera, Model ED-10, was used to take pictures of the slides which were too populated for analysis under the microscope. Further, the calibration of the microscope and the camera revealed a magnification factor of 19.5.

6. A Canon camera was used to take the photographs.

7. Dow Corning high vacuum grease was used to cover the slides.

8. A water micromanometer was used to calibrate the more sensitive electronic measuring units (look at 9-12 below).

9. A Validyne (Model DP 45) pressure transducer was used to measure dynamic pressure. This unit was accompanied by a model CD 15 Carrier Demodulator. Due to malfunction of this unit, after a few months the speed measurements were made by a ruggedized hot wire and/or the water micromanometer.

10. The ruggedized hot wire (made by T.S.I.) and the water manometer were used to measure the same wind speeds (i.e., at the same time). The average of the two speeds was used as a representative of the reference wind speed.

11. In the absence of dust and when the tunnel was vacuumed and cleaned, the boundary layer measurements were made by the use of a Tungsten hot wire (3.80×10^{-4} cm diameter). The anemometer and the associated units used in conjunction with the hot wire were as follows:

Monitor and power supply Model 1051-2
Constant temperature anemometer Model 1050

The anemometry system used is made by Thermo-Systems, Inc.

12. Two true RMS digital voltmeters, Model 1076, were used to measure the output of the pressure transducer and/or that of the hot wire anemometer system.

13. An x-y plotter made by Hewlett-Packard (Model 7044A) was used to record the boundary layer profiles measured by the hot wire.

14. A Lemont Scientific image analyzer Model DB-10 and an image dissector camera, Model OLD1, were used to analyze

some of the photos. During the early part of the study, it was assumed that the use of this equipment would be more efficient as far as time and accuracy are concerned. It was experienced that the manual analysis of the photos were faster, more accurate and less expensive. The computer was not capable of counting the particles that were too close to each other. Figures 5 and 6 show many such instances. Under these conditions, the computer would count one big particle instead of several small particles. Also, there must be distinct differences between the apparent color of the particles compared to the background. For example, in Figure 5, the lower left corner is darker compared to the rest of the photo. This dark element could be counted as one large particle by the computer. To correct for such errors, the pictures had to be taken under precise exposure times and the grease had to be a thin layer, very evenly distributed on the surface of the slides. Since all this was manually controlled, each picture had its own background color. This in turn, means checking and adjusting of the computer for each new photo. The expenses of renting this computer was also a matter of concern. Therefore, almost all the photos were analyzed manually.

15. The transverse mechanism shown in Figures 3 and 4 was accompanied by a potentiometer. Ten volts DC excitation was fed across this unit from a panel containing several DC

power supplies. The potentiometer was used for calibration of height.

16. The ambient pressure and temperature were recorded from a mercury manometer board made by Central Scientific Company.

17. A MacGregor 400 stop watch was used to measure the duration of each test run.

The emitting source

In environmental studies of particle diffusion, two types of models have been used by many to represent the emitting sources of pollution. First, point sources have been used to represent single chimneys, dumping sites of coal dust or any small area containing such polluting substances. Second, line sources have represented a series of chimneys along one line or a pile of snow, coal, dust, etc. These sources are of course, limiting cases of area sources which usually cover a considerable area.

During this study, a point source (height = 1.20 cm, inner radius = 1.10 cm, wall thickness = 0.20 cm) was used to represent one source of pollution. A line source (height = 1.50 cm, inner width = 1.6 cm, wall thickness = 0.4 cm) was also used as a two-dimensional model of a pile. These sources were glued to thin sheets of aluminum at their bases. The aluminum sheets were then taped to the floor of the tunnel at the desired location. Note that the position of these

sources relative to the slides were never changed during the study. Several of the figures show the set-up when the sources are present.

The position of grids

After some preliminary investigation on the extent of particle dispersion downwind and in the lateral directions, twenty-five slides were used in a field covering 72.5 x 58.5 cm of area. The slides were put into slots provided in aluminum plates which had the same thickness as the slides. The reason for using these plates is to eliminate the effects of the shed vortices from the corners of the slides. This method was first used by Iversen (2) in 1981.

After the first few experiments, it was observed that a great amount of mass concentration takes place a few centimeters downwind of the point source. Further, it was realized that the lateral distribution of concentration due to point source approaches a constant value with downwind direction, and that at closer distances to the source, the variations of the lateral concentrations were more pronounced. It was felt that measurements of concentration at distances close to the sources would prove to be beneficial. This explains the single slide at the center line of the tunnel, next to the sources.

The material used

Particles of matter such as sand, dust, coal dust and other materials are not uniform in size and shape in nature. This creates enormous difficulties when mathematical or numerical modeling of diffusion are undertaken. To overcome these difficulties, uniform particles (same shape and size particles) which exhibit properties close to the most dominant particles in question are usually used for analysis. The most important parameters to be satisfied are the average particle diameter, particle density, terminal speed, threshold friction speed and the ratio of terminal to friction speed.

The material used in this study was the spore of lycopodium plant. There are no environmental nuisances associated with lycopodium spores. In fact, they are rare and very expensive. However, their characteristics are almost the same as those of coal particles with the exception that they are almost uniform in size and shape.

From the work done by Smit et al. (1) it was shown that between grain diameters ranging from 23.0 μm to more than 250.0 μm about 90% of migrating coal particles had 23.0 μm diameters. Table 2 compares the characteristics of coal and lycopodium spores.

Table 2. Characteristics of coal dust and lycopodium spores

	Average dia. $\bar{D}$ μm	Density ρ gr/cm^3	Terminal speed V_f cm/sec	Threshold friction speed V_{*t} cm/sec	Parameter V_f/V_{*t}
Coal	21.0-28.0	1.20-1.70	1.63-4.10	23.40-27.70	0.06-0.17
Lycopodium spores	39.0	1.20	5.64	20.0	0.28

The obstructions

A two-dimensional obstruction (height = 3.0 cm, thickness = 1.75 cm) and a three-dimensional obstruction (height = 3.0 cm, thickness = 1.75 cm, width = 2.60 cm) were tested as small scale models. They were taped to the floor of the wind tunnel at various locations. Their existence in the set-up resulted in interesting information on concentration distribution. Figures 7 and 8 are photographs showing the obstructions used.

Preliminary investigation

Without any quantitative knowledge of source strength variation with wind speed and time, it was found necessary to run some preliminary experiments at different ranges of wind speed and time, in order to get a rough estimate on

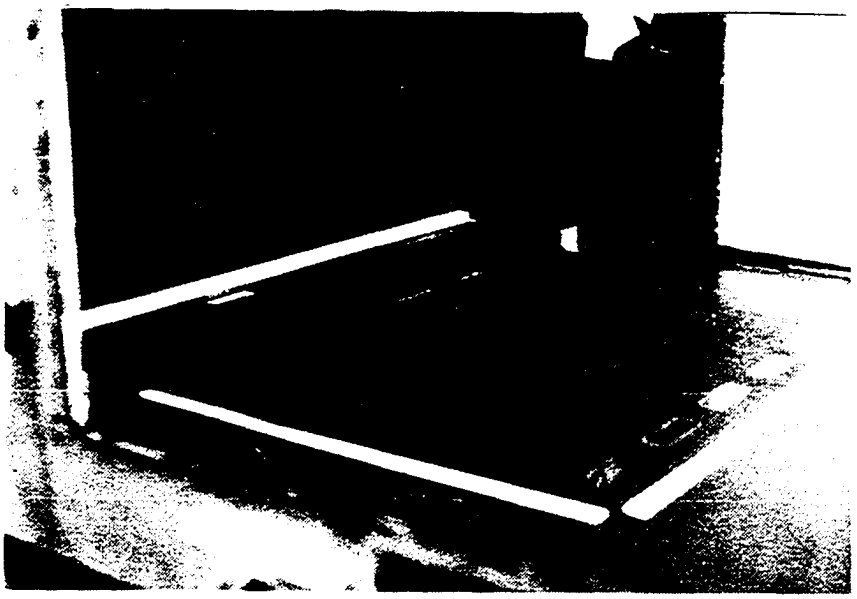

Figure 7. The two-dimensional obstruction in the set-up (between 2 rows of microscope slides, wind direction left to right)

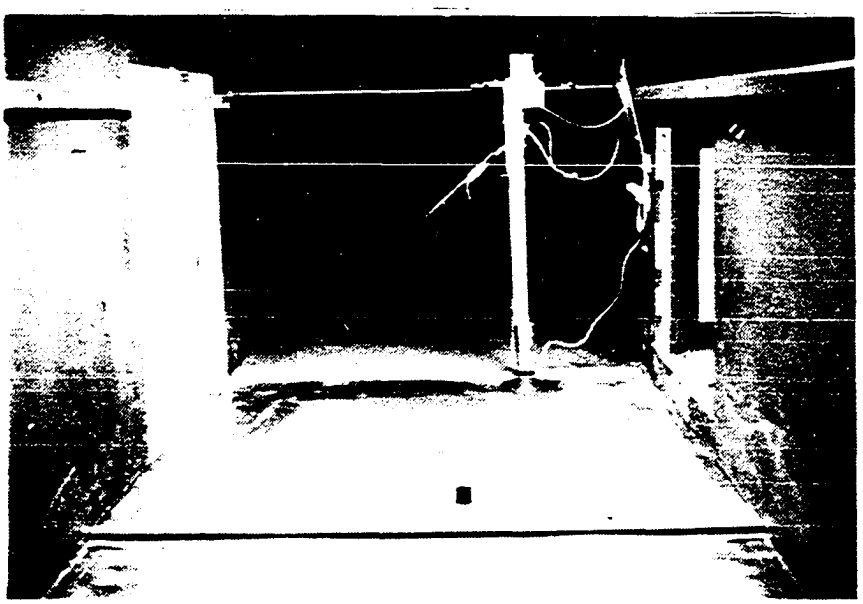

Figure 8. The three-dimensional obstruction in the set-up (small, dark object, view is downwind)

correlation between Q, V_R and ΔT.

The major experiments were run at proper wind speeds during sufficient time durations such that the slides did not get saturated with particles (Figure 5). When a slide is covered by too much material (Figure 6), the oncoming particles will skip over and either get trapped downwind, or simply leave the test section. Since one purpose of the study was to determine ground level concentration, it was therefore, necessary to trap all the particles which struck each slide.

Due to high cost of lycopodium spores, the preliminary tests were conducted by the use of crushed walnut shells. Figure 9 shows how the walnut shell particles vary in size and shape compared to Figures 5 and 6 for lycopodium spores.

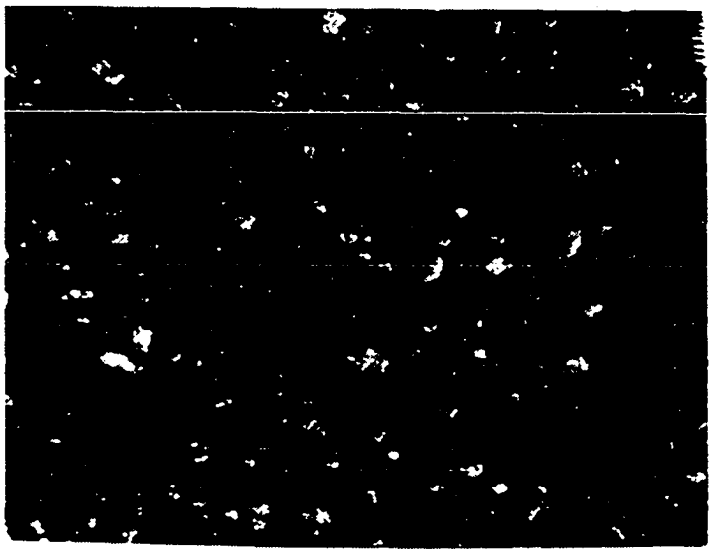

Figure 9. Walnut shell particles (magnified 19.5 times)

It was found that a range of reference wind speeds from 2.0 m/sec to 10.0 m/sec is close to the desired values. The time of each test, however, could vary from one hour to ten seconds corresponding to the low or the high limits of wind speed, respectively.

Major experiments

The step-by-step experimental procedure with and without the obstructions are presented below:

1. Before each test, the source was filled up with lycopodium spores to the level of the rim. The surface area of the particles was leveled with the edge of the source by use of the edge of a glass slide. The dusty areas on the outside walls were brushed off by use of a clean paint brush.

2. The source was weighed using the balances described earlier in this chapter.

3. The source was taped to the floor of the tunnel.

4. The slides were manually covered by thin layers of grease and were put into the slots in the aluminum plates.

5. The source was covered with a top door and the tunnel was turned on.

6. At this time, the desired reference wind speed was measured by use of the instruments described earlier.

7. The tunnel was turned off without changing the drive blade pitch, and the cover on the source was removed.

8. The tunnel was turned on again. At this time, a stop watch was also started to measure time.

9. The tunnel and the stop watch were turned off at the end of each run.

10. The source was removed and weighed once again. The difference between the original and the final mass is the total mass loss of the source. At several instances, because of procedural inaccuracies, the balance readings were higher after the experiments. Therefore, some error is expected to be introduced in such small weight difference measurements.

11. Each slide was observed under the microscope such that their surfaces remained untouched.

12. If there were too many particles on a slide, then Polaroid pictures were taken for a more careful analysis. Otherwise, the number of particles were counted under the microscope. If the concentration on each slide looked fairly uniform, the analysis was done at the center of the slide. If, however, there were lateral and/or longitudinal distinct variations of concentration then, more analyses were performed on each slide.

13. The tunnel was cleaned by the use of a vacuum cleaner and/or a large brush. Steps 1 through 12 were repeated for the next test runs.

Obstructions

When obstructions were tested, the above procedure was the same. The position of the obstructions were arbitrary. chosen. It was soon realized that the three-dimensional obstruction has less effect on the downwind concentrations compared to that due to the two-dimensional piece. The three-dimensional obstacle was therefore positioned closer to the downwind slides.

Boundary layer profile

The test section boundary layer profile was measured by a hot wire anemometer and was recorded on an x-y plotter. Due to the malfunction of the linearizer circuit, the output of the hot wire is a nonlinear voltage plotted against the dynamic pressure. This nonlinear calibration, along with the calibration of the height, was used to obtain the boundary layer profile of the test section (Figure B4).

The output of the hot wire was recorded for a time constant of 0.1 seconds. In order to obtain an average measure of the fluctuations, ten to twenty instantaneous wind profiles were recorded. This procedure was also used during the boundary layer survey of the wind due to the obstructions. All the boundary layer profiles measured during this study are presented in Appendix B.

The hot wire was positioned perpendicular to the flow

with the probe axis vertically oriented (z direction). Figure 10 shows the relative position of the hot wire with respect to the tunnel coordinates. As can be seen, the hot wire can detect any possible upwind flow which might be encountered in the high/low pressure regions.

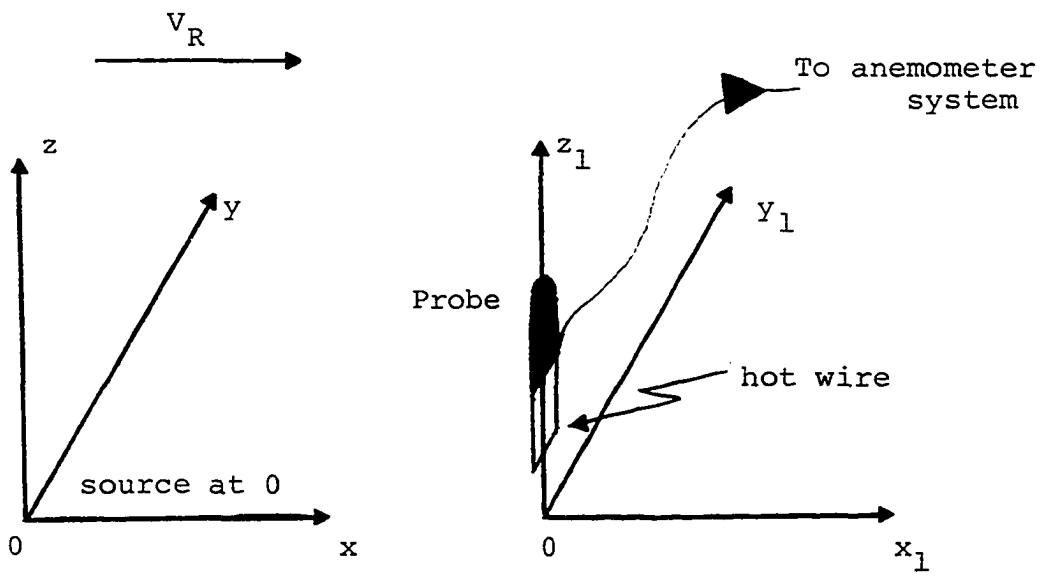

Figure 10. Orientation of the hot wire relative to the reference coordinate axes

CHAPTER III. RESULTS AND DISCUSSION

Through the calibration of the microscope it is possible to obtain the number of particles per square millimeter in the field of view. The number of particles per unit area are plotted against the lateral position at which the slides were analyzed. From the interpolation of these plots, the isolines of constant concentration (i.e., $\#/mm^2$) are drawn. The isolines are presented on a small scale view, showing the positions of the slides, the source and the obstruction relative to each other. The plots of $\#/mm^2$ versus lateral position y and the corresponding isolines are presented for each case in the same figures. These are Figures 11, 14, 18, 22, 24 and 27 in this chapter and Figures A1 through A25 in Appendix A.

Choice of Reference Coordinates

The reference coordinate system was chosen such that the origin is the position of the point source. The x axis is the center line of the tunnel floor and is in the direction of the wind. The y axis coincides with the leeward edge of the line source and the z axis is perpendicular to the xy plane at the origin and is pointed upwards (see Figures 10, 11b and 22b).

Point Source

No obstructions

Figures 11a, 11b, and 13 show concentration varying with x and y for V_R=6.84 m/sec and ΔT = 65.0 seconds. Figures A1 through A9 present the concentration diagrams for various wind speeds and time durations. The figures show that concentration is a maximum along the center line x. Further, it is noticed that the lateral variation of concentration (i.e., the slope of #/mm^2 vs. y curves) approaches zero with downwind distance (i.e., the curves become flat). Another interesting observation is that the lateral position of the zero isoline seems to be nearly independent of wind speed and time. The only parameter which significantly altered the lateral position of the zero concentration region was the three-dimensional effects due to the atmospheric turbulence external to the open circuit wind-tunnel. To overcome this problem, the tests were performed during nights and/or very calm days. Figures A2 and A9 show the results when the atmosphere was too windy and gusty.

The longitudinal position of zero concentration on the other hand seems to be more dependent on V_R and ΔT at distances far downwind of the source qualitatively speaking it seems that all the isolines with the exception of Figures A2 and A9 have about the same shape at the different values of

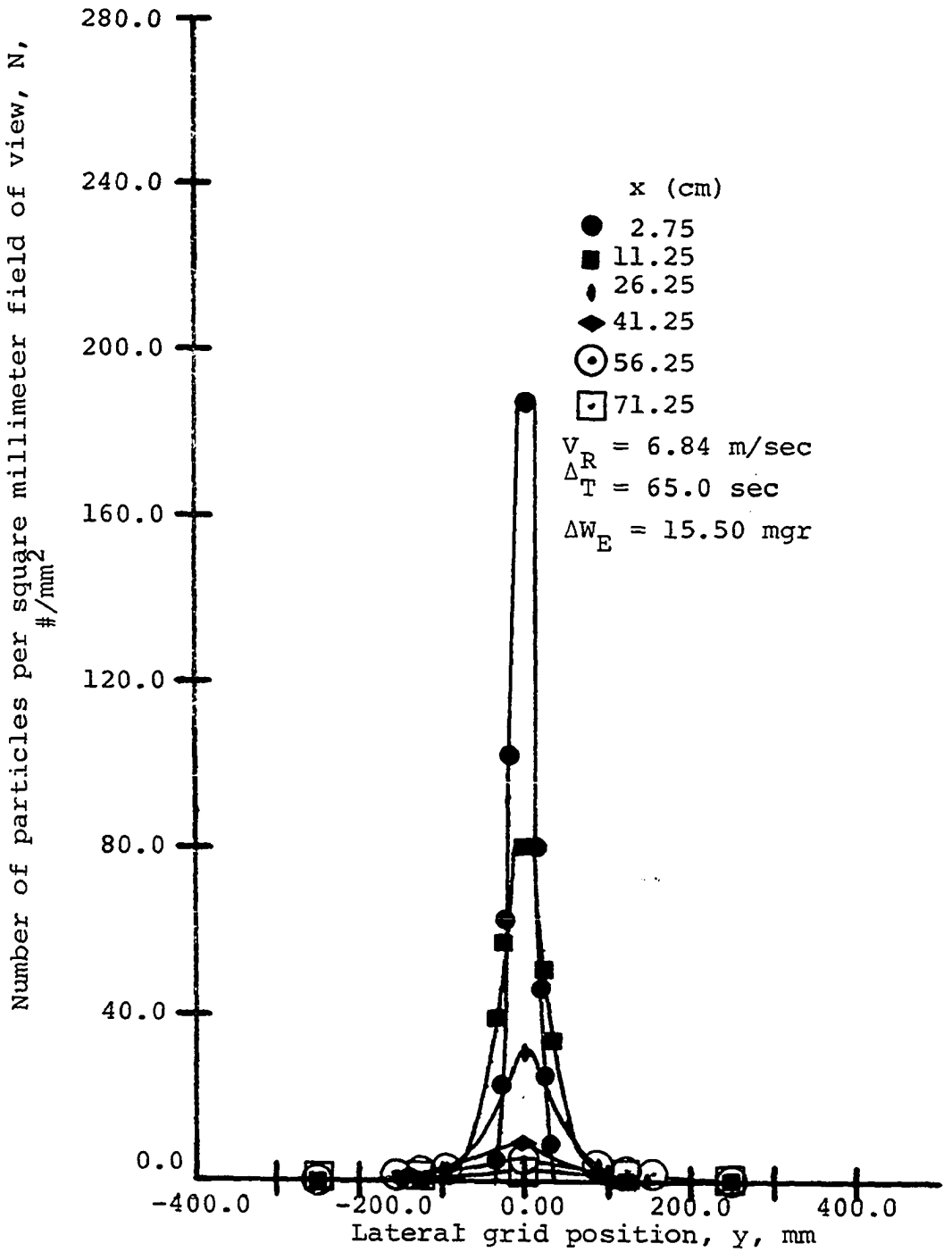

Figure 11a. N versus y for point source

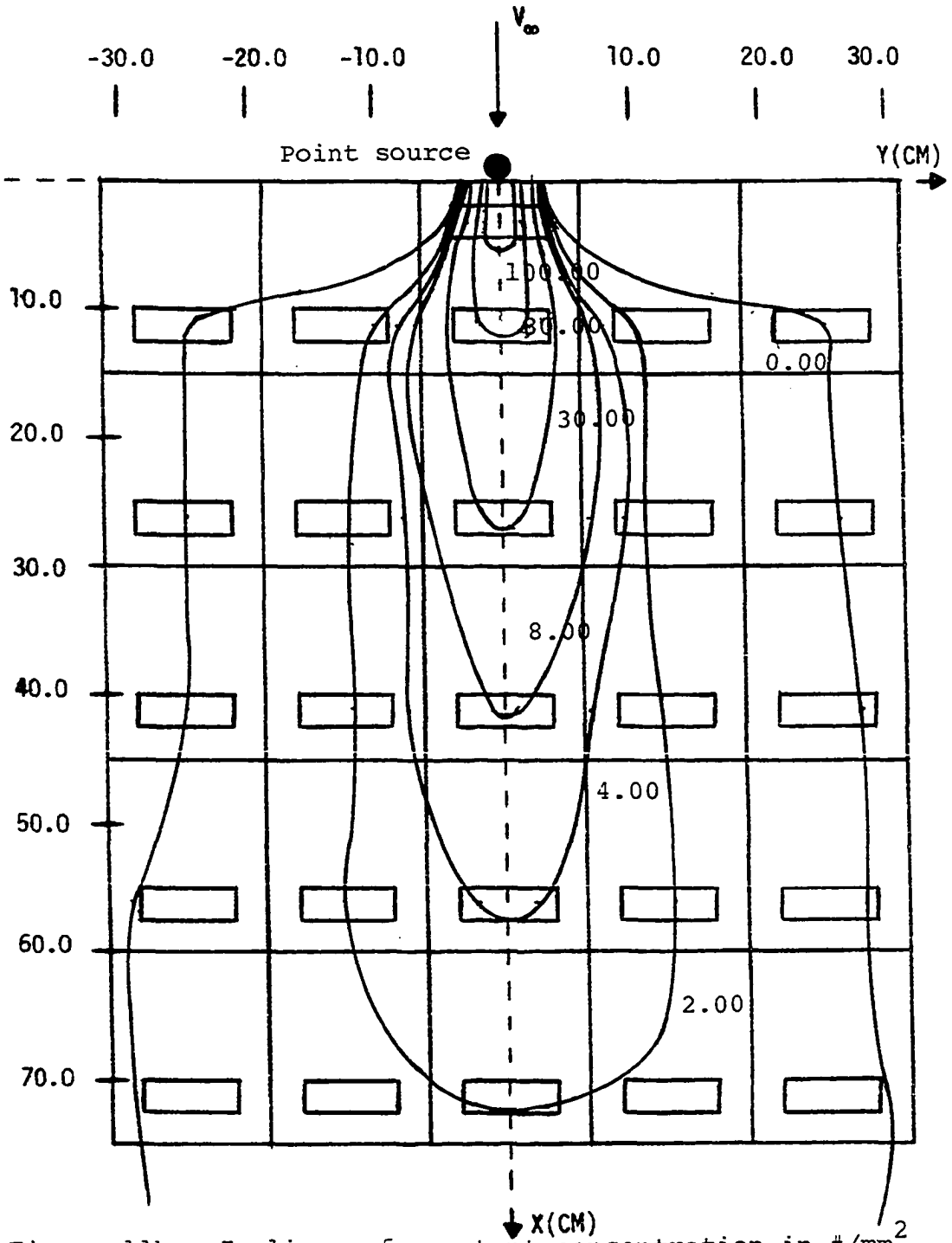

Figure 11b. Isolines of constant concentration in #/mm^2

concentration.

Total number of particles diffused

Since one object of this study was to determine the source strengths, therefore, it is necessary to know the amount of particle mass diffused from the source. One method used was by direct measurement of mass loss by use of the analytical balances described in Chapter II. Another method which reflects only those particles deposited on the surface within the measurement area is the use of a double integration procedure. This can be achieved by determining the area enclosed by the $\#/mm^2$ versus y curves. Mathematically, this can be represented as

$$N'(x) = \int N(x,y)\,dy = \text{number of particles per unit longitudinal distance} \qquad (2)$$

The values of $\int N dy$ are determined and are plotted against the x position as can be seen from Figure 12. To obtain the total number of particles diffused for each test run, one can measure the area enclosed by these curves. In order to achieve this goal it was necessary to interpolate the zero concentration positions by extending the curves until they intersected with the horizontal axis. The mathematical representation of the total number of particles is given as

$$\iint N dy dx = \int N'(x) dx = \text{total number of particles} \quad (3)$$

The curves in Figure 12 are almost similar in that they all drop to lower values of concentration along constant slopes until they reach an x value between 20.0 to 40.0 cm. At this position, the slopes are reduced and the concentration seems to behave approximately as an exponentially decreasing function of x. It should be mentioned that three of these curves behave somewhat differently from the rest. The first of these curves is at V_R = 7.6 m/sec and ΔT = 8.0 sec in Figure 12. The kink on the left of this curve could be due to the high wind speed which has saturated the slides close to the source. Second and third are the curves corresponding to V_R = 3.97 m/sec and V_R = 6.55 m/sec in Figure 12. These curves seem to have larger negative slopes on the left compared to the rest of the cases. Note that these curves bear the three-dimensional effects corresponding to Figures A2 and A9.

Point source strength

Considering the assumption that the point source has a very small area (i.e., area approaching zero) the source strength will be defined as

$$Q_{PS} = \frac{\iint N dy dx}{\Delta T} \times F \; \frac{\mu gr}{sec} \; . \quad (4)$$

The variation of Q_{PS} with wind speed is shown in Figure

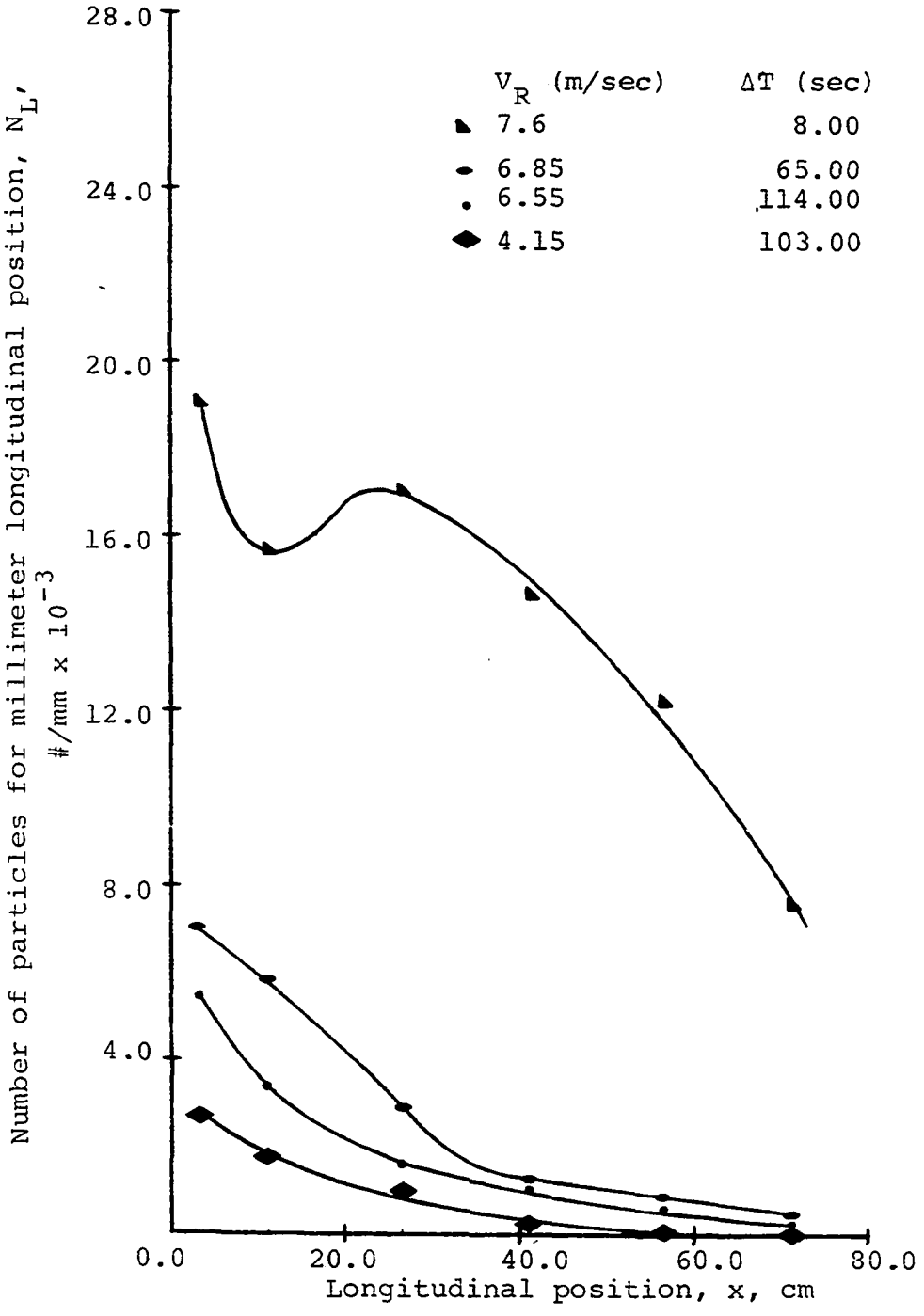

Figure 12. N_L versus x for point source

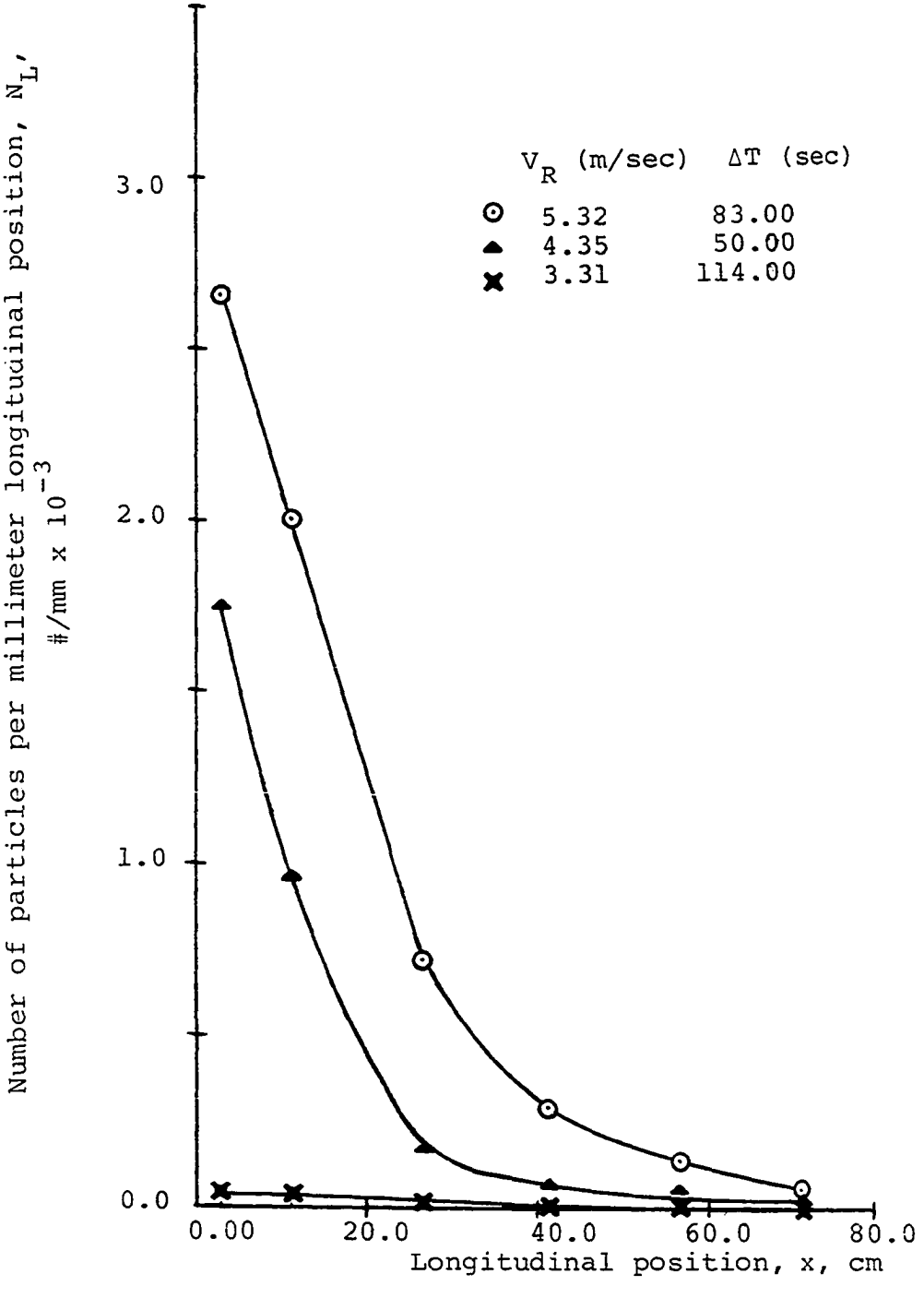

Figure 12 (Continued)

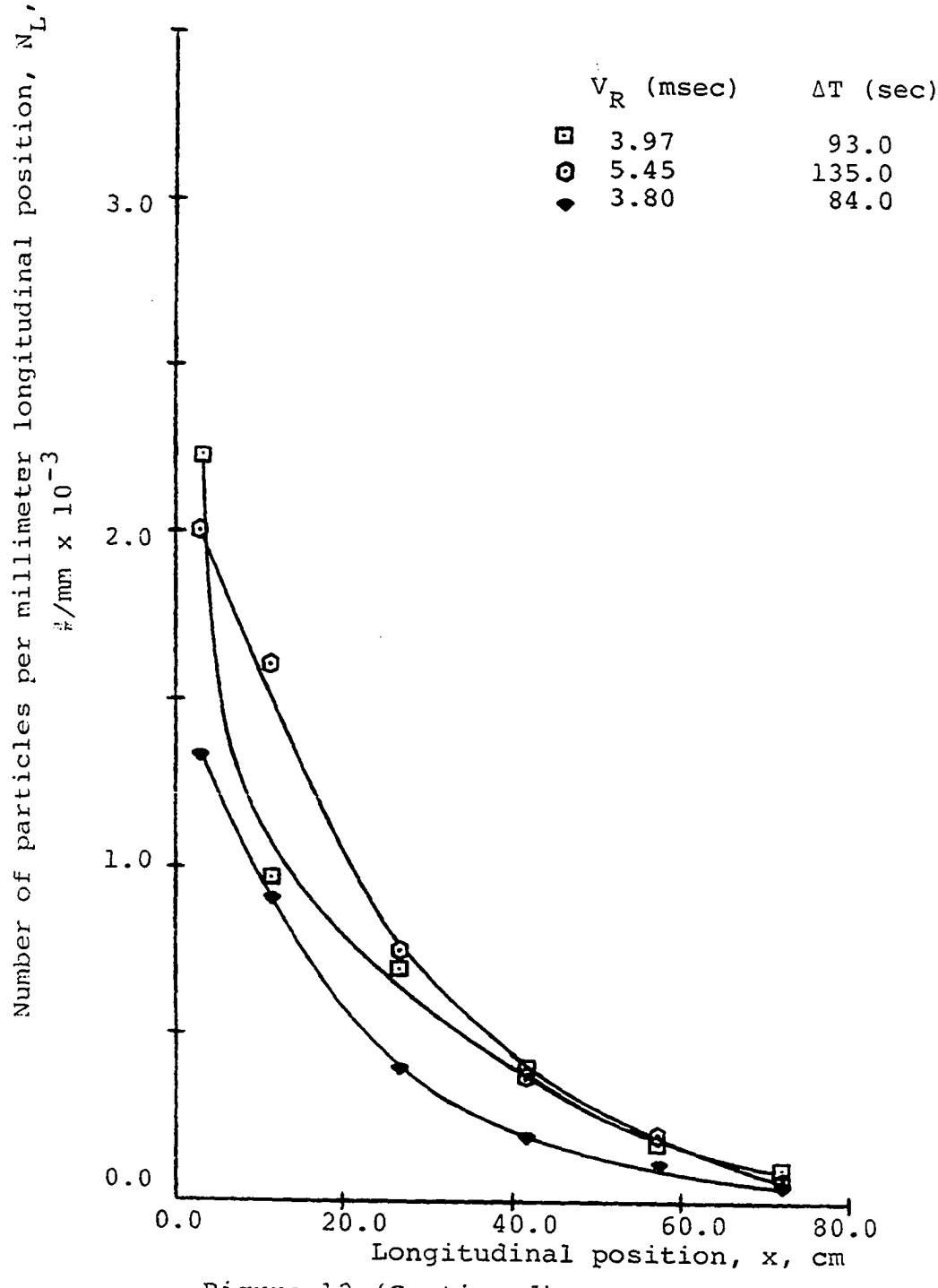

Figure 12 (Continued)

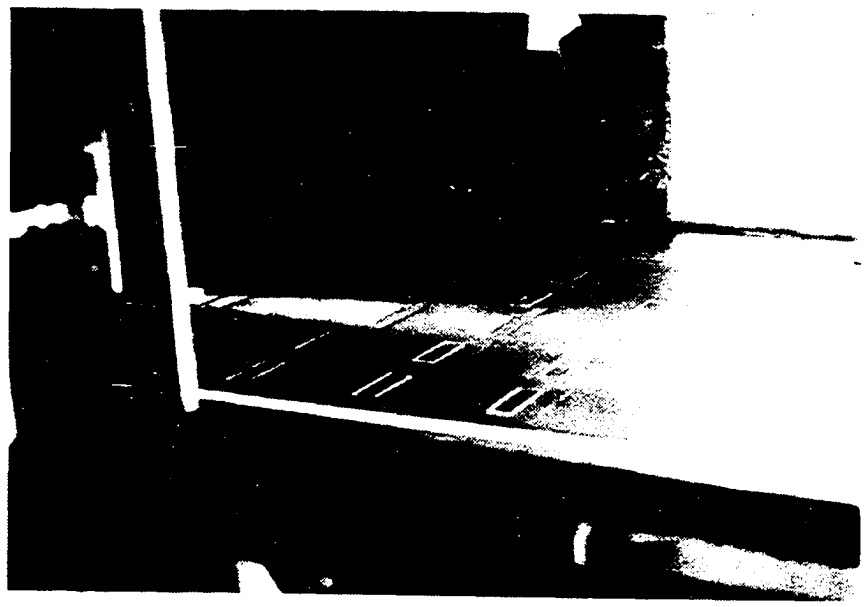

Figure 13. Concentration due to point source diffusion (V_R = 6.84 m/sec and ΔT = 65.0 sec)

31. A result of a least square fit of the data is the following equation.

$$Q_{PS} = 0.00574\ V_R^{6.79}\ \frac{\mu g}{sec}\ . \qquad (5)$$

It will be seen in Chapter IV that the relation between strength and wind speed is more complicated than is shown in Equation 5. Equation 5 is presented here only to provide a comparison with other published data which have used the same formula $Q = AV_R^n$ (see Chapter IV).

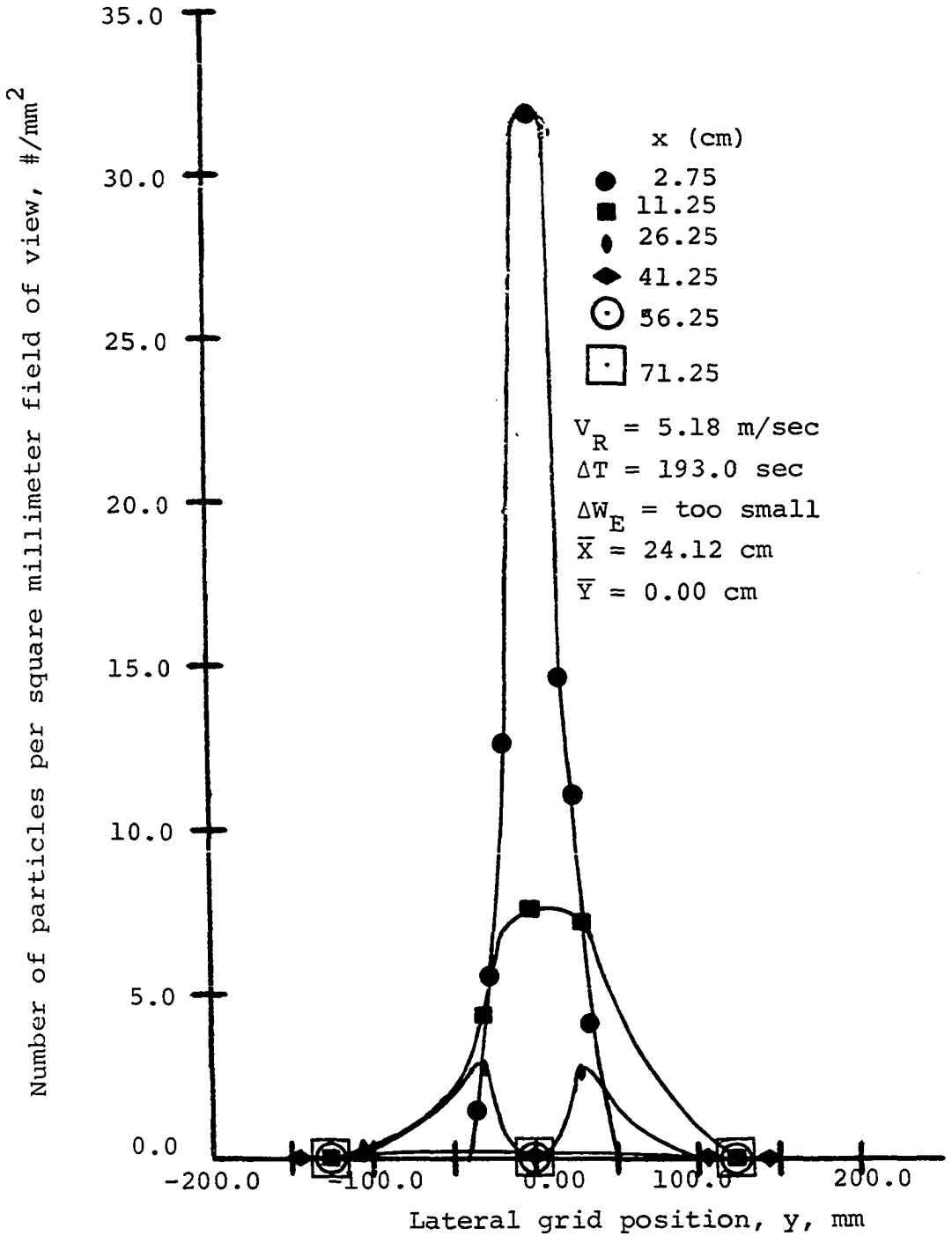

Figure 14a. N versus y for point source with three-dimensional obstruction

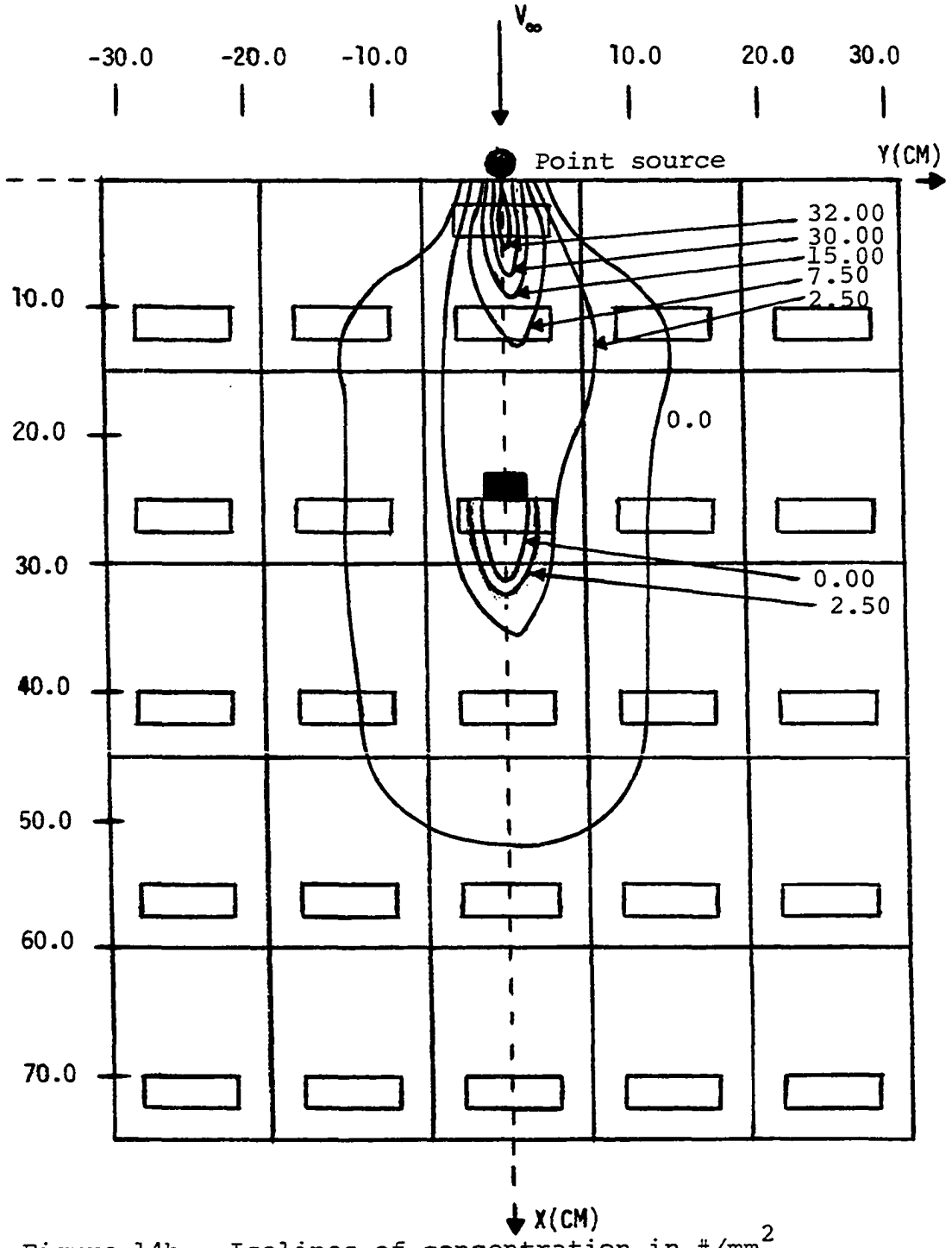

Figure 14b. Isolines of concentration in #/mm^2

With three-dimensional obstruction

The three-dimensional obstruction was at first randomly positioned in the xy plane. After a few experiments, it was observed that the effects of the obstruction on concentration distribution are limited to distances very close to the obstacle. Figures 14 and A10 show that the downwind effects of the obstacle are more pronounced compared to other directions. The location of the obstruction shown in Figures 16 and 17 is the same as that of Figure 14. Figures 16 and 17 show that there has been little deposition on the immediate upstream and lateral sides of the obstruction. A closer look at Figure 16 reveals that there are concentrations on the lateral sides of the slide at the downwind edge of the obstruction, but there are no particles along the center region. Probably, some particles have struck the dark area around the obstacle, but due to the high wind speeds around the obstacle, the particles did not settle in that area.

For higher wind speeds, Figure 17 shows that the slide right next to the obstruction is covered with particles in the middle while the lateral edges are bare. This can be explained by the larger drag forces on the particles due to faster winds. In this case, particles around the obstruction probably do not strike the ground at all. The lack of particles on the lateral edges of the slide next to the obstacle in Figure 17 is due to high wind speed and therefore

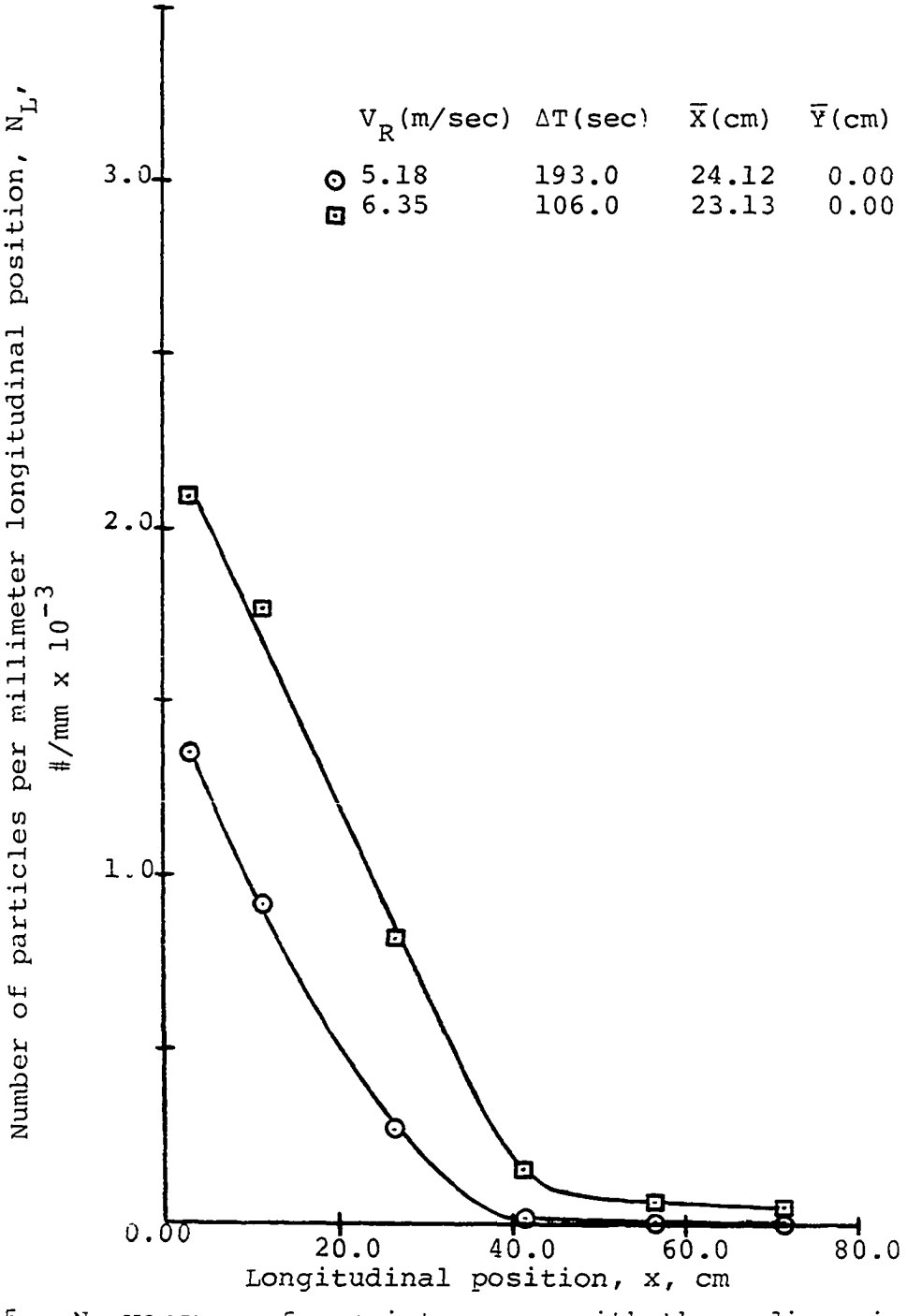

Figure 15. N_L versus x for point source with three-dimensional obstruction

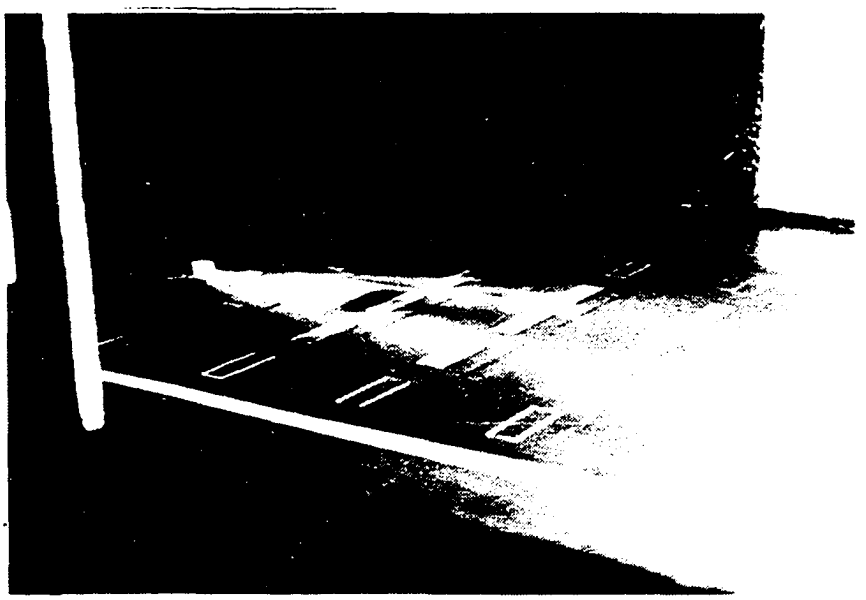

Figure 16. Point source with three-dimensional obstruction at $\overline{X}$ = 24.12 cm, $\overline{Y}$ = 0.00 cm, V_R = 4.21 m/sec, ΔT = 2940.0 sec. The obstacle is removed to obtain a better view

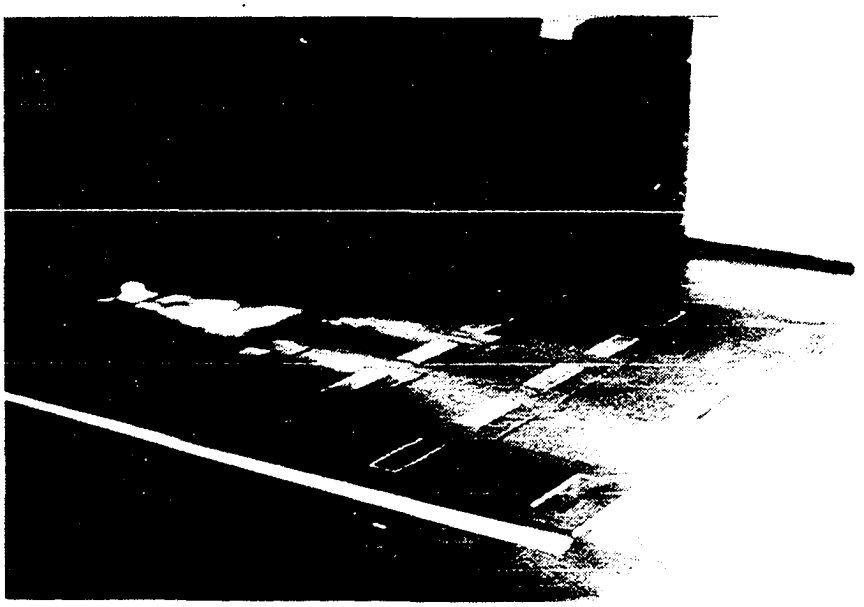

Figure 17. Point source with three-dimensional obstruction at $\overline{X}$ = 24.12 cm, $\overline{Y}$ = 0.00 cm, V_R = 6.65 m/sec, ΔT = 138.0 sec. The obstacle is removed to obtain a better view

high drag on the particles which do not reach the surface.

For larger wind speeds, the particles travel higher above the surface. As a result, some particles could travel over the top of this obstacle. When these particles reach the leeward side of the obstruction, they fall into a low velocity separated flow region. Consequently, the drag force is reduced and the particles descend and become trapped on the grease. On the other hand, some of these trapped particles could have also arrived from the sides of the obstruction (Figure 17).

Figures 14 and A10 show the concentration diagrams and the isolines of concentration due to two different wind speeds and time durations. There are two effects of the obstacle on the downwind concentration. First, there is a region of zero concentration immediately downwind of the obstacle. The extreme edges of this zero concentration region are shown in the isoline diagrams (Figures 14 and A10). Second, the concentration starts to increase with downwind and lateral distances and eventually reaches that of the primary flow, where the effects of the obstacle are no longer present.

The envelopes of the isolines shown in Figures 14b and A10b based on qualitative comparisons look similar. It seems that the zero isolines are laterally fixed, i.e., independent of wind speed. The change in the wind speed, however, seems

to alter the longitudinal position of the zero isolines. This was also observed for the point source.

Source strength with three-dimensional obstruction

It is thought that the three-dimensional obstacle could have an effect on source strength. However, from the boundary layer diagrams (Appendix B), it is seen that the effects of the obstacle on the upwind distribution is limited to the near vicinity of the obstacle. The strengths are determined using Equation 4 and are tabulated in Table 3. The strengths determined from weight loss measurements are also presented. Figure 15 is the result of the integration ($\int N dy$) on Figures 14 and A10. The areas enclosed by the curves of Figure 15 are the total number of particles diffused (i.e., $\iint N dy dx$).

Table 3. Point source strength when the three-dimensional obstacle is present

V_R m/sec	$\bar{X}$ (cm)	$\bar{Y}$ (cm)	Q_{PS} μg/sec	Q_{PSM} μg/sec
6.35	23.13	0.00	180.76	0.00
5.18	24.12	0.00	47.55	0.00

It is seen that the total number of particles per millimeter longitudinal length, drops somewhat linearly until distances between x = 35.0 cm to x = 45.0 cm are reached. After this, their slopes become larger in magnitude but remain negative.

Figure 15, in comparison with Figure 12, shows no qualitative difference in concentration per unit downwind length. The lateral variations of concentration on the other hand were the only noticeable differences compared to the point source results (Figures 11 and 14).

With two-dimensional obstruction

Figure 20 shows the experimental results after a test with the point source and the two-dimensional obstacle. The position of the obstruction is shown in Figure 18b. This position appears as a dark region along a lateral element on the floor of the test section in Figure 20. Upstream of this line there seems to be a large deposition of lycopodium spores. Downstream of the obstacle on the other hand, there are not too many particles present.

As can be seen from Figures 18 and A11, concentration drops drastically downwind of the obstacle. Further, the concentration isolines on the upstream part of the obstruction still looks similar to those of the point source with and without the three-dimensional obstacle. However, on the downstream section of the set-up, the total number of particles

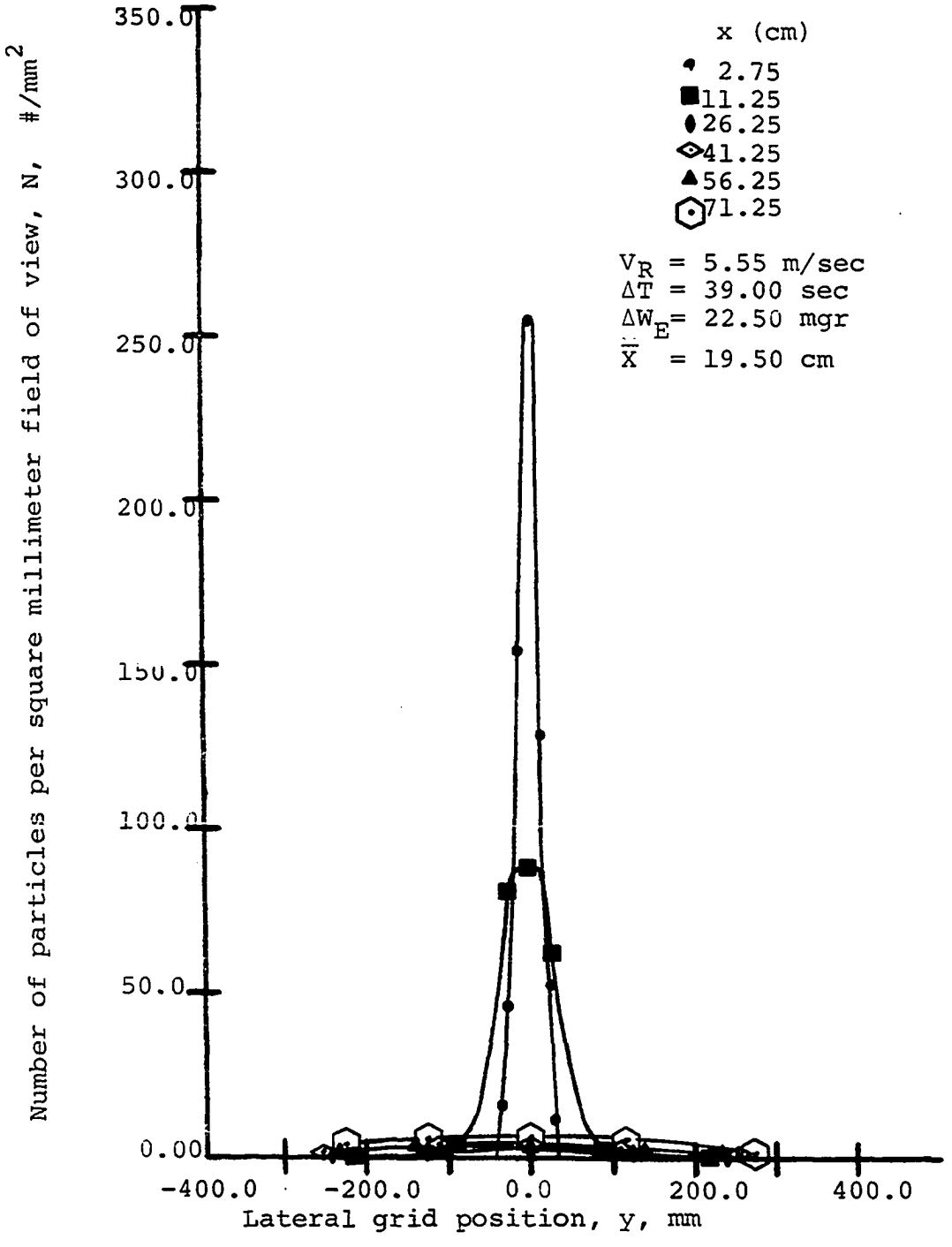

Figure 18a. N versus y for point source with two-dimensional obstructions

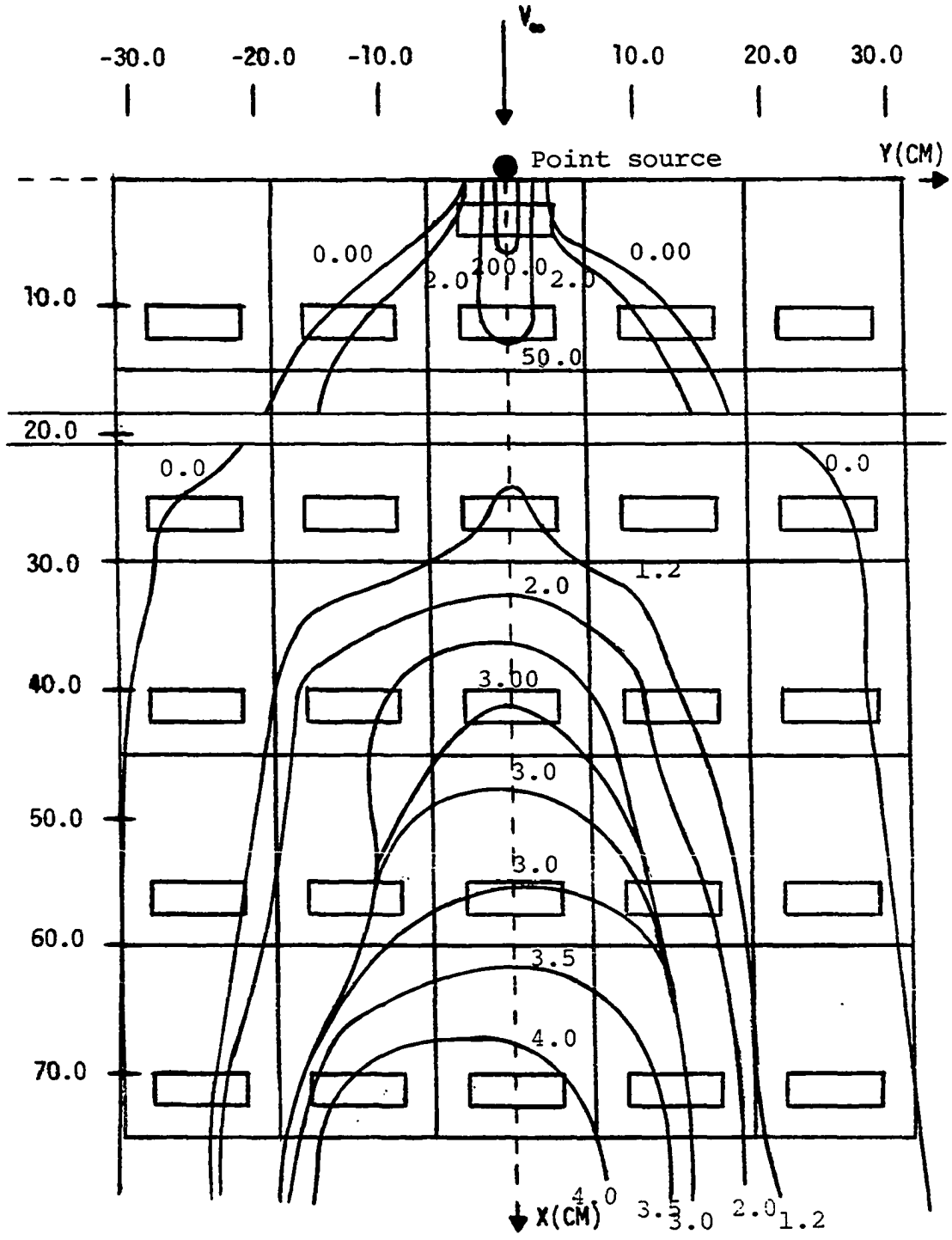

Figure 18b. Isolines of constant concentration in #/mm^2

has dropped to values two orders of magnitude less than the maximum values on the upstream part. At the same time, the downwind isolines now look quite different compared to previous cases (Figures 18b and A11b).

As is shown in Figure 18 the center line concentration downwind of the obstacles is very small. Farther downwind of the obstacle the centerline concentration increases by almost a factor of 2 at the farthest grid positions. It is difficult to predict exactly what happens after that last grid position is reached. However, since the wind tunnel surface at distances further downwind were checked after each test, and since it was found that there were not enough particles to collect by a brush, it can be assumed that this center line concentration decreases to zero a very short distance downwind of the measurement region.

In general, the isolines show that there are tendencies for relatively uniform concentration regions downstream of the obstruction.

Source strength with two-dimensional obstruction

The areas enclosed by the curves of Figures 18a and A11a were measured. These correspond to the number of particles per millimeter of downwind position. They were plotted against the x position of the slides as shown in Figure 19. It can be seen that due to the effects of the two-dimensional obstruction, some kind of a discontinuity has been created in

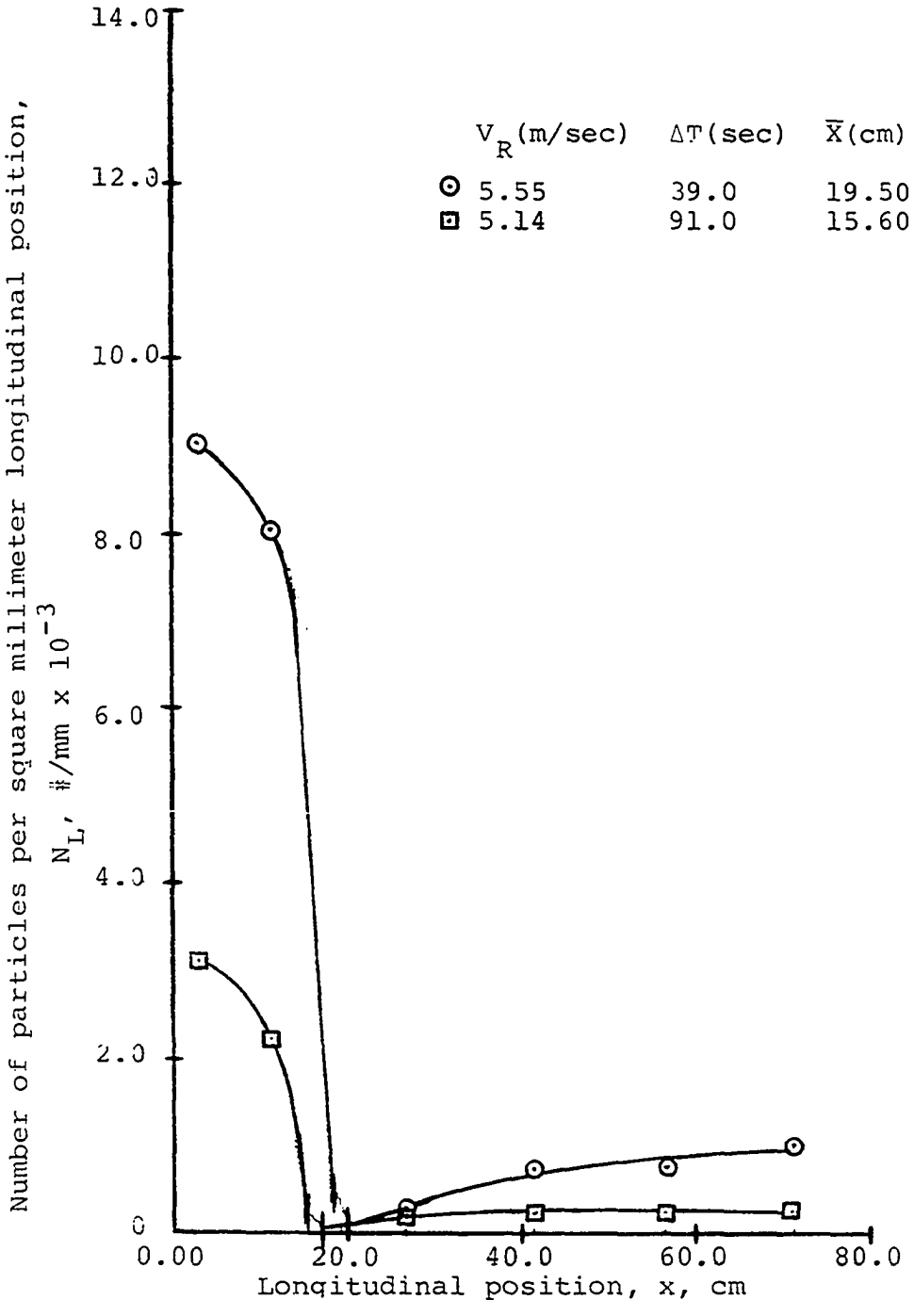

Figure 19. N_L versus x for point source with two-dimensional obstruction

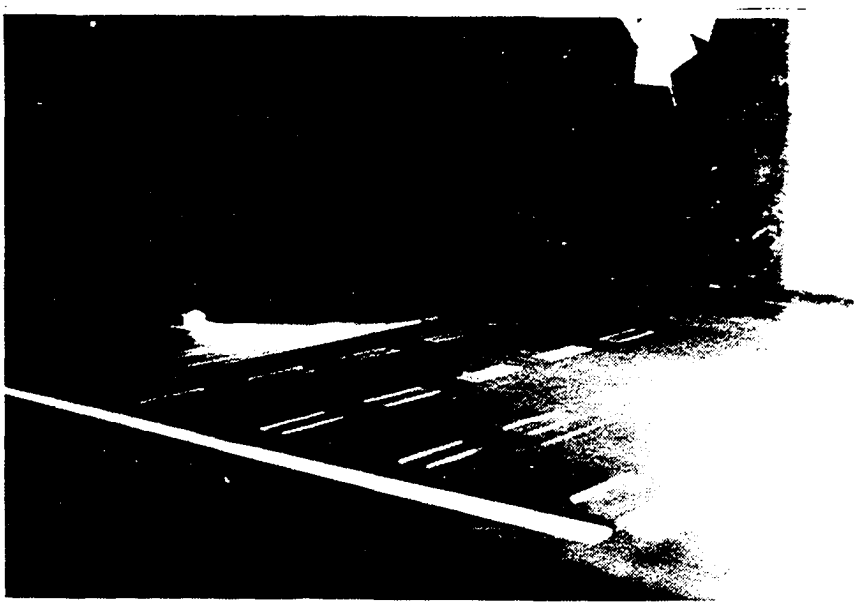

Figure 20. The concentration distribution due to point source diffusion with two-dimensional obstacle at $\overline{X}$ = 19.50 cm, V_R = 5.70 m/sec, ΔT = 750.0 sec

the longitudinal concentration. The effects of this obstacle at distances more than 32.0 cm upwind has been shown (Figure B2) to alter the boundary layer profile. Therefore, when the obstacle is too close to the source, the strength becomes affected.

The source strengths are determined both by using Equation 4 and by direct measurements of mass loss, and are tabulated below in Table 4.

Table 4. Point source strength with the two-dimensional obstruction present

V_R (m/sec)	$\bar{X}$ (cm)	$\bar{Y}$ (cm)	Q_{PS} (μg/sec)	Q_{PSM} (μg/sec)
5.14	15.60	0.00	222.13	0.0
5.55	19.50	0.00	1892.19	576.92

Line Source

No obstructions

The line source was tested for the same test conditions as the point source. Figure 21 shows the experimental set-up after a test with the line source. This figure does not show clearly the variation of concentration with length x, because of the fact that the entire surface is covered by the light-colored particles.

Particle concentration measurements, on the other hand, show that concentration is almost constant along lateral slides (Figures 22 and A12 through A15). The isolines such as those of Figure 22b were determined from interpolation of N versus y diagrams, similar to Figure 22a.

Three-dimensional effects due to large atmospheric gusts in the case of the line source can cause asymmetric concentration curves (Figure A12 in Appendix A for example).

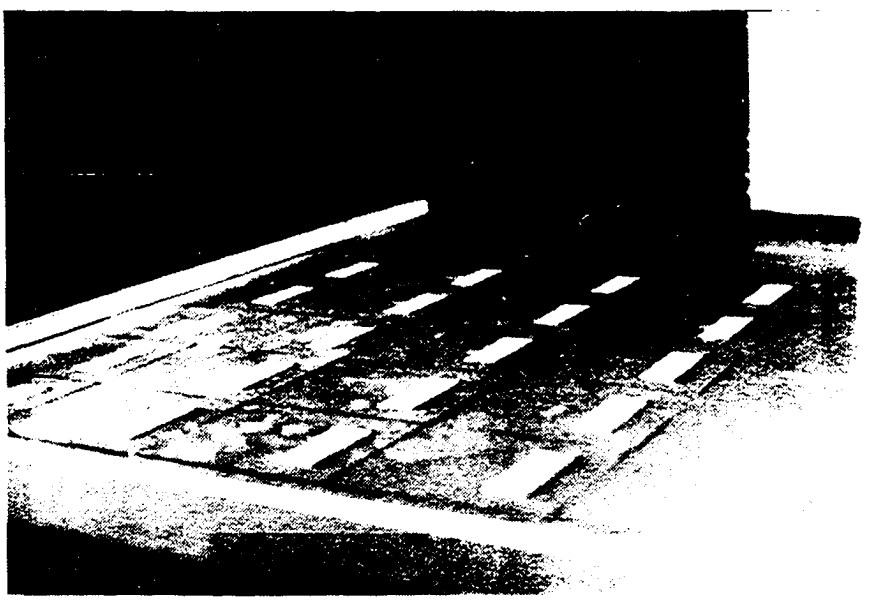

Figure 21. A view of concentration distribution due to line source diffusion at V_R = 5.55 m/sec, ΔT = 480.0 sec

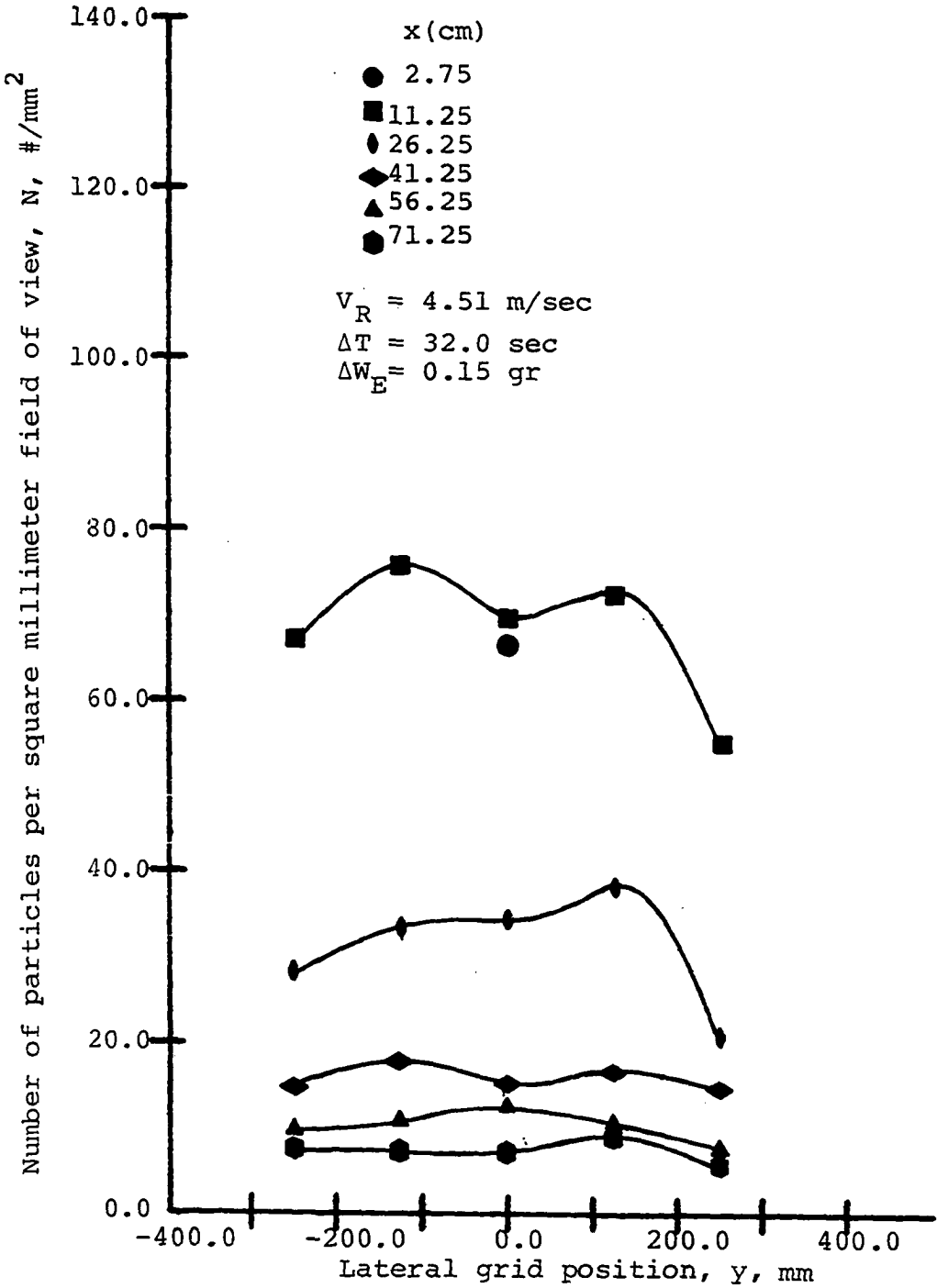

Figure 22a. N versus y for line source

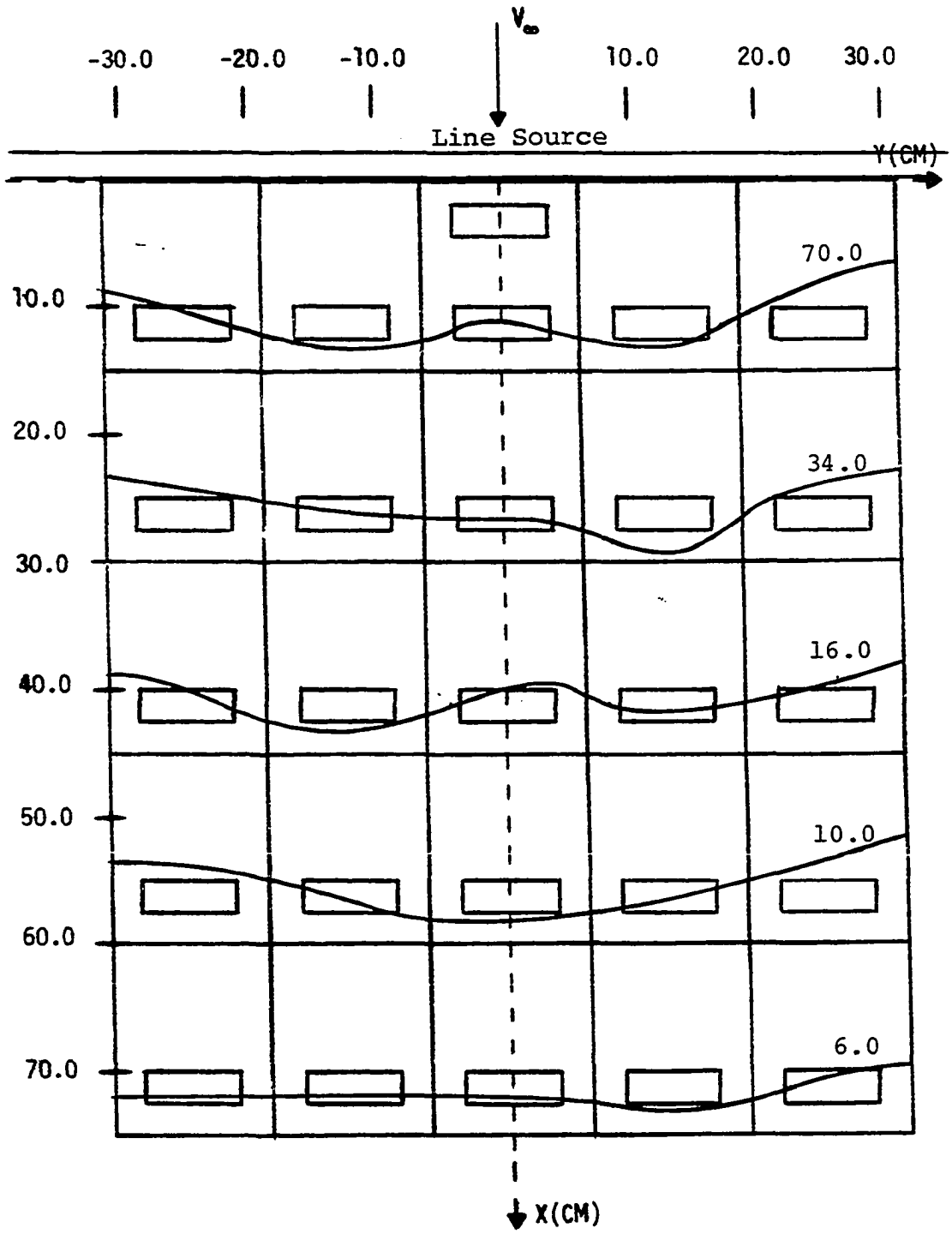

Figure 22b. Isolines of constant concentration in #/mm^2

To obtain an average concentration variation with downwind distance, the mean value of N for each lateral row of slides was determined. Figure 23 shows the variation with longitudinal distance x with the mean value of concentration. These curves are similar in shape in that the concentration grows rapidly with x near the source to a maximum. The downwind position of this maximum point is between 8.0 cm to 12.0 cm from the source. The location of the maximum concentration region seems to be independent of source strength.

At distances downwind of this maximum N, the concentration decreases to zero. Again, the shapes of the family of curves are consistent.

Line source strength

The source strength associated with the two-dimensional source is defined in units of $\frac{\mu g}{Dm\text{-}sec}$. Figure 22 represents the average number of particles per square millimeter field of view as a function of downwind distance x. One can determine the total number of particles per unit lateral distance y (Equation 6) by measuring the area enclosed by the curves of Figure 22.

$$\int N dx = \frac{\text{total number of particles}}{\text{unit length } y} . \qquad (6)$$

In order to complete such integrations, the curves in Figure 23 were extrapolated in the downwind direction to

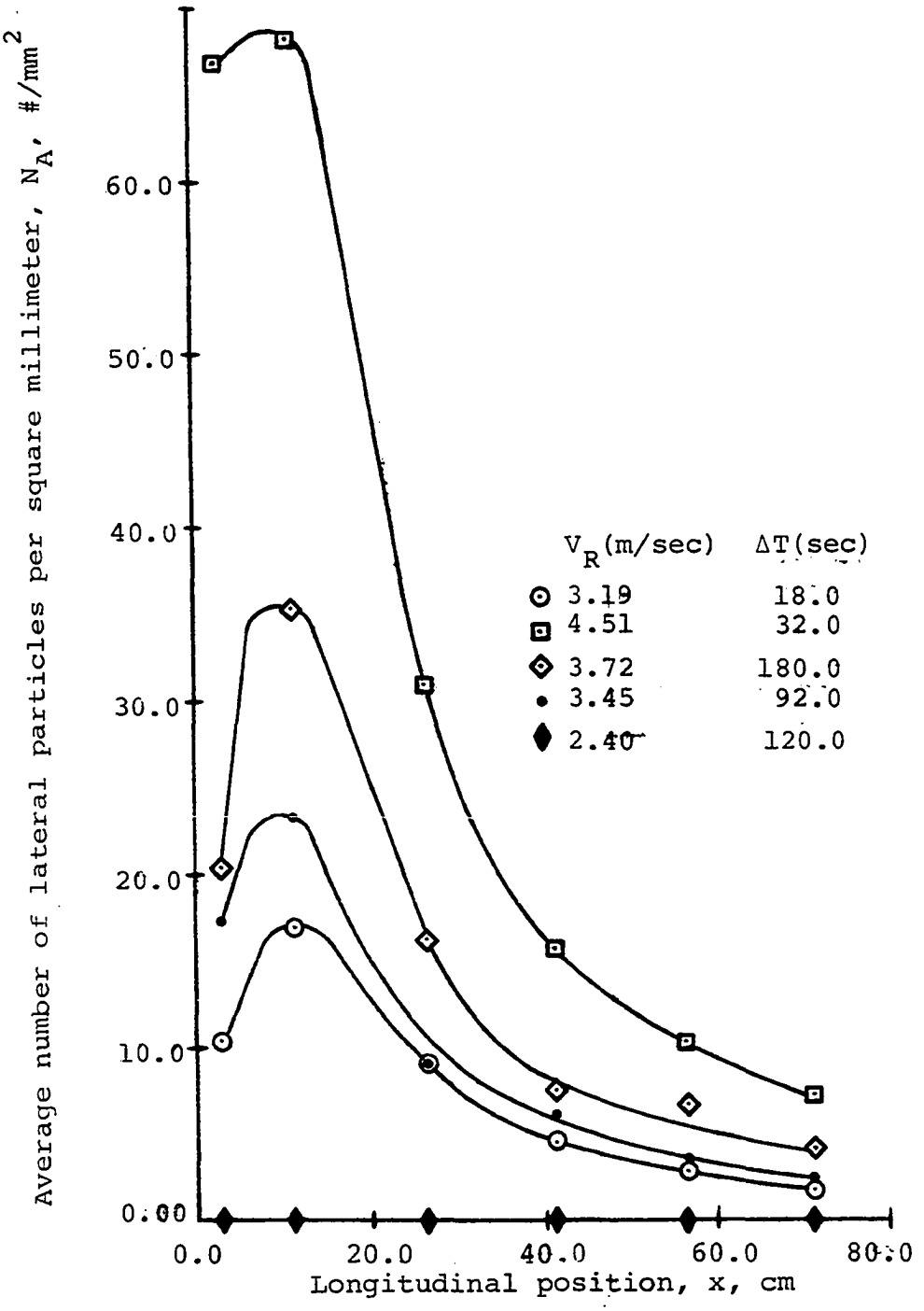

Figure 23. N_A versus x for line source

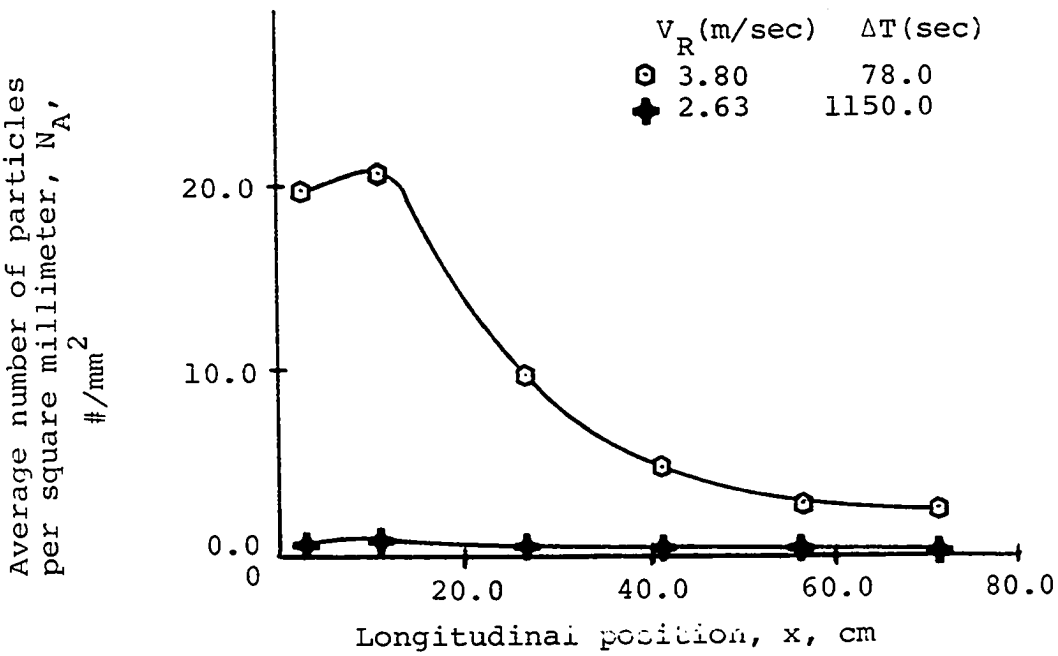

Figure 23 (Continued)

intersect with the horizontal axis.

The source strength defined with units of $\frac{\mu g}{Dm\text{-}sec}$ is found by multiplying Equation 6 by F and dividing it by ΔT. Therefore, Q_{LS} is

$$Q_{LS} = \frac{\int N dx}{\Delta T} \times F \frac{\mu g}{Dm\text{-}sec} \tag{7}$$

The source strengths are plotted as functions of friction speed in Figure 31. If the strength is determined as a function of reference wind speed in a form $Q = AV_R^n$, the following least square fit will result

$$Q_{LS} = 0.000221\ V_R^{10.931} \frac{\mu g}{Dm\text{-}sec} \tag{8}$$

This formula contains a numerical coefficient which is not dimensionless. It will be shown in Chapter IV that a dimensionless coefficient can be obtained by altering the formula to make it more appropriate to the physics involved.

With three-dimensional obstruction

The three-dimensional obstruction as can be seen from Figure 24 has an effect on concentration distribution limited to regions downwind of its location. The immediate areas upstream and on the lateral sides of this obstruction are not covered by particles. The reason is similar to the case when the point source was tested with this obstacle. That is, the local increase of wind speed in the vicinity of the obstacle is so large that it carries the particles away from

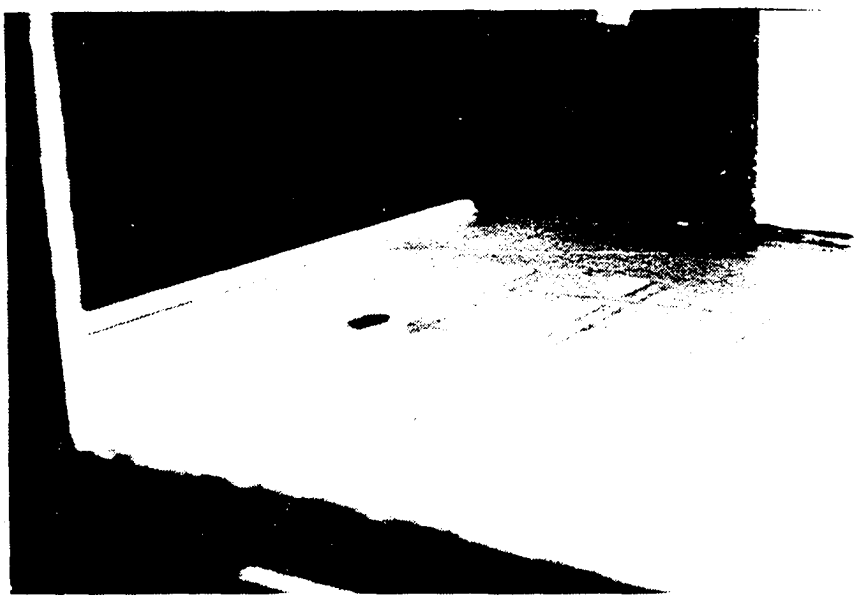

Figure 24. The effects of the three-dimensional obstacle on concentration distribution due to line source diffusion for V_R = 4.35 m/sec, ΔT = 310.0 sec, $\overline{X}$ = 23.87 cm, $\overline{Y}$ = 0.00 cm

and/or above these areas. The slide immediately downwind of the obstacle, however, is covered on its lateral sides by particles. This is because of the greasy surface on the slide, which traps the particles. The wind speed in those areas is not strong enough to move the trapped particles downwind. The three-dimensional effects of the obstacle can be observed at distances downwind and along the center-line of

the test section (Figure 24).

Figures 25 and A16 through A20 show the N versus x curves and the isolines of constant concentration for each test run. From these figures it becomes evident that the three-dimensional effects, as compared to the cases with the point source, are more pronounced at distances downwind.

From the isolines of concentration (Figure 25b), it can be seen that concentration is less in the region along the center line and next to the obstacle. At distances away from this region, the concentration increases until eventually it becomes equal to that due to the line source in the absence of the obstacle. Another interesting figure is A17 in Appendix A. In this case, the obstruction was positioned upwind of the line source. The effects are quite distinct to distances up to 30.0 cm from the source.

Source strength with three-dimensional obstruction

Since the effects of the three-dimensional obstruction were mostly limited to only one slide length and width and since there was no significant effect on the wind profile near the source (from hot wire wind profile measurements in Appendix B), the results were used to determine the source strength in the absence of the obstacle. When the lateral number of particles were averaged, along each lateral row, the slide closest to the obstacle was ignored (i.e., the

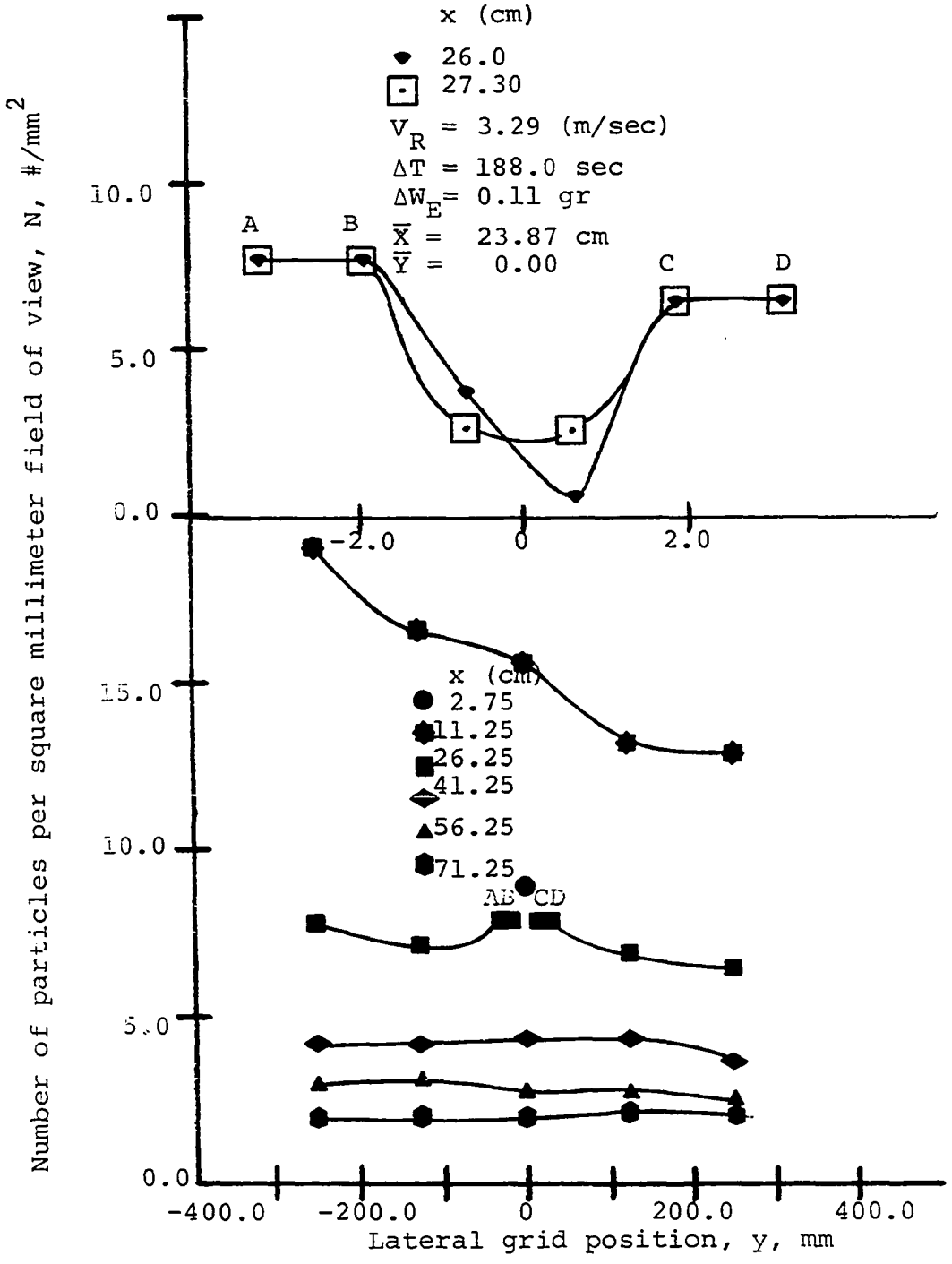

Figure 25a. N versus y for line source with three-dimensional obstruction

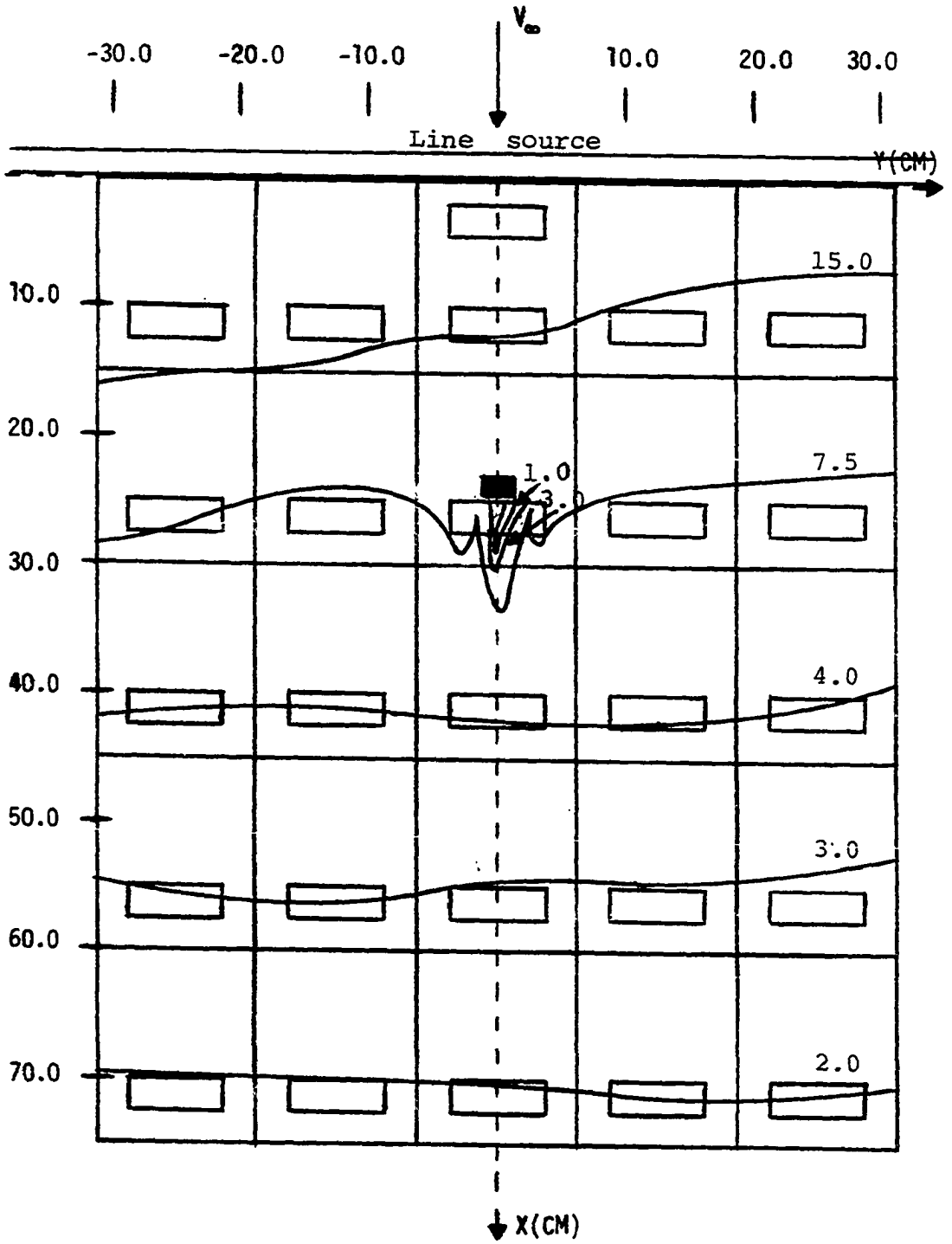

Figure 25b. Isolines of constant concentration in #/mm^2

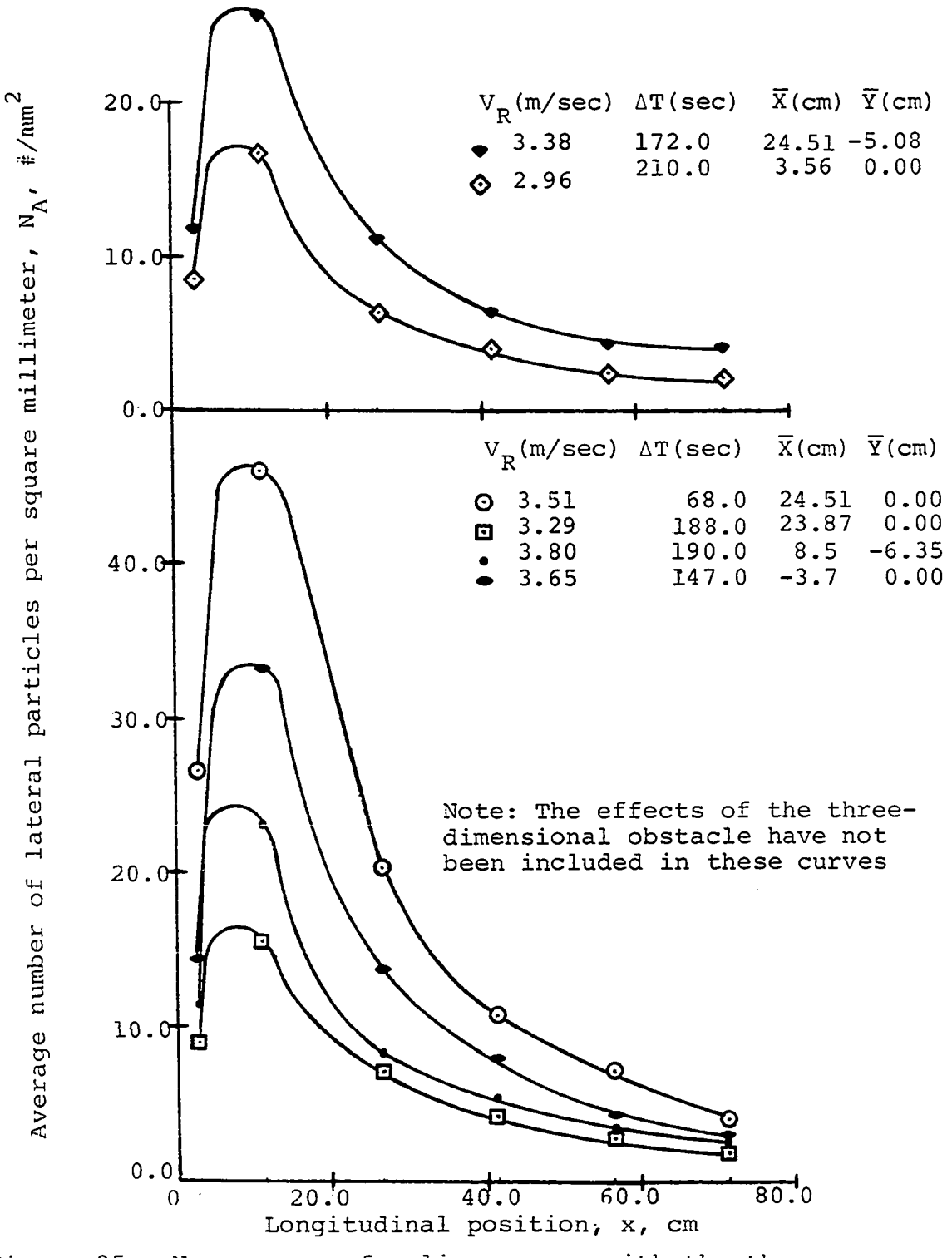

Figure 25. N_A versus x for line source with the three-dimensional obstruction neglected

slide which was most affected by the obstacle).

Figure 26 shows the average concentration as a function of downwind distance. By measuring the areas enclosed by these curves and by using Equation 7, the line source strengths are determined.

With two-dimensional obstruction

The wind structure at distances above 32.0 cm upwind and close to 38.0 cm downwind of the two-dimensional obstacle are affected by the obstacle's pressure field (see Appendix B). As a result of this, the concentration distribution due to a line source becomes altered by the existence of the obstacle. Figure 27 shows a massive concentration upwind of the obstruction. At downwind distances, the concentration has been reduced significantly. It was observed that no matter how close to the source the location of the obstacle might be, the concentration downwind of the obstacle is reduced drastically. One reason of course is that due to its height the obstruction blocks the downwind mass drift. However, due to the local increase of wind speed near the top of the obstacle, some particles skip over and are deposited downwind.

As shown in Figures 28 and A19 through A25, the particle concentration is always larger between the source and the obstacle. The downwind concentration drops to 1/20 to 1/40 of that of the maximum concentration. With increasing

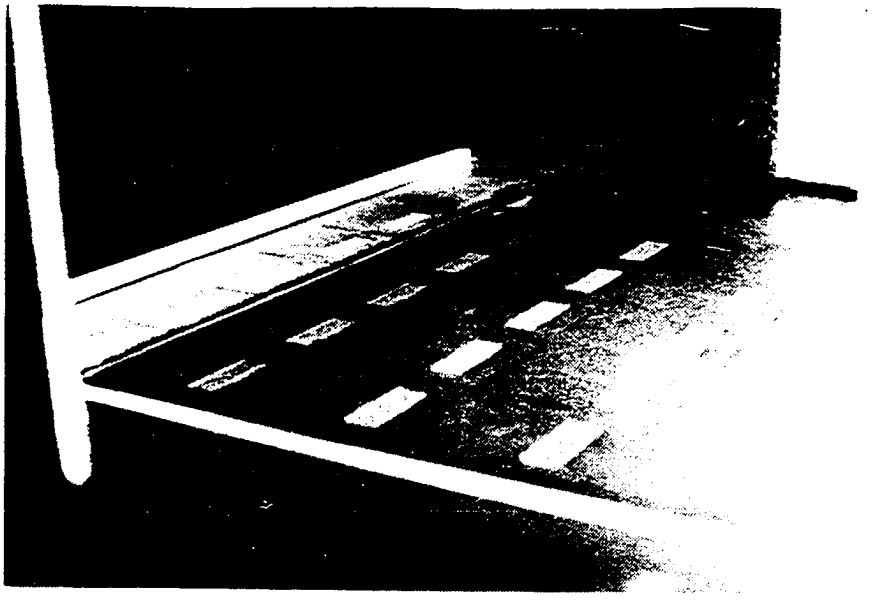

Figure 27. The two-dimensional obstruction alters the state of mass concentration (V_R = 4.75 m/sec, ΔT = 350.0 sec, $\overline{X}$ = 16.90 cm)

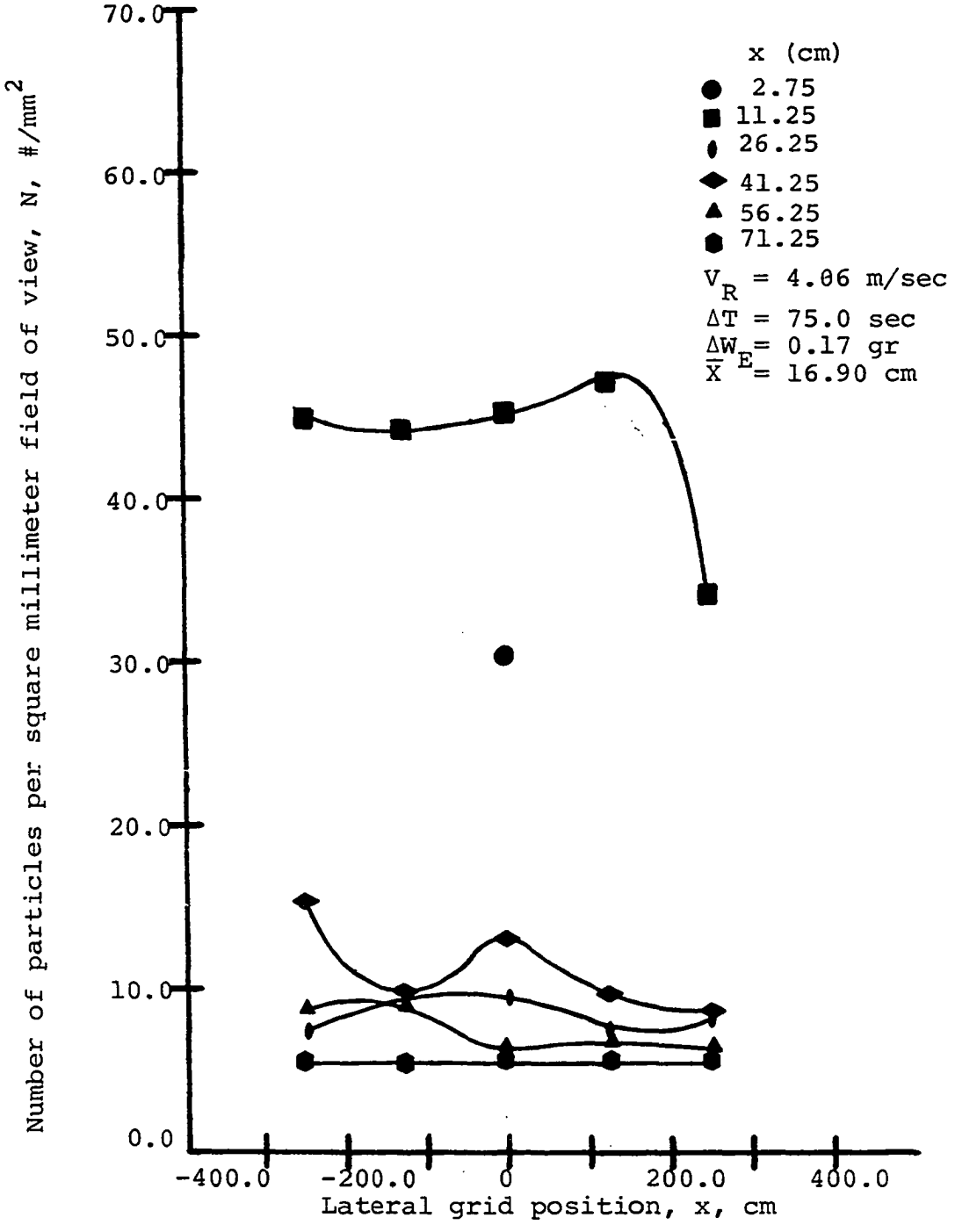

Figure 28a. N versus y for line source with three-dimensional obstruction

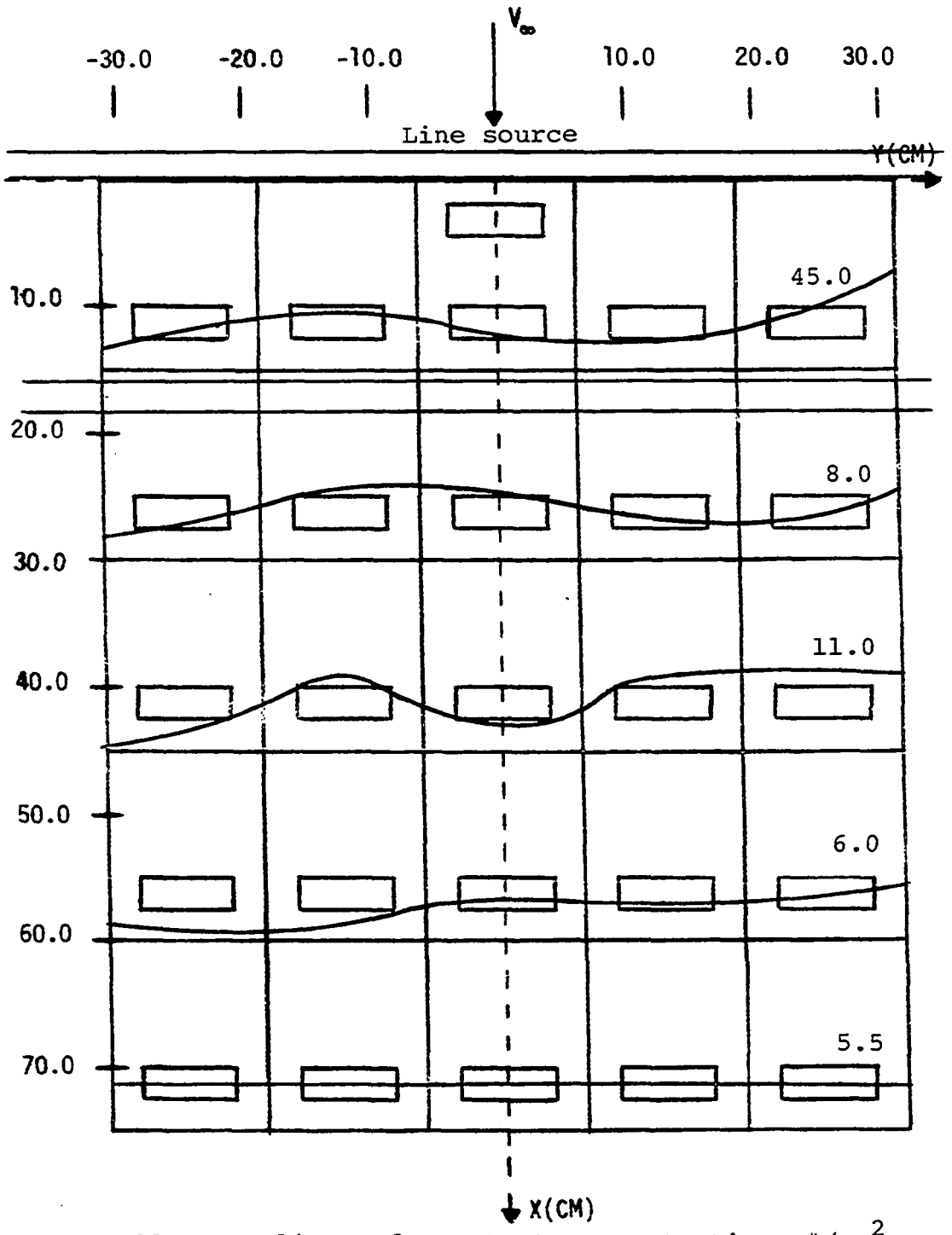

Figure 28b. Isolines of constant concentration, #/mm^2

downwind distance the concentration grows to a peak value. Further downwind the concentration decreases to zero.

As illustrated in Figure 28b all the isolines have opposite shapes compared to their corresponding N versus x curves, except the isolines at the closest downwind distances from the obstacle. This is due to the fact that in this region, the concentration is increasing with x. This could also be observed from Figure 29.

When the two-dimensional obstruction was positioned upstream of the source ($\overline{X}$ = -3.4 cm on Figure A25) the particle mass flow was reduced by a factor of 40 to 50 compared to the same speed with a downwind obstruction. Figure A25 shows a concentration variation of 0.16 to 1.57 particles per square millimeter. Another interesting observation is that the location of the maximum concentration N has now moved closer to the source than for the obstruction placed downwind.

When the obstacle was moved closer to the source at $\overline{X}$ = -2.75 cm not a single particle was diffused. Therefore, it seems that the obstacle has a wake of low or zero wind speed close to the surface and immediately leeward. This is substantiated by the results in Appendix B.

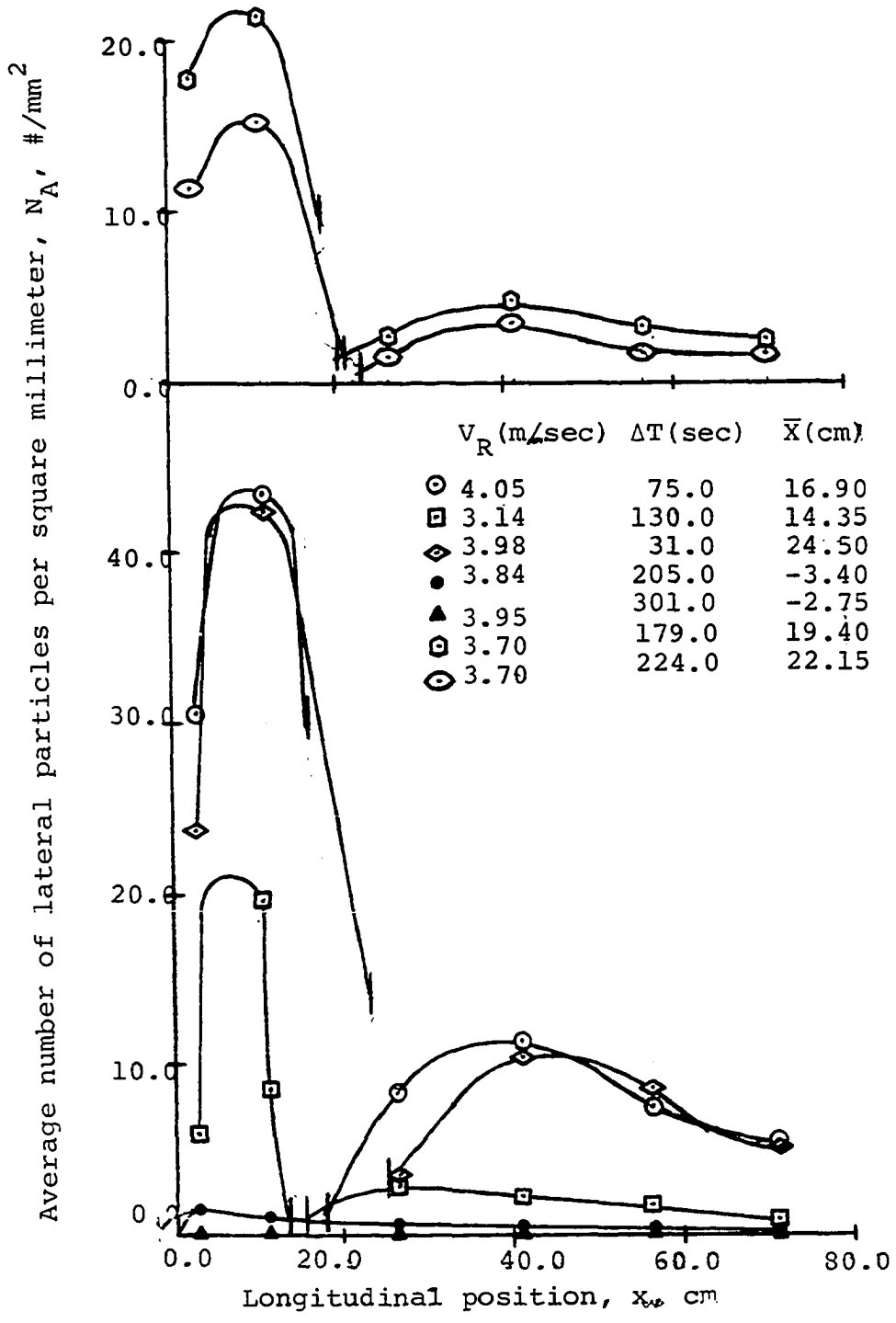

Figure 29. N_A versus x for line source with two-dimensional obstruction

Source strength with two-dimensional obstruction

The source strength was evaluated using Equation 7 and by the direct measurements of mass losses from the source. The results are tabulated in Table 5. Note that the source strengths presented here are dependent on the various wind profiles created by the two-dimensional obstruction at different $\bar{X}$ positions.

Table 5. Line source strength when two-dimensional obstruction is present

V_R m/sec	$\bar{X}$ (cm)	Q_{LS} $\frac{\mu g}{Dm\text{-}sec}$	Q_{LSM} $\frac{\mu g}{Dm\text{-}sec}$
3.69	19.40	125.98	36.84
3.70	22.15	70.48	18.40
3.95	-2.75	0.00	0.00
4.05	16.90	735.71	186.86
3.98	24.50	1544.30	585.06
3.14	14.35	84.86	0.00
3.84	-3.40	8.54	0.00

The existence of the obstacle causes less dependency of source strength Q on wind speed V.

CHAPTER IV. RESULTS AND CONCLUSIONS

Theoretical Source Strength

Consider a mass of particles rising due to the impact of oncoming particles. Let's assume that all particles rise with the initial velocity $\vec{V}_1 = V_1\vec{i} + W_1\vec{k}$ and the final impact velocity $\vec{V}_2 = V_2\vec{i} + W_2\vec{k}$ (Figure 30), where $\vec{i}$ and $\vec{k}$ are unit vectors along the x (i.e., wind direction) and z (i.e., perpendicular to the ground) directions, respectively.

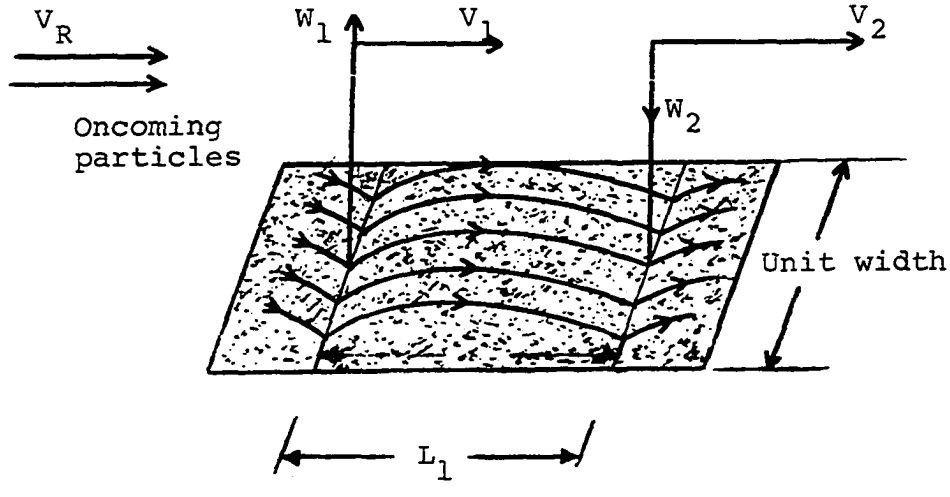

Figure 30. Sand size particles in saltation along characteristic paths

It is assumed that all particles travel along similar flight paths over a distance L_1. This flight path is called the characteristic of average flight path. It is thought of as an average of all possible flight paths encountered for a collection of particles.

If Q is the total particulate mass per unit width per second, traveling a distance L_1 (Figure 10), then the total momentum loss of the wind per unit area of travel (i.e., $L_1 x 1$) per second is presented as

$$\frac{\text{Total momentum exchange}}{\text{Unit area-second}} = \frac{Q(V_2 - V_1)}{L_1} \tag{9}$$

The rate of change of momentum is equal to a force. The force in this case is the resistance which is exerted from the surface of the moving particles to the air flow. This force per unit surface area is the friction shear stress $\tau = \rho V_*^2$, where ρ is the density and V_* is the friction or drag velocity. Since V_1 is small compared to V_2, Equation 9 can be written as

$$\rho V_*^2 = \frac{QV_2}{L} . \tag{10}$$

It is suggested (18) that $\frac{V_2}{L}$ is approximately equal to $\frac{g}{W_1}$, where g is the gravitational acceleration.

From Equation 10, one can substitute for $\frac{V_2}{L}$ and obtain the following equation

$$Q = \frac{\rho W_1 V_*^2}{g} \quad . \tag{11}$$

The value W_1 is related to the friction speed V_*. This is due to the fact that W_1 is controlled by the final velocity of the falling or oncoming particles. The falling particles obtain their final speed due to the gradient of wind speed which in turn is dependent on V_*. Therefore, W_1 is assumed to be proportional to V_*. The constant of proportionality is a coefficient c which is dependent on the type of particles in question.

$$W_1 = cV_* \quad . \tag{12}$$

By substituting Equation 12 into Equation 11, the following equation is derived

$$Q = \frac{C\rho V_*^3}{g} \qquad \text{(Bagnold (18))} \tag{13}$$

The values of the constant C are given by Bagnold (18) for different ranges of grain diameter.

It can be seen that $\frac{Qg}{\rho V_*^3}$ is a dimensionless quantity equal to the coefficient C and thus, Q must vary with the cube of the wind speed. Although Bagnold's equation (Equation 18) is derived strictly for particles in saltation, it is also still dimensionally correct for smaller particles which are transported in the suspension mode as in the present series of experiments.

Modification of Bagnold's equation

Since the derivation of Equation 13 in the 1930s by Bagnold, many experimental and field data have been presented by others, either in substantiation or in disregard of the relation between Q and V_* presented by Bagnold. The values of Q and V_R are often plotted on log-log scales, and presented as straight lines. The slope of the lines corresponds to the power of wind speed in the following equation.

$$Q = AV_R^{\,n} \ . \tag{14}$$

However, the values of n have been shown to vary between 1 to 10 (see Table 1). Therefore, the presentation of strength versus V_R as is shown by Equation 14 has not yet been generalized nor has it been substantiated theoretically.

Equation 13, on the other hand, has shown to be in good agreement with some experimental and field observations for larger values of wind speed. This can be observed from Figures 31 through 33 where the power n is at low wind speeds larger than 3 but for larger wind speeds becomes equal to 3. Naturally, if experimental data are taken for low ranges of wind speed, the power n will thus be larger than 3. If the wind speed is increased, the relation between Q and V becomes a cubic function of V.

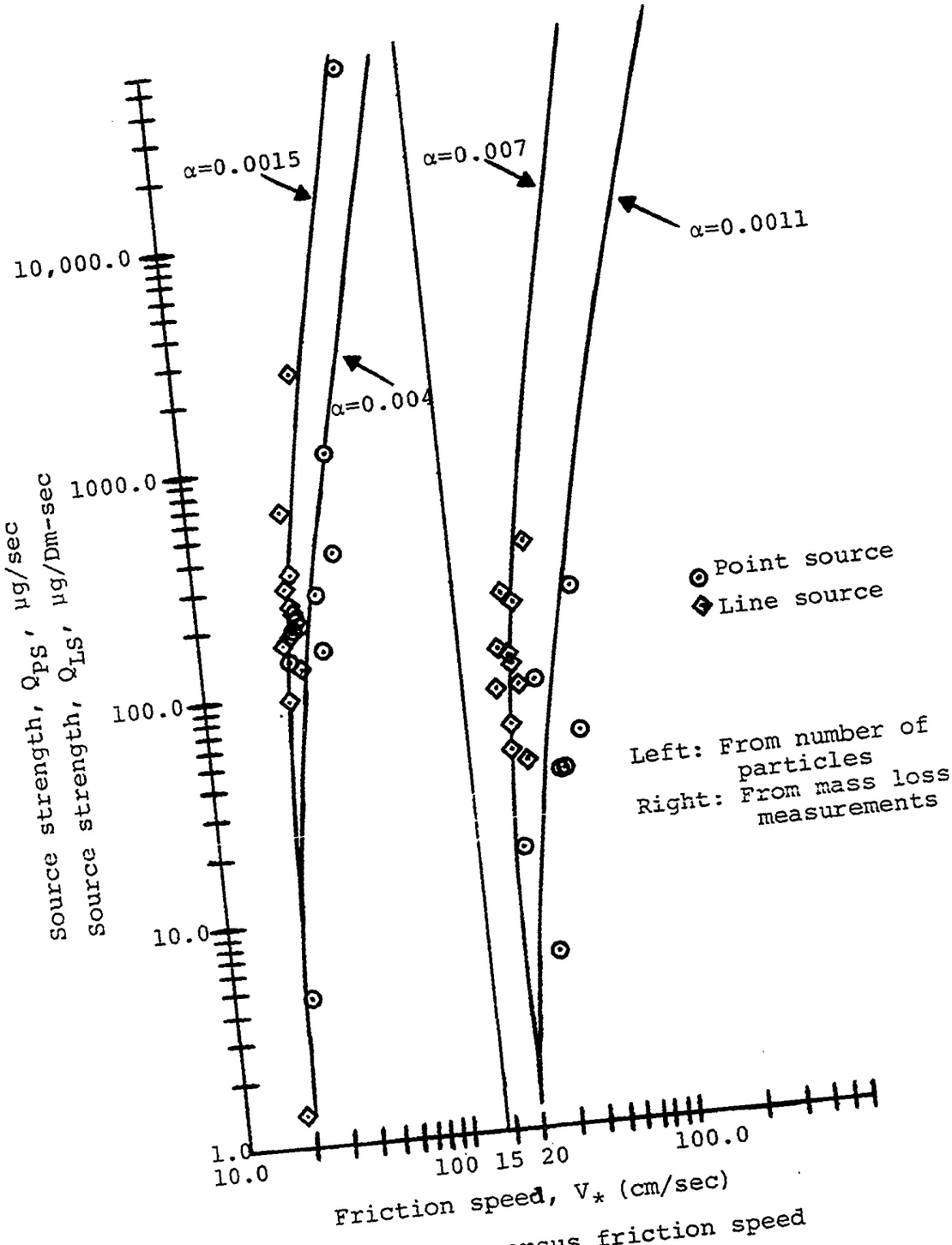

Figure 31. Source strength versus friction speed

The Q and V relationship is apparently more complicated than exemplified by Equations 13 and 14. On the other hand, Equation 13 seems to be a limiting case for large V_* for which Q becomes proportional to V_*^3. The following equation is suggested here, to cover all ranges of wind speed

$$Q = \frac{C\rho V_*^3}{g} \quad f\left(\frac{V_*}{V_{*t}}\right) \tag{15}$$

The function $f\left(\frac{V_*}{V_{*t}}\right)$ could be an exponential function which at higher values of velocity approaches unity, such that

$$\lim_{V_* \to \infty} f\left(\frac{V_*}{V_{*t}}\right) = 1 \tag{16}$$

$$V_{*t} = \text{constant}$$

and at $V_* = V_{*t}$ the function f must be zero.

$$\lim_{V_* \to V_{*t}} f\left(\frac{V_*}{V_{*t}}\right) = 0 \tag{17}$$

A function which satisfies conditions 16 and 17 is presented as

$$f\left(\frac{V_*}{V_{*t}}\right) = 1 - e^{-\alpha\left(\frac{V_*}{V_{*t}} - 1\right)} \tag{18}$$

By substituting Equation 18 into Equation 15 the following formula is obtained

$$Q = \frac{C\rho V_*^3}{g} \left(1-e^{-\alpha\left(\frac{V_*}{V_{*t}} - 1\right)}\right). \qquad (19)$$

Where α is a constant to be determined.

Source Strength

The line and point source strength were determined using two methods of measurements; first, from measurement of mass loss after each test run, and second, from the integration of the number of particles per square millimeter versus distance diagrams (i.e., by determining the number of particles diffused). Figure 31 displays the results for both types of measurements and for both sources. As was shown in Chapter III, a straight line polynomial fit through the data of Figure 31 resulted in Equations 5 and 8 for the point and the line source, respectively. The values of n obtained were 6.35 and 10.35 (Table 1). These new values of n do not agree with any previously determined powers of wind speed.

If, on the other hand, Equation 19 is used, not only a good fit through the data is obtained, but it also agrees with Bagnold's equation (13). The only factor different in each case in Figure 31 is the value of the constant α. This coefficient could be found either by trial and error or could be determined from Equation 19, by substituting for V_*

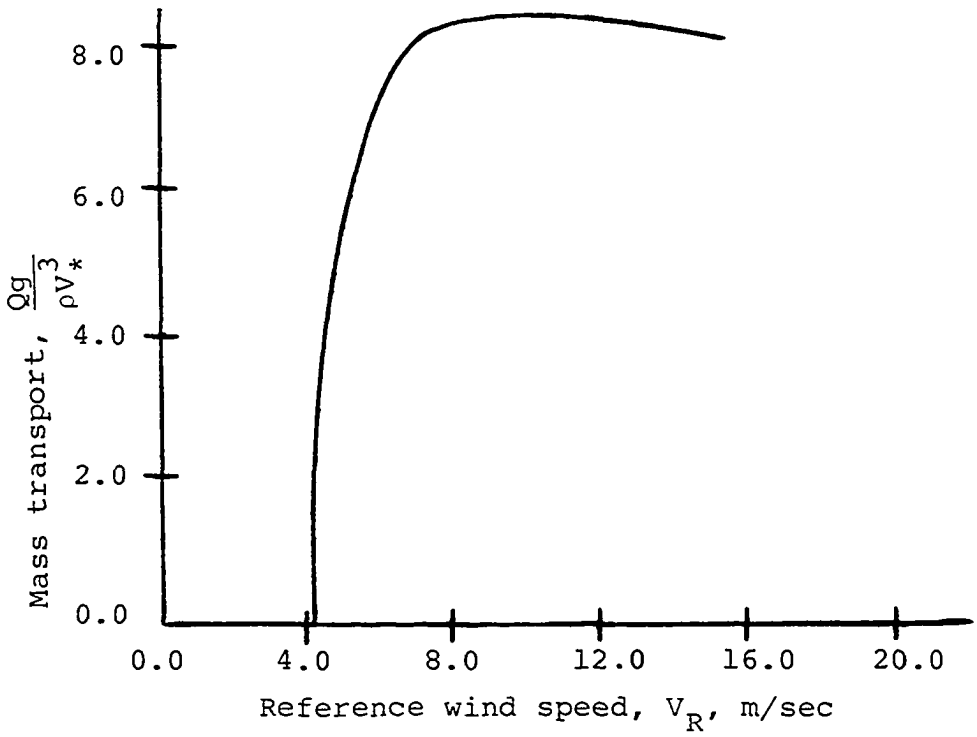

Figure 32. $\frac{Qg}{\rho V_*^3}$ versus V_R (Budd, Dingle, Radok (31))

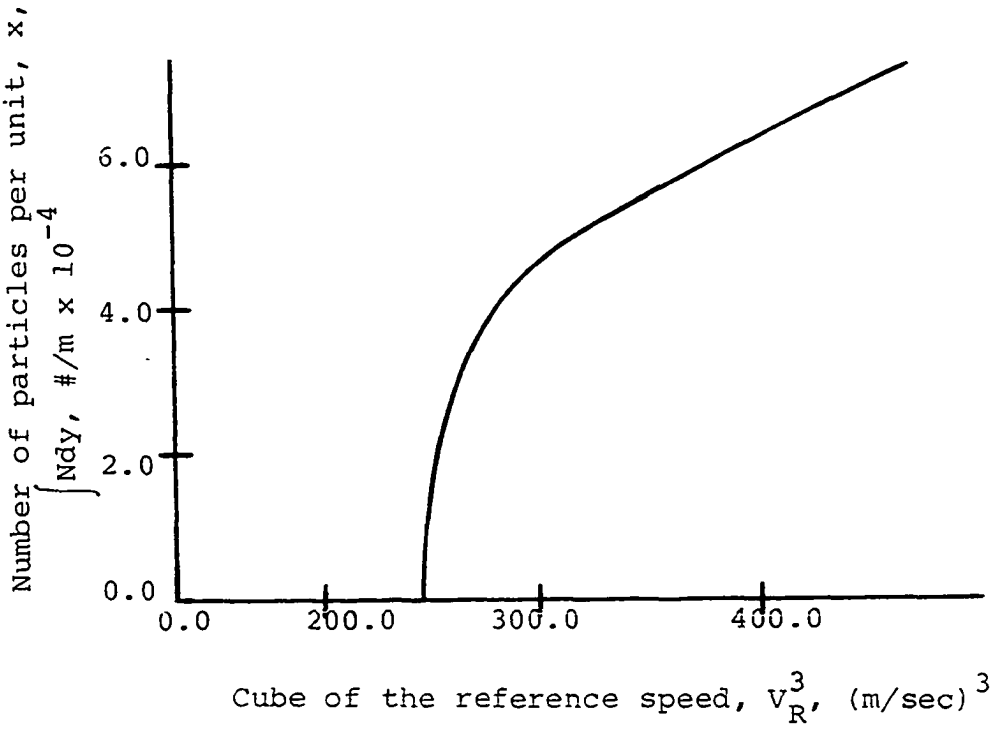

Figure 33. $\int$Ndy versus V_R^3 (Iversen (2))

and Q from the data.

In comparison with Figure 32, which is a result from blowing snow at Z = 10.0 meters wind speeds, it is seen that Equation 13 holds true for winds above 7.0 m/sec. On the other hand, for wind speeds below 7.0 m/sec, a higher degree polynomial with a power n larger than 3 would perhaps fit the data. Almost a similar situation is seen from Figure 33. Here, the $\int Ndy$ is the number of particles per unit y lateral distance due to diffusion of lycopodium spores from a model of a coal dumping site (2). For wind speeds above 6.69 m/sec, a straight line relation exists between $\int Ndy$ and the cube of the wind speed. At speeds lower than 6.69 m/sec a higher rate of change of V_R is apparent.

Figure 31 shows basically the same type of behavior between Q and V. At friction speeds higher than ≈30.0 cm/sec, the relation 19 approaches a straight line while for values of V_* less than ≈30.0 cm/sec the results show a larger rate of change of V_* relative to Q.

It is clearly demonstrated here that at low wind speeds, the relation between Q and V still is governed by a cubic function of wind speed, modified, however, by an exponential function of the friction speed ratio $\frac{V_*}{V_{*t}}$. This exponential function rapidly approaches unity at higher wind speeds and thus approaches the relation between Q and V of Equation 13.

Concentration Diagrams

The diffusion equation was solved numerically due to point and line source diffusions. The numerical codes were developed and run by Mr. Chin-Shun Lin, Department of Aerospace Engineering, Iowa State University.

The diffusion equation solved numerically is

$$\frac{\partial C_1}{\partial t} + V\frac{\partial C_1}{\partial x} + U\frac{\partial C_1}{\partial y} + W\frac{\partial C_1}{\partial z} = \frac{\partial}{\partial x} K_x\frac{\partial C_1}{\partial x} + \frac{\partial}{\partial y} K_y\frac{\partial C_1}{\partial y}$$

$$+ \frac{\partial}{\partial z} K_z\frac{\partial C_1}{\partial x} \qquad (20)$$

This equation was simplifies by assuming steady state conditions (i.e., $\frac{\partial C_1}{\partial t} = 0$) and by neglecting the terms $U\frac{\partial C_1}{\partial y}$ and $\frac{\partial}{\partial x} K_x \frac{\partial C_1}{\partial x}$. These terms are assumed to be negligible because the three-dimensional concentration C_1 does not vary significantly with time, and since the lateral component of wind speed U is very small, and since the streamwise diffusion term $\frac{\partial}{\partial x} K_x\frac{\partial C_1}{\partial x}$ is negligible compared to the lateral and vertical terms. The diffusion equation becomes

$$V\frac{\partial C_1}{\partial x} + W\frac{\partial C_1}{\partial z} = \frac{\partial}{\partial y} K_y \frac{\partial C_1}{\partial y} + \frac{\partial}{\partial z} K_z \frac{\partial C_1}{\partial z} \qquad (21)$$

The particle velocity component along the z-direction W is assumed to be equal to the terminal velocity of fall V_f. Therefore, Equation 21 can be written as

$$V \frac{\partial C_1}{\partial x} = \frac{\partial}{\partial y} K_y \frac{\partial C_1}{\partial y} + \frac{\partial}{\partial z} K_z \frac{\partial C_1}{\partial z} - V_f \frac{\partial C_1}{\partial z} \tag{22}$$

In Equation 20, the term V is actually the particle velocity profile distribution. However, by assuming that the particles have the same velocity profile as that of the wind (a reasonable assumption for particles so small and light as lycopodium spores), Equation 22 can be written as

$$V_R(z) \frac{\partial C_1}{\partial x} = \frac{\partial}{\partial y} K_y \frac{\partial C_1}{\partial y} + \frac{\partial}{\partial z} K_z \frac{\partial C_1}{\partial z} - V_f \frac{\partial C_1}{\partial z} \tag{23}$$

Equation 23 was solved using the Crank Nicolson method for the concentration C_1 in $\frac{\mu g}{cm^3}$ due to diffusion from the point and the line sources described in Chapter II. The velocity profile $V_R(z)$ is presented in Figure B4 (Appendix B). The terminal velocity of fall equal to 5.64 cm/sec was used from Table 2.

When solving for the line source diffusion, the term $\frac{\partial}{\partial y} K_y \frac{\partial C_1}{\partial y}$ becomes equal to zero, since ideally, there are no concentration variations in the y direction for the two-dimensional diffusion problems. Thus, Equation 23 becomes

$$V_R(z) \frac{\partial C_1}{\partial x} = \frac{\partial}{\partial z} K_z \frac{\partial C_1}{\partial z} - V_f \frac{\partial C_1}{\partial z} . \tag{24}$$

For the point source, however, the differential Equation 23 must be solved in three-dimensional space.

The coefficients of diffusivity were assumed to have the following relations with other test parameters

$$K_z = KV_*Z \tag{25}$$

and

$$K_y = KV_*Z \tag{26}$$

where K is the Von Karman constant.

The initial conditions for a line and a point source are infinite concentration at the source. Equations 23 and 24 are elliptic partial differential equations. The initial and the boundary conditions for this type of equation have to be well-posed. Clearly, $C_1 = \infty$ at $x = y = z = 0$ is not a well-posed initial condition. To overcome this problem, the experimental concentrations at a close distance downwind of the line source were used as initial conditions. In case of the point source, a Gaussian initial condition was assumed.

The boundary condition used in the vertical direction was $C_1 = e^{A_1+B_1Z+D_1Z^2}$ for lower heights, such that at z=0 the concentration C_1 is a constant e^{A_1}. For the higher regions, the boundary condition was changed to $C = e^{-(A_1+B_1Z+D_1Z^2)}$ such that at $z=\infty$, the concentration becomes equal to zero. Note that A_1, B_1 and D_1 are numerical constants and are determined for each test run.

It should be mentioned that the solution of the numerical

methods used here (i.e., C_1), has units of $\frac{\mu g}{mm^3}$. Further, the numerical values of C_1 correspond to a source of unit strength. In order to make comparisons with the ground level concentrations obtained from the experiments, the following corrections were made.

$$C_1 \times V_D \times \Delta T \times Q \times F_1 = N_{Nu} \frac{\#}{mm^2} \tag{27}$$

where V_b is the deposition velocity, ΔT is the duration of each test run, Q is the experimentally determined source strength and F_1 is a conversion factor in $\frac{\#}{\mu g}$ for lycopodium spores.

Comparison with numerical results

Figures 34 and 35 are the numerical results due to diffusions from the line source. These figures correspond to Figures 23 and 26 of Chapter III. It is seen that the numerical concentrations are underpredicted at the peak or the maximum N_{Nu}'s. However, the position of the maximum concentration is predicted at 14 cm downwind of the source while the experimental results show this position to be somewhere between 6.0 cm and 11.0 cm. On the other hand, the downwind numerical predictions away from the peak are very close to the test results.

Figure 36 is the numerical result due to diffusion from the point source. Due to the expense of computer time required

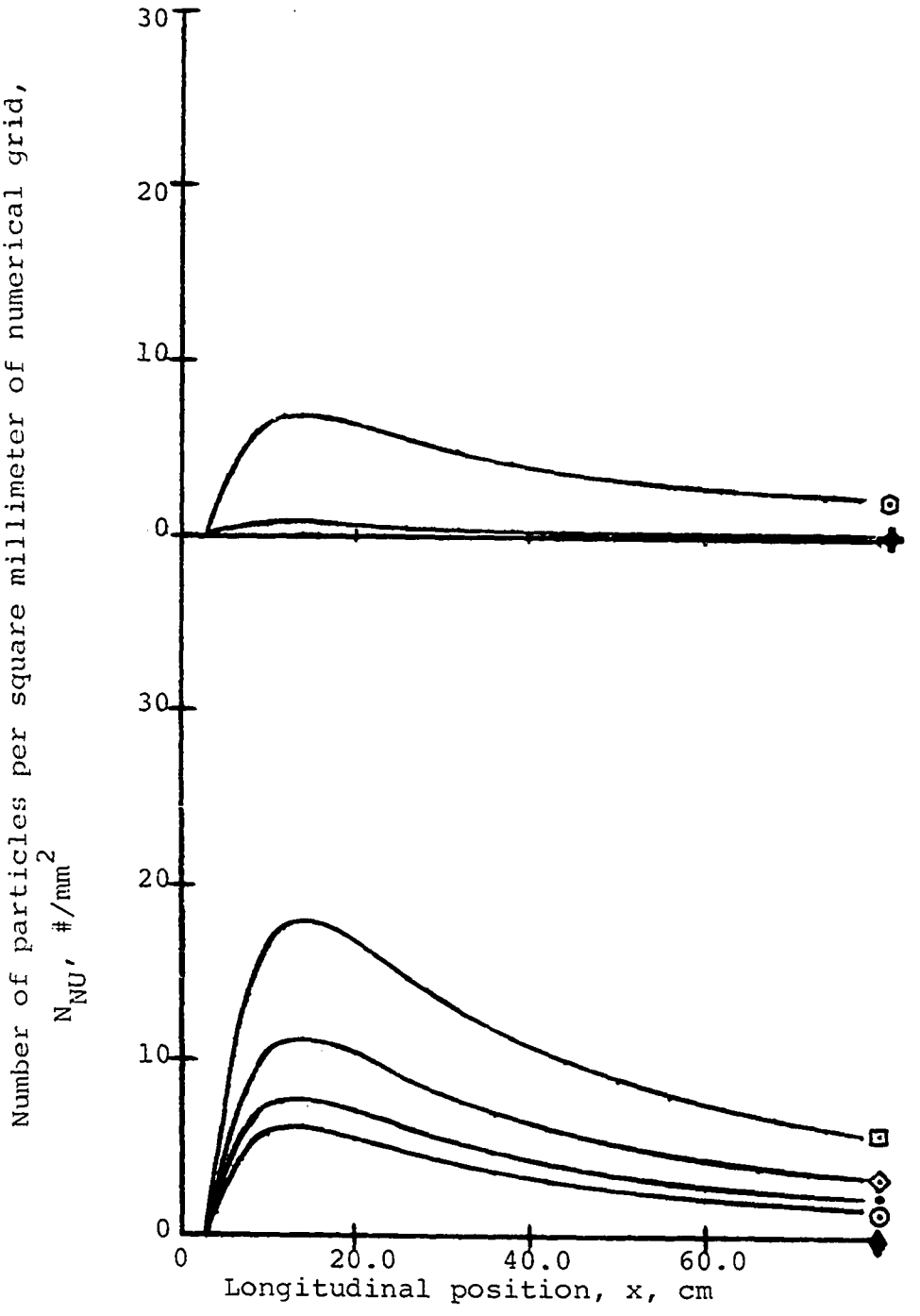

Figure 34. N_{NU} versus x for line source

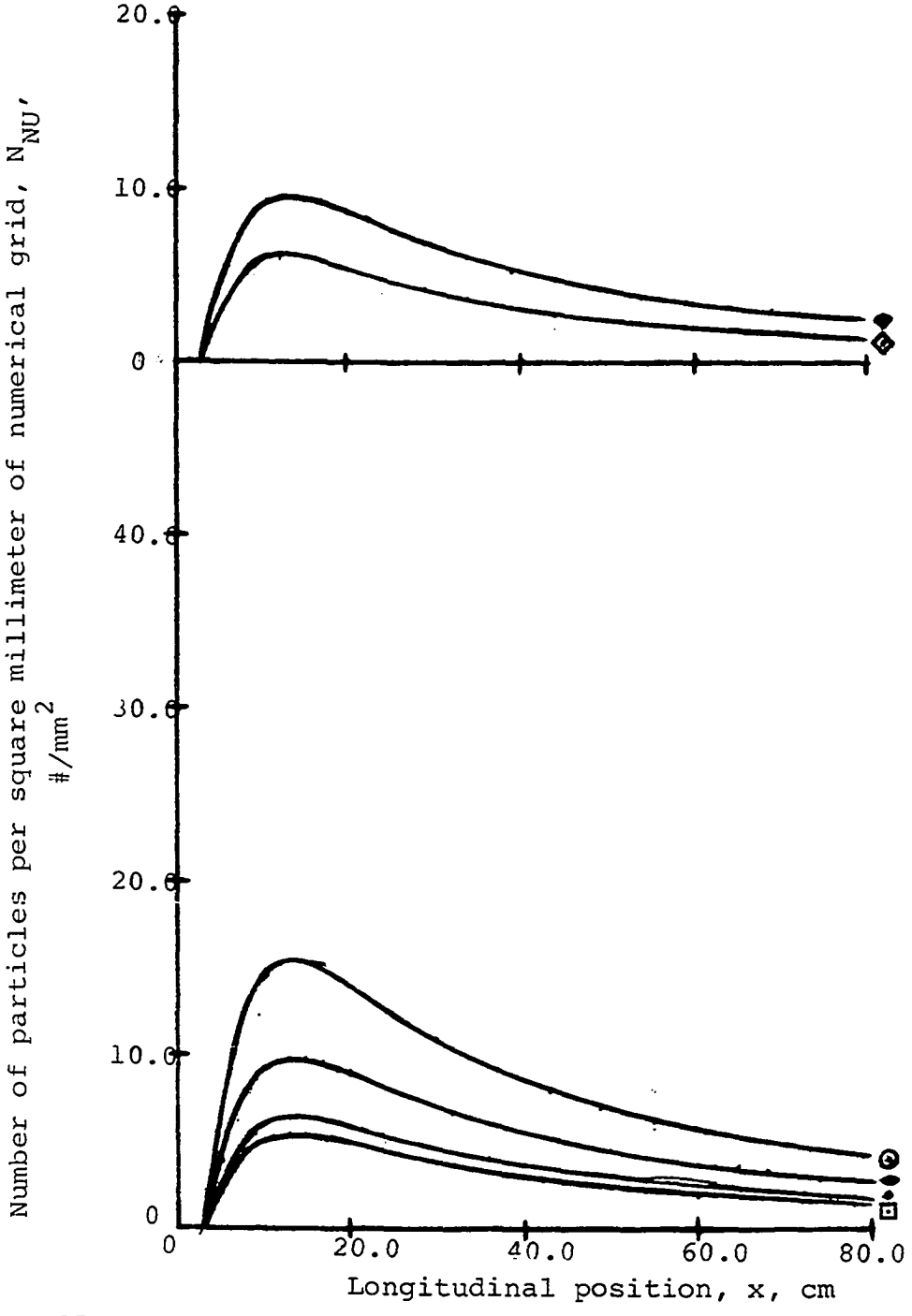

Figure 35. N_{NU} versus x for line source with the three-dimensional obstacle neglected

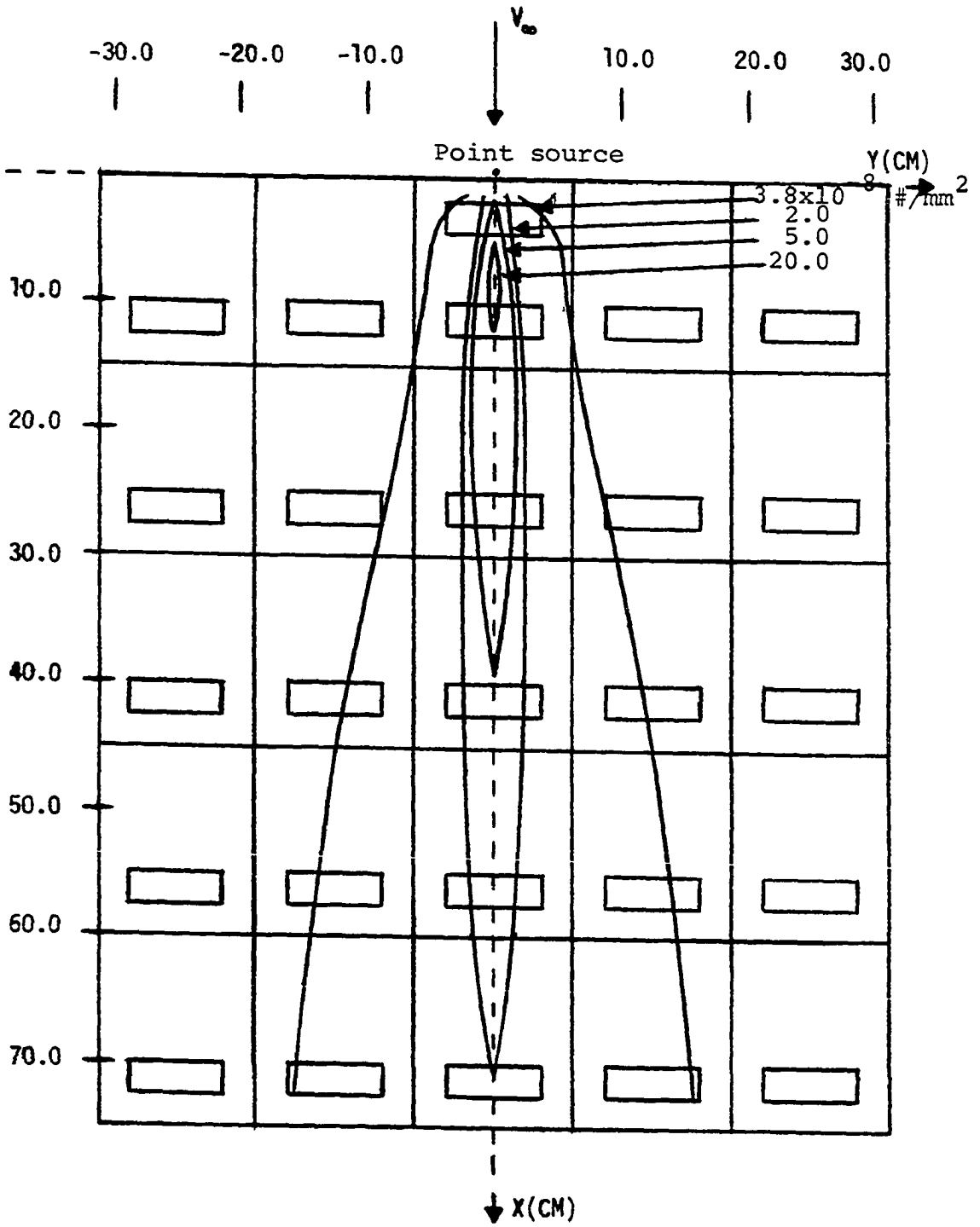

Figure 36. Numerical isolines for point source diffusion at V_R = 5.45 m/sec

to solve the diffusion problem in three-dimensional space, only one solution is presented here. It can be seen that in comparison with Figure A7 in Appendix A, the numerical predictions are not in total agreement with the results of the experiment. The most noticeable differences are: First, the isolines of the numerical solutions are narrower and much longer. In other words, in the numerical results, less particles are deposited over longer longitudinal and shorter lateral lengths, whereas, the experimental results have shown more deposition at closer longitudinal but larger lateral lengths. Second, the maximum concentration due to the numerical results is located inside of the 20.0 $\#/mm^2$ isoline at $x = 7.5$ cm and $y = 0.00$, and has a value of $\simeq 24.0$ $\#/mm^2$. The experimental results show a maximum value of 55 $\#/mm^2$ at $0.0 < x < 5.0$ cm and $y = 0.0$.

The only agreement between the two sets of results is that the maximum concentration is in both cases along the central axis.

The reasons for the discrepancies between the experimental and the numerical results could be one or any combination of the following.

1. The most important factor is perhaps the variation of the wind boundary layer in the vicinity of the sources. That is, the wind profile near the sources would be different from that of the clean test section. Note, that in the numerical

code the wind tunnel (clean test section) velocity profile was used to present the wind structure everywhere.

It is seen from Figures B1 through B3 that in the wake of the two and the three-dimensional obstacles the wind speeds near the wake of the obstructions are lower compared to distances farther downwind. The sources used here are themselves obstructions. Therefore, the wind speed in the wake of the sources would be lower than at distances downwind. Since the wind speed is low here, more particles will be released from the wind stream and become trapped on the greased slides.

2. Another factor could be due to experimental errors in determining Q. The number of particles obtained from the integration of the $\#/mm^2$ versus distance diagrams or the total mass loss from each source, were used to determine Q. These strengths could very well be smaller than the actual strengths since many particles could have escaped the test section without being deposited. This would result in error when particles are counted. On the other hand, the measurements of mass loss were not accurate, since too much error was introduced in measuring small losses of mass in the order of 10^{-1} to 10^{-4} grams.

3. The cohesive force between the particles and resulting agglomeration could have been another reason for heavy accumulations near the sources. Figure 6 shows that the particles

might have been influenced by this force, since some of them have gathered in small groups very close to each other.

4. The deposition velocity could vary with distance x (26). If so, then the numerical predictions should also be subjected to a variable deposition velocity V_D. In fact, when the deposition velocity was changed from 5.64 m/sec to 10.0 m/sec a larger concentration peak was obtained from the numerical results. However, the numerical results were still underpredicting the peak values.

Since no knowledge of V_D variations with distance are known, the subject is left for future investigations.

5. It was assumed that source strength remains unchanged with time. However, it could very well be that strength decreases with time because of depletion of the source. Again, no information is available on this aspect of the study and thus could not be pursued any further.

6. The assumptions made in modification of Equation 20 and the adopted initial and boundary conditions may have some influence on the final solution. However, their influence is perhaps negligible compared to those mentioned in 1 through 5 above.

7. Finally, the sources examined in the laboratory were not exactly point or line sources but had finite surface areas, while the numerical sources were mathematically fixed to have zero areas. This could be one reason for the numerical

solution of the point source to result in narrower isoline diagrams than the experimental results (Figures 36 and A7).

Comparison with other field and experimental results

It is not possible at this point to provide bases for any kind of a quantitative comparison with the concentration data obtained during other studies. This is due to the fact that the physical and the geometric conditions under which each study was carried on are different in each case. Therefore, the following are attempts to make qualitative comparisons with some available published data.

The results obtained from a study on lycopodium spores diffusion from the wind tunnel test of a dumping site of a model power plant is shown in Figure 37. It is seen that in comparison with point source diffusion date of the present study, there are some agreements between the two sets of data. First, it is evident that the maximum concentration lies along the central longitudinal axis through the center of the source. Second, it is seen that the concentration diagram at downwind distances tend to become flat. Even though the data presented in Figure 37 have units of $\#/mm^2$ versus distance, it will not be possible to make any kind of quantitative comparison with the results of the present work. The basic differences are due to the model buildings and construction sites in addition to the fact that the point source in Figure 37 was located on top of a larger pile of

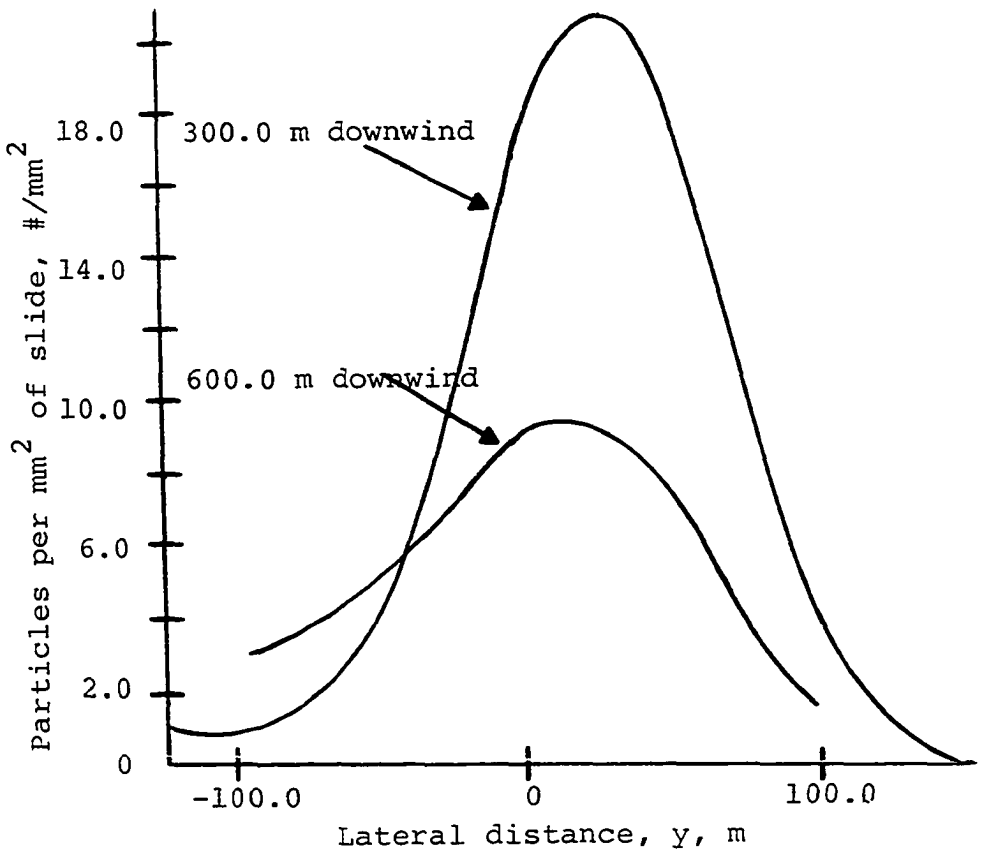

Figure 37. Number of particles per mm^2 versus lateral distance (Iversen (2))

lycopodium spores.

Further comparisons could be made with Figures 1 and 2 of Chapter I. It can be seen that concentration of coal dust decreases with downwind distance in approximately an exponential manner. This is in agreement with the results obtained during the present study. The ground level concentration diagrams due to point and line source diffusion presented in this study at least agree that at some short distance downwind of the sources ($0.0 < x < 9.0$ cm), an exponential drop of concentration begins and continues with x.

Conclusions

Due to the diffusion of lycopodium spores from point and line sources, in the absence and in the presence of a two- or three-dimensional obstruction, the following conclusions are made on the ground level concentration distribution of particles.

Point source

The concentration distribution due to point source diffusion at each longitudinal position, downwind of the source is similar to a Gaussian distribution. The distribution at distances close to the source have a larger peak covering smaller lateral lengths. At downwind distances, the

concentration distributions become flatter, such that the peak values are considerably reduced but the particles cover a larger lateral extent compared to distances closer to the source.

The total number of deposited particles per longitudinal downwind position is decreased with increasing x, until a distance of $x \approx 30.0$ cm is reached. After $x \approx 30.0$ cm, the total number of particles continued decreasing at a lower rate.

From the isolines of constant concentration it is observed that the shape of the isolines were almost similar between each test run. Further, the number of particles per unit area decreased at a faster rate with lateral distances compared to decreases along the longitudinal axis. Finally, it is concluded that the largest concentration isolines are perhaps located between $0.0 < x < 2.0$ cm and $-0.8 < y < 0.8$ cm.

Line source

The average lateral concentrations at each longitudinal position are plotted as functions of downwind distance. It is found that at $x \approx 9.0$ cm, the number of particles per unit area is a maximum. For $x < 9.0$ cm there are less particle concentrations. For $x > 9.0$ cm, the concentration decreases exponentially with x.

From the isolines of constant concentration it is observed that in general, the isolines which are farther downwind are straighter. This is perhaps due to the possible three-dimensional effects which might have been encountered nearby the source. At distances far downwind, the three-dimensional effects diminish as momentum is exchanged with the main wind flow.

Two-dimensional obstacle

It is found that the two-dimensional obstruction creates a discontinuity in the longitudinal concentration distribution. The size of this obstacle is apparently large enough to keep most of the diffused particles on the upstream side of its position. The total maximum number of particles per unit x position upstream compared to downstream of the obstacle in case of the point source is on the order of 9.0-14.0: 1.0 ratio. While, for the line source, the maximum number of particles per unit area upstream and downstream of the obstruction are of the order of 4.0-7.0:1.0 ratio.

From the isoline diagrams, it can be concluded that when the two-dimensional obstacle is present, more particles are trapped upstream of the obstacle position. The distribution of the isolines in this region are similar to those of the sources in the absence of the obstructions.

In case of the line source, the downwind concentration

distributions from the obstacle are similar to other isolines, however, they are much less populated. The obstacle in this case is almost acting as a very weak line source, creating very small depositions downwind. The two-dimensional obstacle at the upstream side of the line source is able to completely stop the mass flow rate when positioned immediately adjacent to the source.

The downwind isolines in the case of the point source, however, looked quite different with the obstacle present. This region downwind of the obstacle is almost uniformly covered by particles (see Figure 18b).

Three-dimensional obstacle

The three-dimensional obstacle has a very limited effect on the distribution of concentration. This of course could be explained from the smaller size of the obstacle compared to its two-dimensional counterpart. It is found that at speeds below 6.35 m/sec there are no particles deposited immediately downwind of the obstacle. This is because no particles entered this region (Figure 16). At faster wind speeds ($\simeq$ 6.65 m/sec), the particles are carried over and/or around the obstacle to be deposited on the central region on the immediate downwind slide. In this case, the slide would have no deposition on the lateral sides due to locally high wind speeds which keep the particles from striking the surface

(Figure 17).

The isolines of constant concentration are drawn for cases when the reference wind speed is less than or equal to 6.35 m/sec. It is observed that the effects of the obstruction are limited to downwind distances equal to ≈15.0 cm from the obstacle. The lateral variations of concentration affected by the obstacle are limited to $-1.5 < y < 1.5$ cm.

It is observed that when the obstacle is positioned just upstream of the source, its downwind effects are carried to distances equal to approximately 30.0 cm from the source (Figure A17b).

In general, the isolines at the immediate downwind position of the obstacle increase with x and y until they reach the concentration values of the main flow at sufficient distances from the obstacle.

Strength

It is shown that a complicated relationship exists between Q and V such that in its limiting case, when $V \to \infty$, it becomes similar to Bagnold's equation.

$$Q = \frac{C\rho V_*^3}{g} \left(1 - e^{-\alpha\left(\frac{V_*}{V_{*t}} - 1\right)}\right) \tag{19}$$

which takes into account the ratio of friction speed to its value at threshold is shown to well represent the data obtained during this study.

It can be seen from Figure 31 that the slope of the

Q versus V_* curve for the point source is always smaller than that of the line source. This correlation between the two methods of measurement suggests that even though some error might have been introduced (due to mass loss measurements or the counting of the particles) in calculating the source strengths, nevertheless, the results appear to be consistent.

Thoughts about Future Studies

Attention should be focused on the development of numerical methods. In order to make any progress in the perfection of the numerical schemes, much more must be known about the physical mechanism concerning the nature of diffusing and eventually depositing particulates.

Earlier in this chapter, the numerical results for the surface concentrations of lycopodium spores were compared with the experimental results. There were some suggestions made in an attempt to diagnose the main reasons for the disagreements between the results. For future studies, items 1 through 7 on pages 93-95 of this dissertation should be investigated thoroughly. A primary objective would be to place surface source strength estimation on a firmer basis so that source strengths can be estimated for wind tunnel tests with more complicated geometry, for which numerical calculations are as yet impossible (such as trees, buildings, etc.).

REFERENCES

1. Smit, P. P. A., P. H. M. te Riele and P. C. Richards. "Air Pollution by Coal Dust." Proceedings of the 12th International Colloquium on Atmospheric Pollution, Paris, France, 1976.

2. Iversen, J. D. "Wind Transportation of Dust from Coal Piles." Danish Ship Research Laboratory, SL Report 81054, Oct. 1981.

3. Bosanquet, C. H. and J. L. Pearson. "The Spread of Smoke and Gases from Chimneys." Transactions, Faraday Society, 32 (1936), 1249-1264.

4. Sutton, O. G. "The Theoretical Distribution of Airborne Pollution from Factory Chimneys." Quarterly Journal of Royal Meteorology Society, 73 (1947), 426-436.

5. Barad, M. L. and D. A. Haugen. "A Preliminary Evaluation of Sutton's Hypothesis for Diffusion from a Continuous Point Source." Journal of Meteorology, 16 (February 1959), 12-20.

6. Yordanov, D. "Simple Approximation Formulae for Determining the Concentration Distribution of High Sources." Atmospheric Environment, 6 (1972), 389-398.

7. Sehmel, G. A. "Particle and Gas Dry Deposition: A Review." Atmospheric Environment, 14 (1980), 983-1011.

8. Gillette, D. and P. A. Goodwin. "Microscale Transport of Sand-Sized Soil Aggregates Eroded by Wind." Journal of Geophysical Research, 79, No. 27 (September 20, 1974), 4080-4084.

9. McTigue, D. F. "Mixture Theory for Suspended Sediment Transport." Journal of the Hydraulics Division, 107, No. HY6 (June 1981), 659-673.

10. Shir, C. C. and L. J. Shieh. "A Generalized Urban Air Pollution Model and Its Application to the Study of SO_2 Distributions in the St. Louis Metropolitan Area." Journal of Applied Meteorology, 13, No. 2 (March 1974), 185-204.

11. Sehmel, G. A. "Particle Diffusivities and Deposition Velocities over a Horizontal Smooth Surface." Journal of Colloid and Interface Science, 37, No. 4 (December 1971), 891-906.

12. Fuquay, J. J., C. L. Simpson and W. T. Hinds. Prediction of Environmental Exposures from Sources near the Ground Based on Hanford Experimental Data." Journal of Applied Meteorology, 3 (December (1964), 761-770.

13. Smith, F. B. "The Diffusion of Smoke from a Continuous Elevated Point Source into a Turbulent Atmosphere." Journal of Fluid Mechanics, 2 (1957), 49-76.

14. Hino, M. "Computer Experiment on Smoke Diffusio over Complicated Topography." Atmospheric Environment, 2 (1968), 541-558.

15. Csanady, G. T. "Dispersal of Dust Particles from Elevated Sources." Austrian Journal of Physics, 8 (1955), 545-550.

16. Ermak, D. L. "An Analytical Model for Air Pollutant Transport and Deposition from a Point Source." Atmospheric Environment, 11 (1977), 231-237.

17. Overcamp, T. J. "A General Gaussian Diffusion-Deposition Model for Elevated Point Sources." Journal of Applied Meteorology, 15 (November 1976), 1167-1171.

18. Bagnold, R. A. The Physics of Blown Sand and Desert Dunes. London: Methuen and Co., Ltd., 1941.

19. Ghosh, J. K., B. S. Mazumder and S. Sengupta. "Methods of Computation of Suspended Load from Bed Materials and Flow Parameters." Sedimentology, 28 (1981), 781-791.

20. Chakrabarti, C. and D. R. Lowe. "Diffusion of Sediment on the Lee Dune-Like Bedforms: Theoretical and Numerical Analysis." Sedimentology, 28 (1981), 531-545.

21. Becker, D. L. and E. S. Takle. "Particulate Deposition from Dry Unpaved Roadways." Atmospheric Environment, 13 (1979), 661-668.

22. Iversen, J. D. "Comparison of Wind Tunnel Model and Full Scale Snow Fence Drifts." Journal of Wind Engineering and Industrial Aerodynamics, 8 (1981), 231-249.

23. Iversen, J. D. "Small Scale Modeling of Snow Drift Phenomena." In Wind Tunnel Modeling for Civil Engineering Applications. T. A. Reinhold, ed. Cambridge, Mass.: Cambridge University Press, 1982, 522-545.

24. Smit, P. P. A. "Dust Concentrations Around Coal Stockpiles." The Science of the Total Environment, 15 (1980), 207-216.

25. Aspaugh, L. R., P. L. Phelps, N. C. Kennedy, J. H. Shinn and J. M. Reichman. "Experimental Studies on the Resuspension of Plutonium from Aged Sources at the Nevada Test Site." Proceedings of a Symposium held at Richand, Washington, September 4-6, 1974.

26. Raynor, G. S. "Experimental Studies of Pollen Deposition to Vegetated Surfaces." Proceedings of a Symposium held at Richland, Washington, September 4-6, 1974.

27. Iversen, J. D. and B. R. White. "Saltation Threshold on Earth, Mars and Venus." Sedimentology, 29 (1982), 111-119.

28. Blackwood, T. R. and R. A. Wachter. "Source Assessment, Coal Storage Piles." Environmental Protection Agency report. Contract No. 68-02-1874, Program Element No. IBB610, July 1977.

29. Janssen, L. A. M. "Modelonderzoak aan de Verstuiving van Stortgoed." Symposium Verslag, Utrecht, Ministerie van Volksgezondheid en Milieuhygiëne, March 22, 1979.

30. Gillette, D. "Tests with a Portable Wind Tunnel for Determining Wind Erosion Threshold Velocities." Atmospheric Environment, 12 (1978), 2309-2313.

31. Budd, W. F., R. Dingle and U. Radok. "The Byrd Snow Drift Project: Outline and Basic Results." In Antarctic Research Series, 7 (1965), 71-134.

ACKNOWLEDGMENTS

The author wishes to express appreciation and gratitude to Dr. J. D. Iversen for his guidance during this study. Also, I like to acknowledge Dr. C. T. Hsu, Dr. L. K. Seversike, Dr. R. J. Lambert, Dr. W. J. Cook and Dr. F. M. Graham for serving as committee members and to Mr. Lin for developing the numerical schemes and to Mrs. Pat Gunnells for typing this dissertation.

It is also my wish to acknowledge my father (Ali Moghadam) and mother (Pari Moghadam) for the encouragement and support they have given me during my academic years, especially during the course of this study. Without their support, it would have been a much more difficult task.

APPENDIX A: MORE CONCENTRATION DIAGRAMS

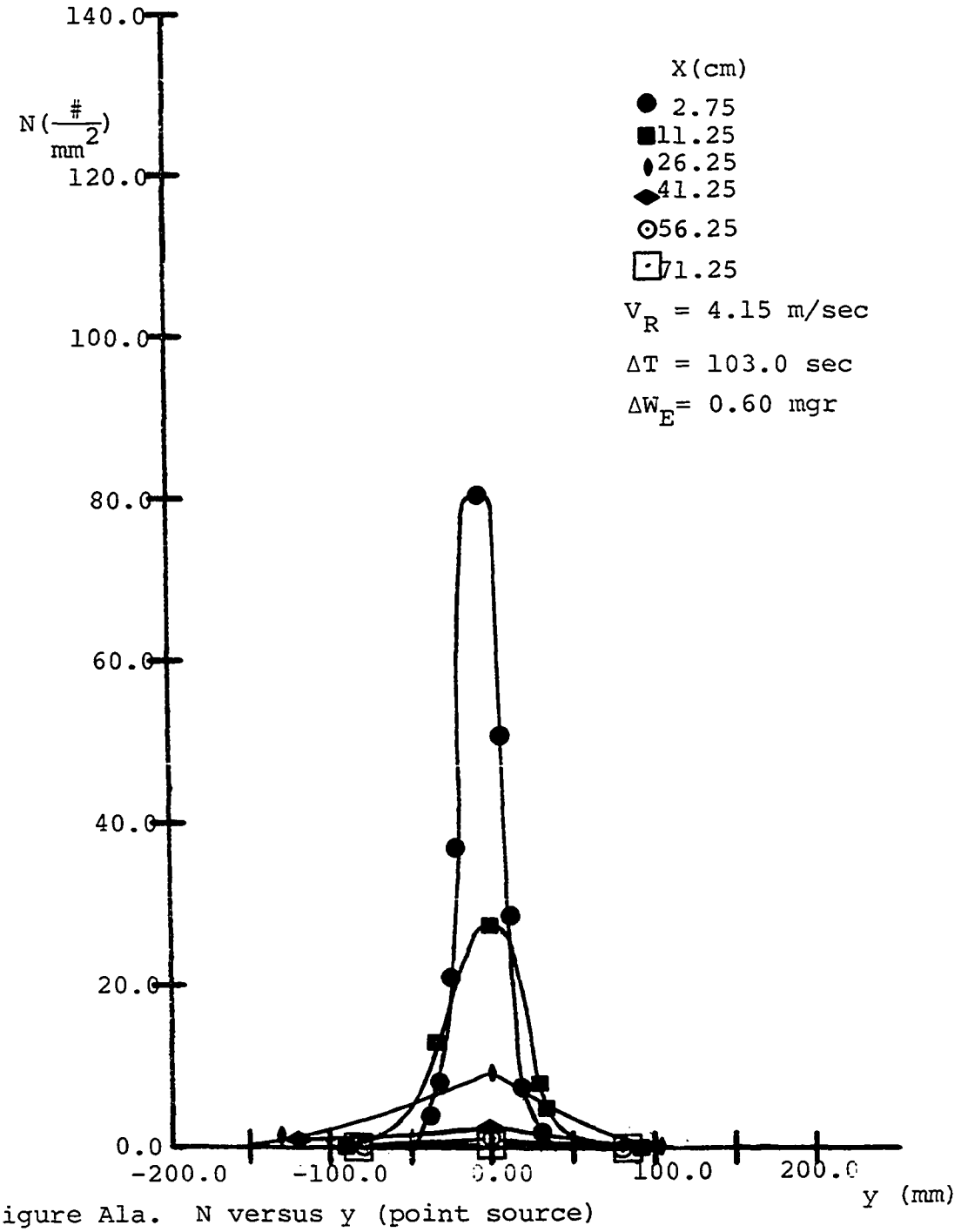

Figure Ala. N versus y (point source)

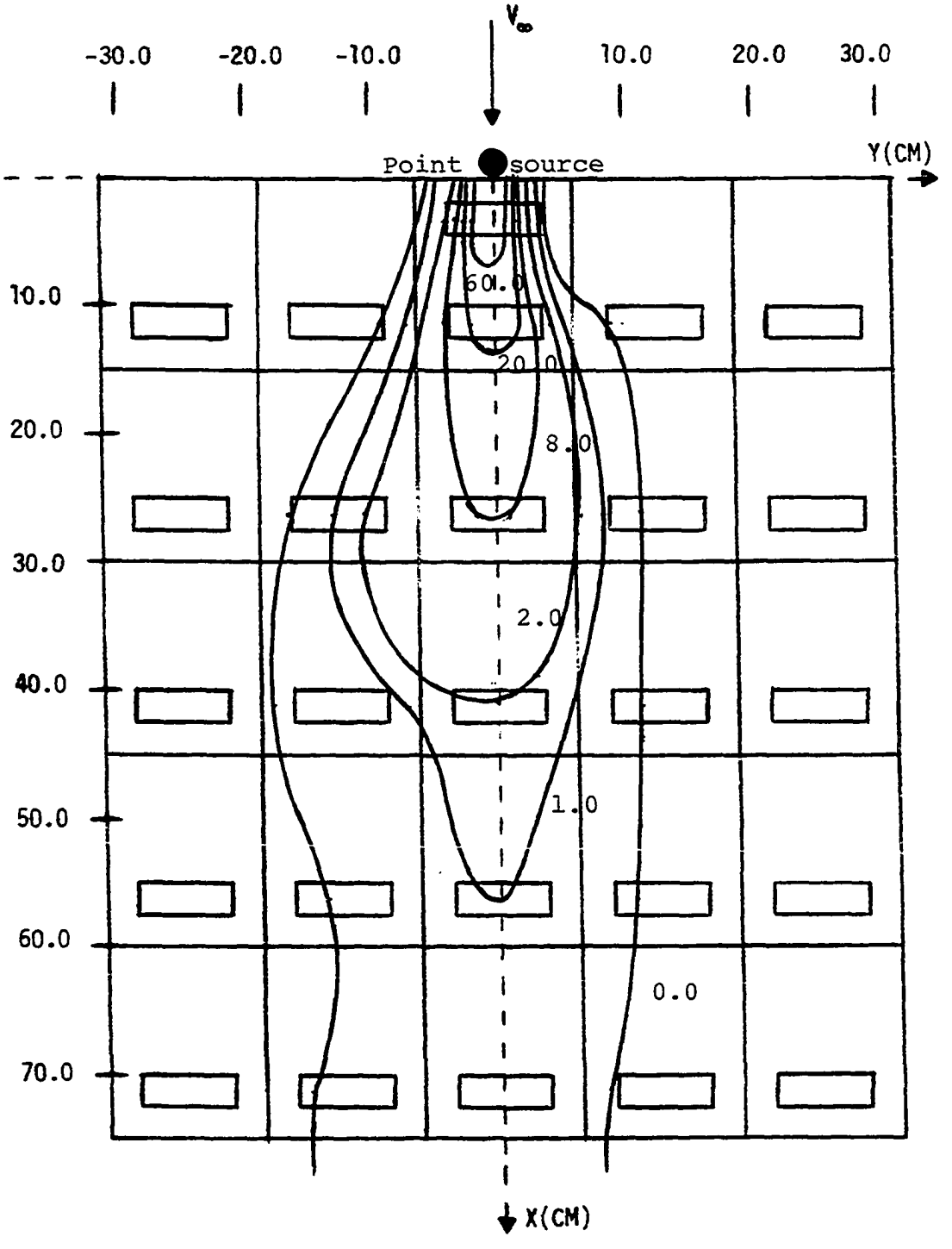

Figure A1b. Concentration isolines (#/mm^2)

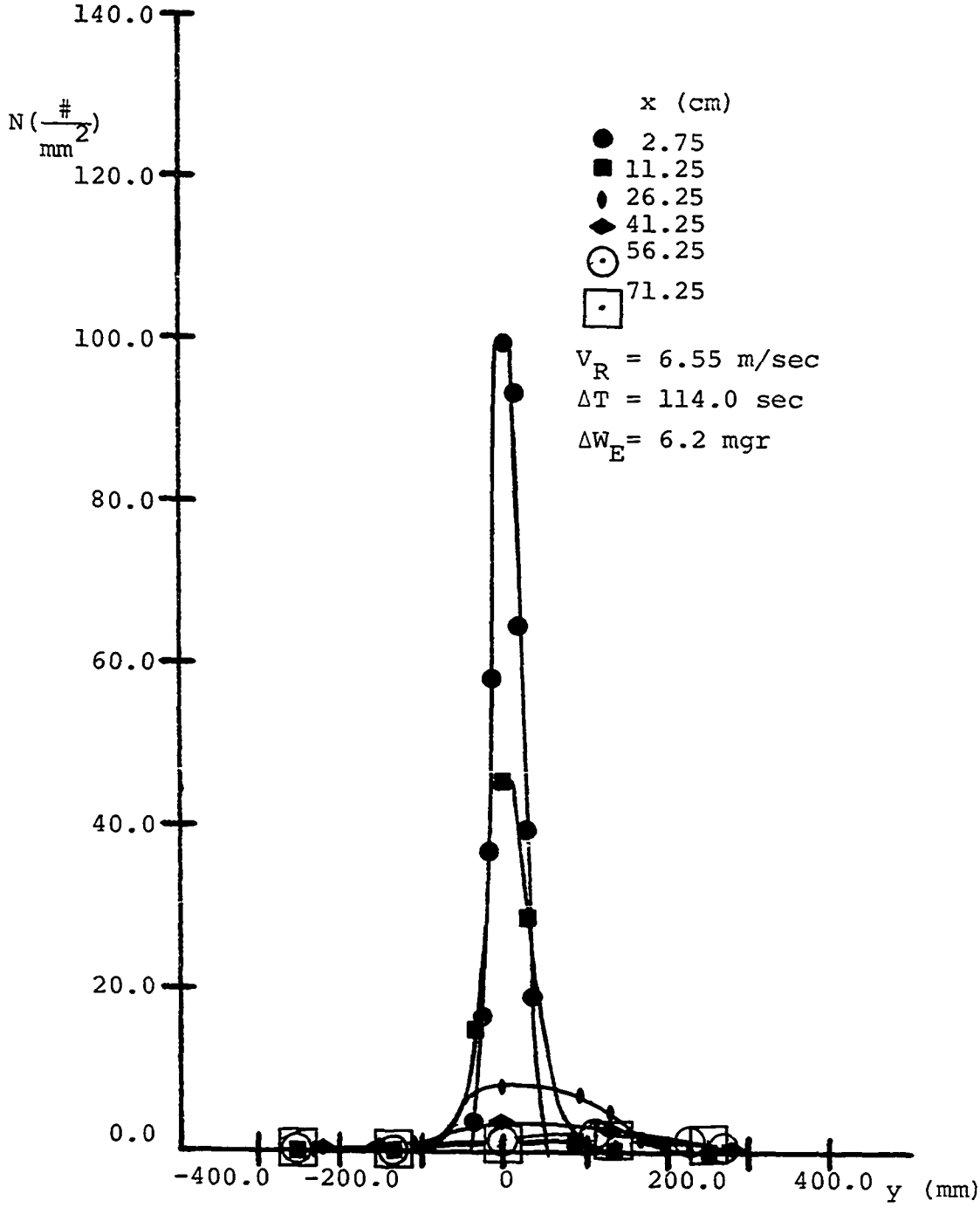

Figure A2a. N versus y (point source)

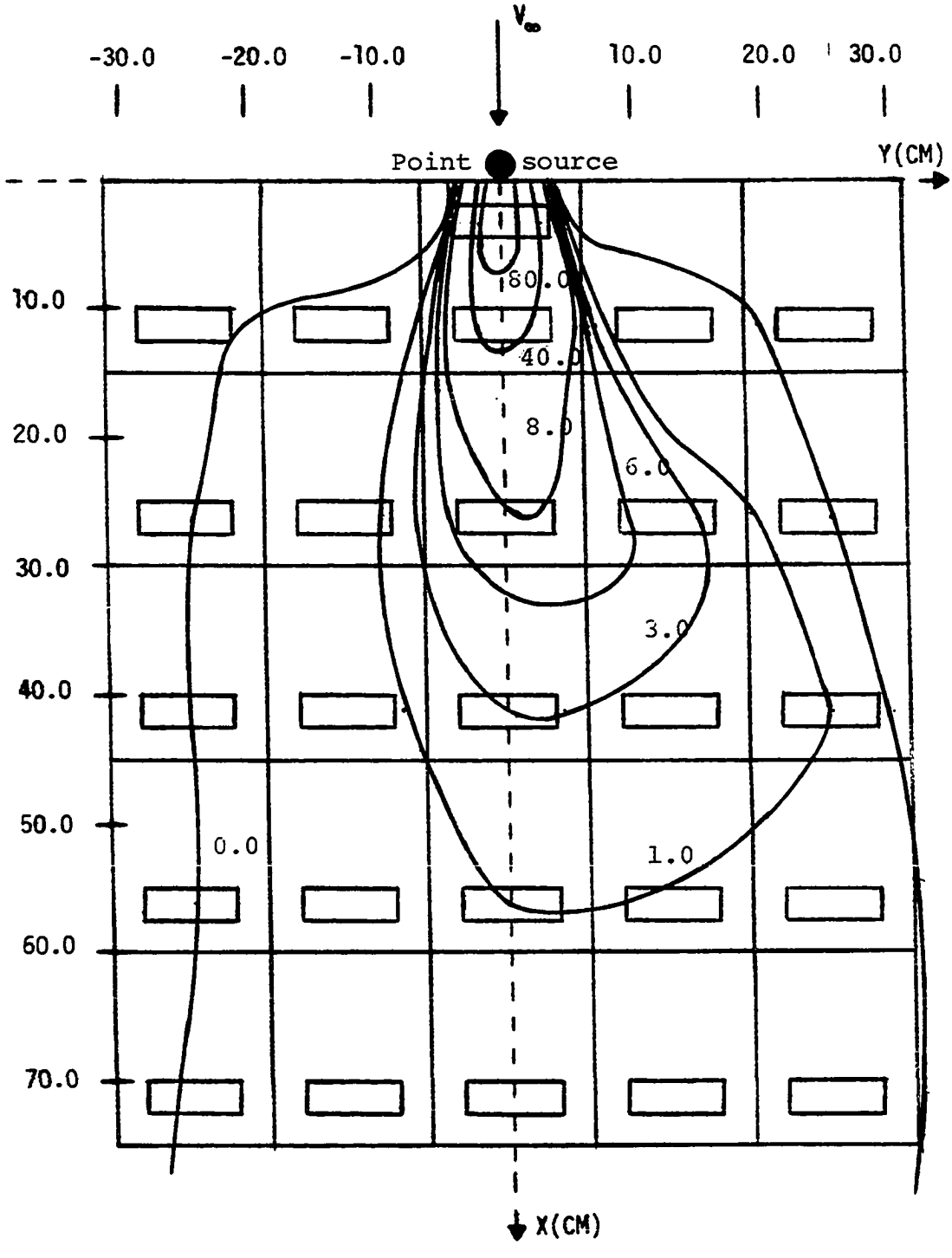

Figure A2b. Concentration isolines (#/mm^2)

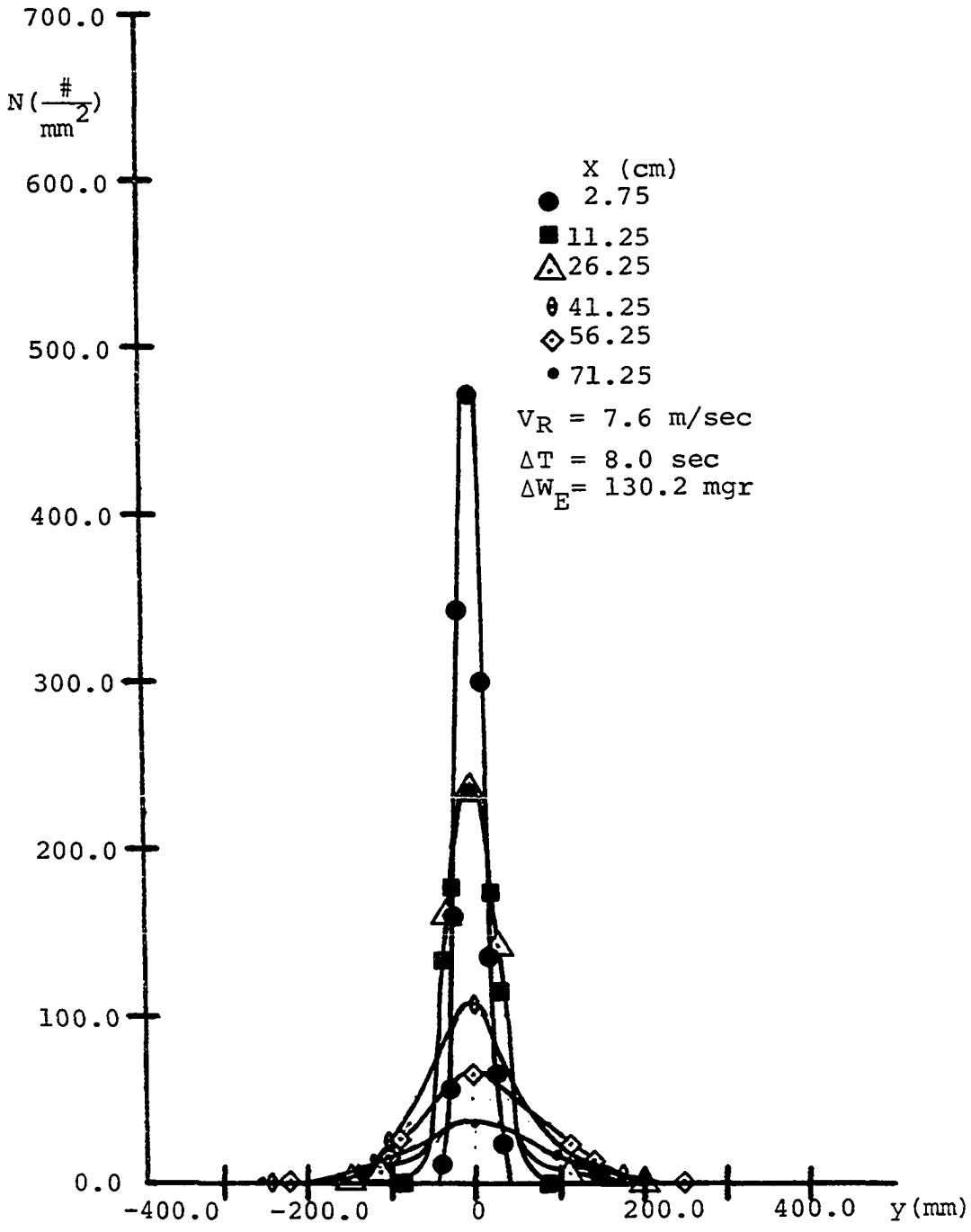

Figure A3a. N versus y (point source)

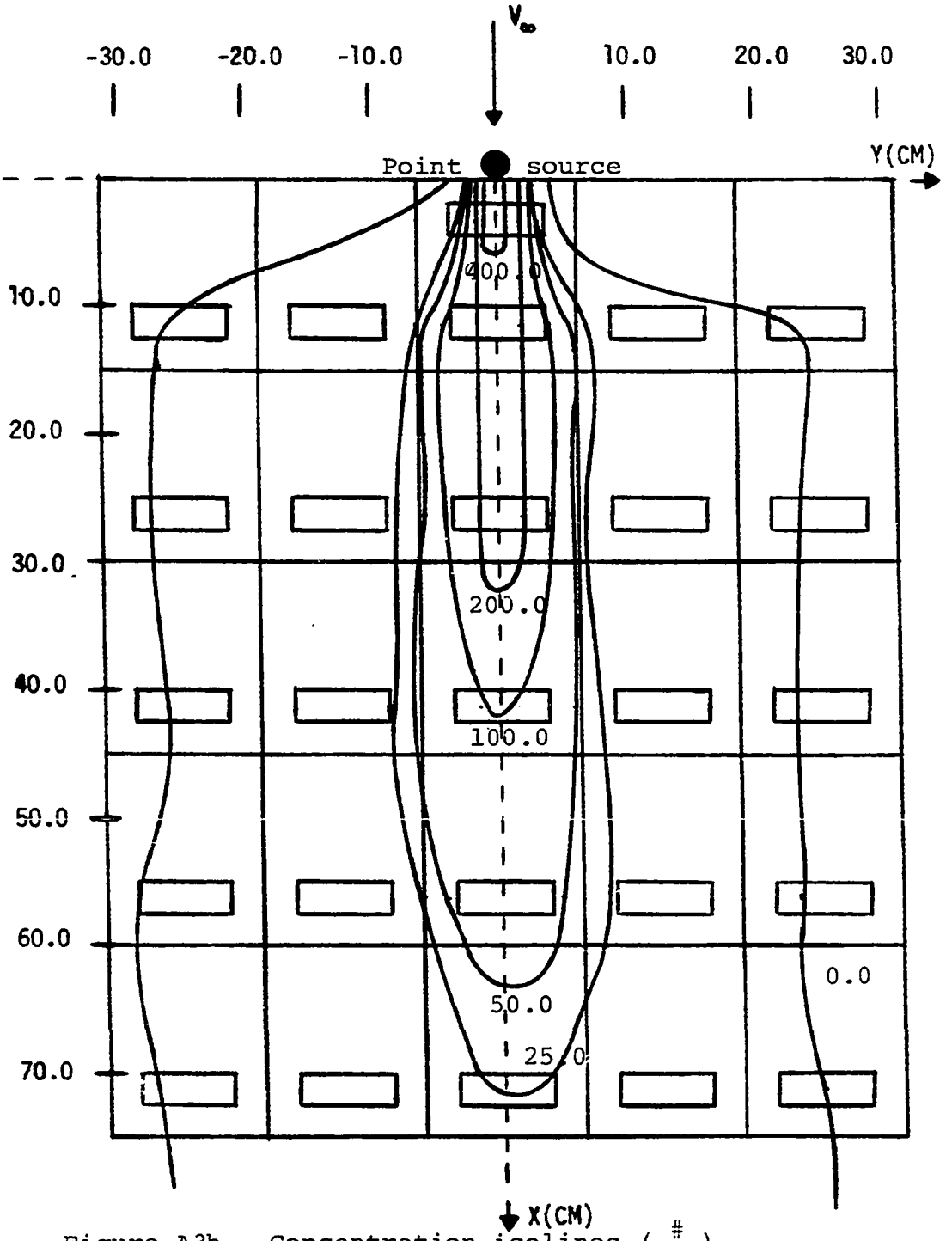

Figure A3b. Concentration isolines $\left(\frac{\#}{mm^2}\right)$

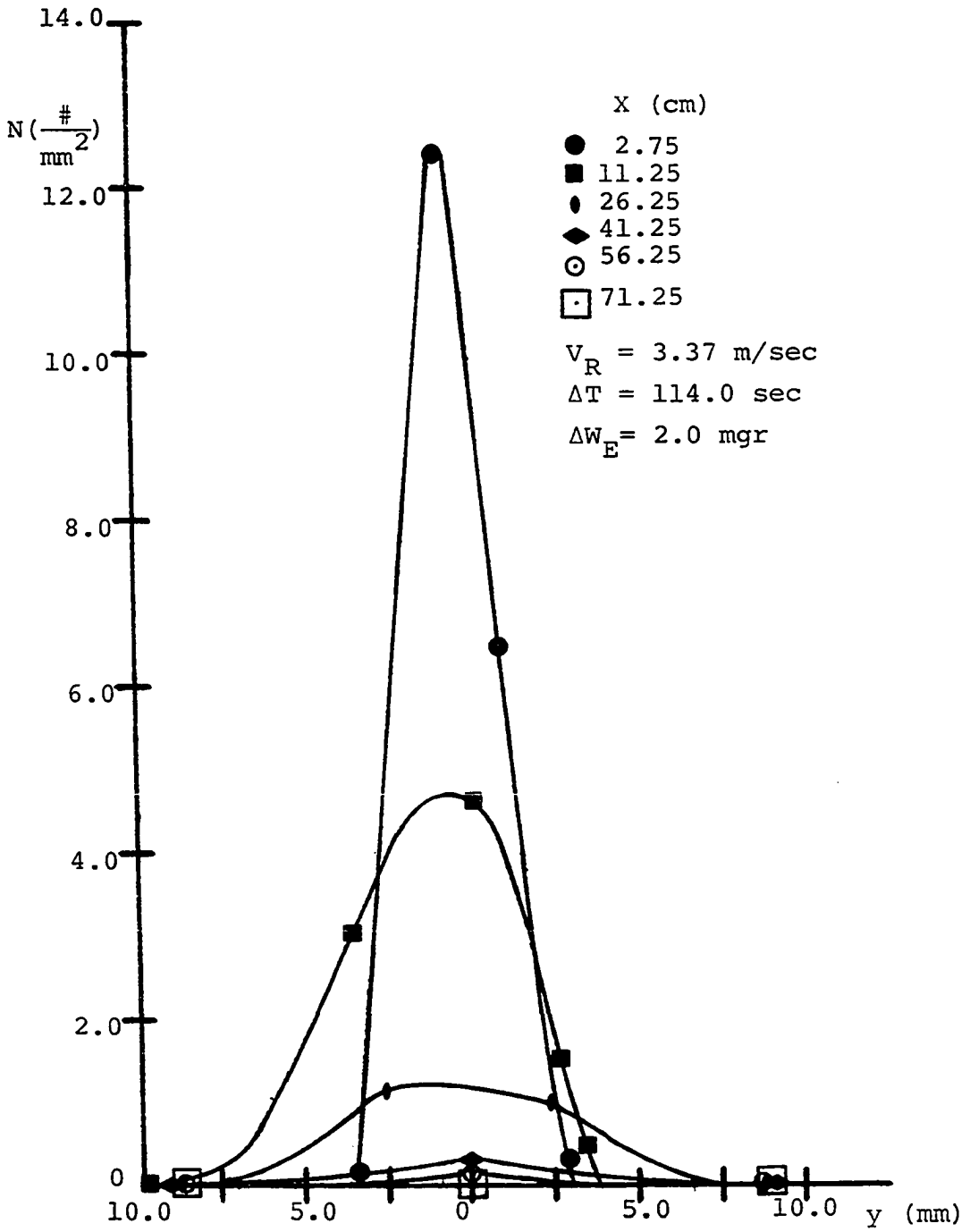

Figure A4a. N versus y (point source)

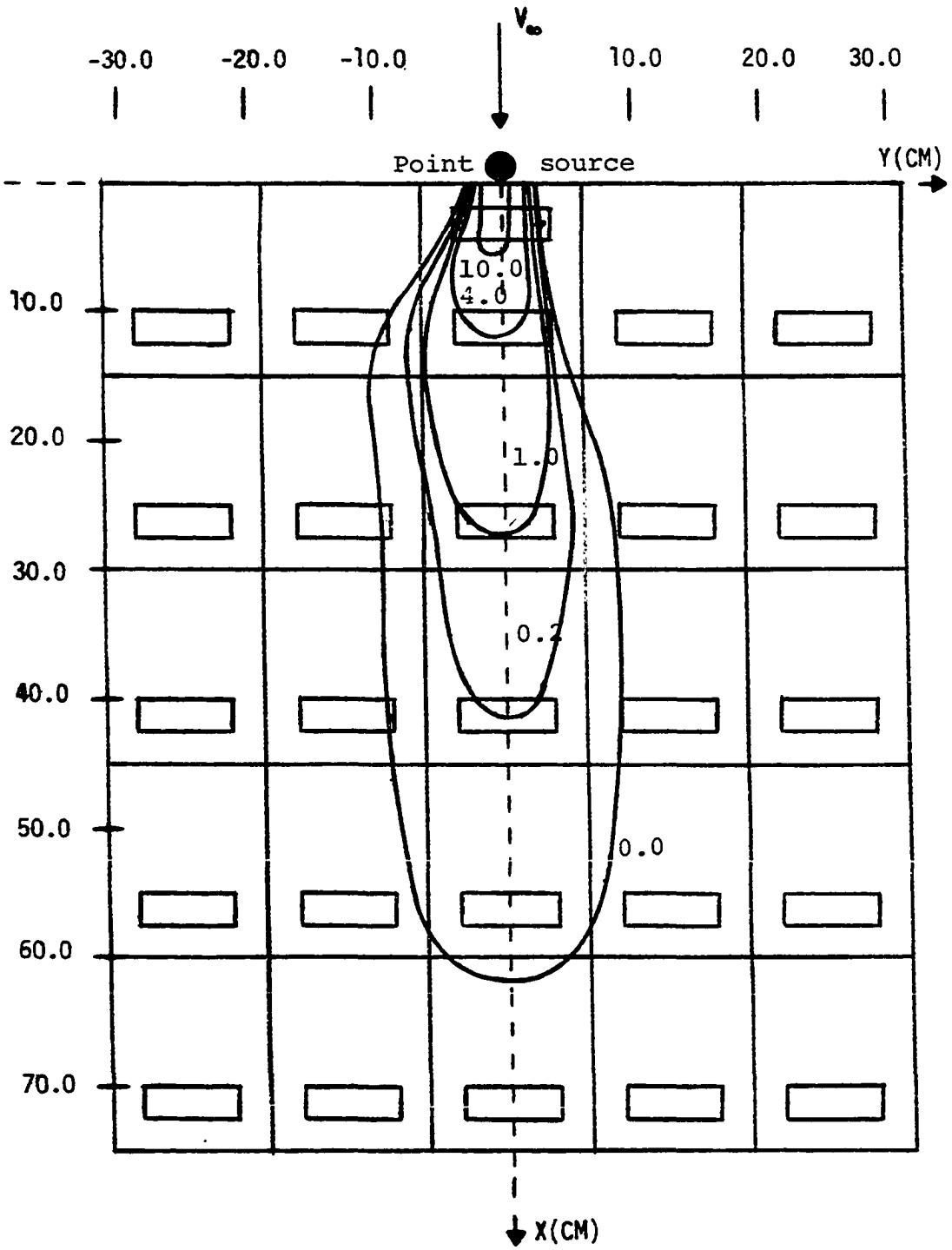

Figure A4b. Concentration isolines (#/mm^2)

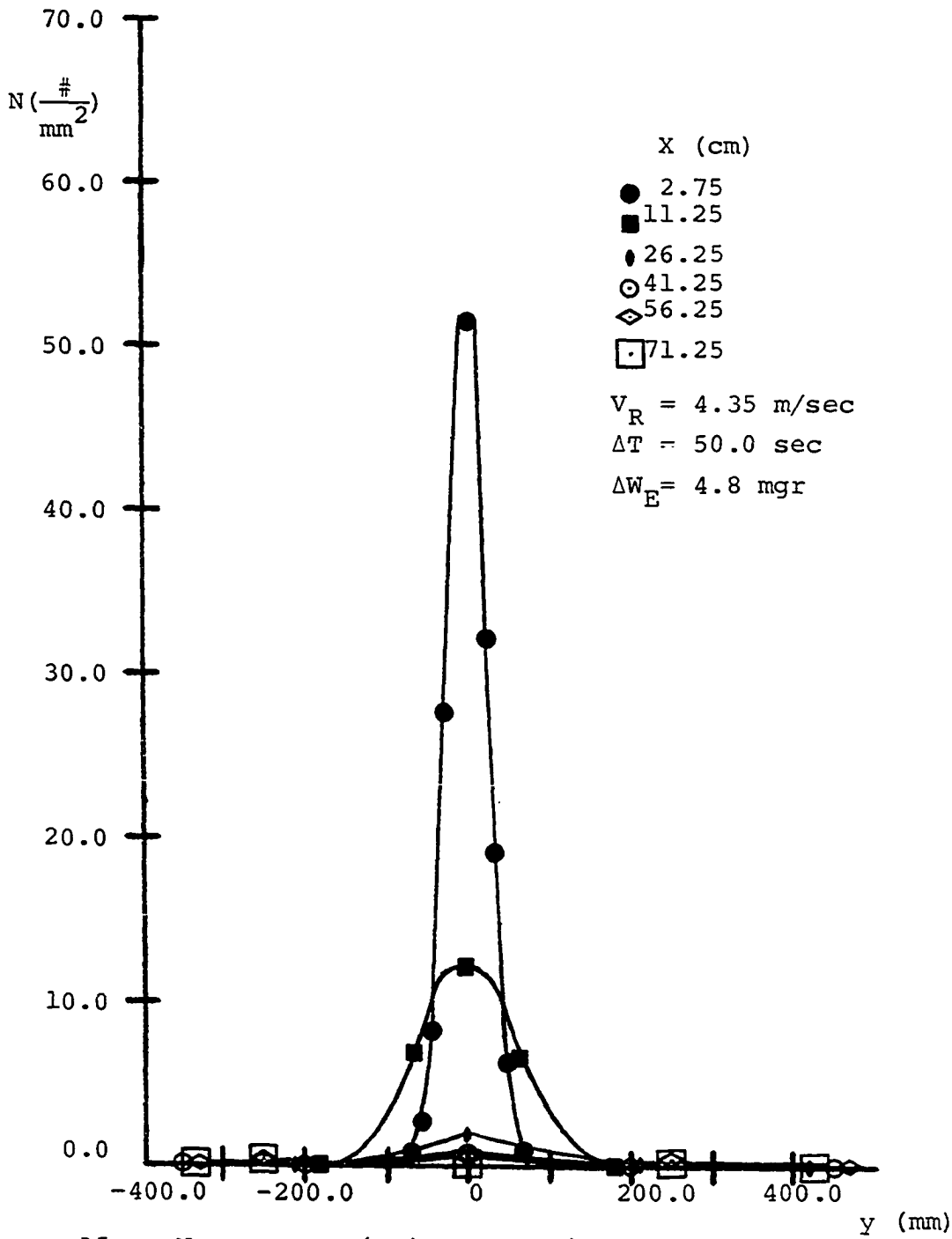

Figure A5a. N versus y (point source)

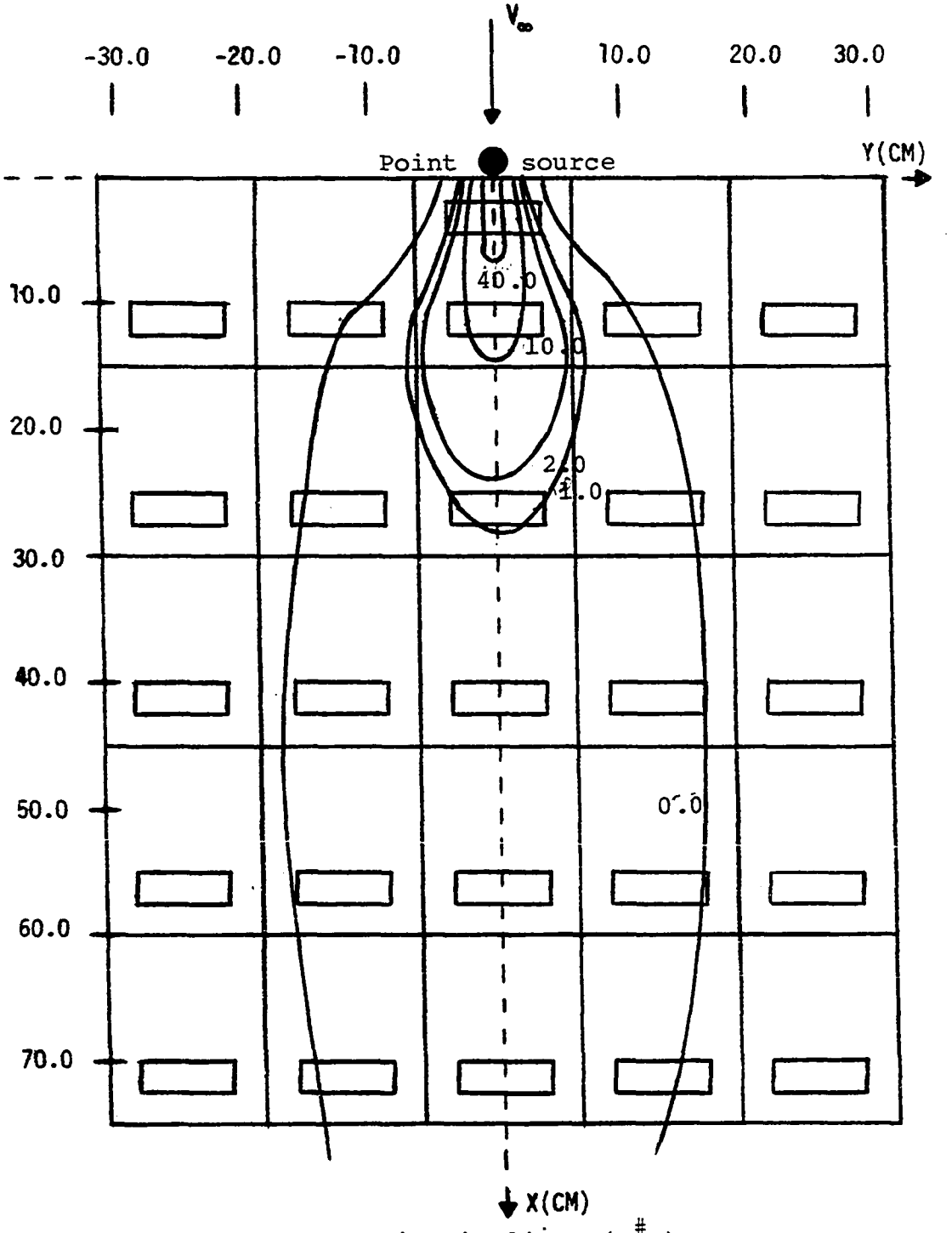

Figure A5b. Concentration isolines $(\frac{\#}{mm^2})$

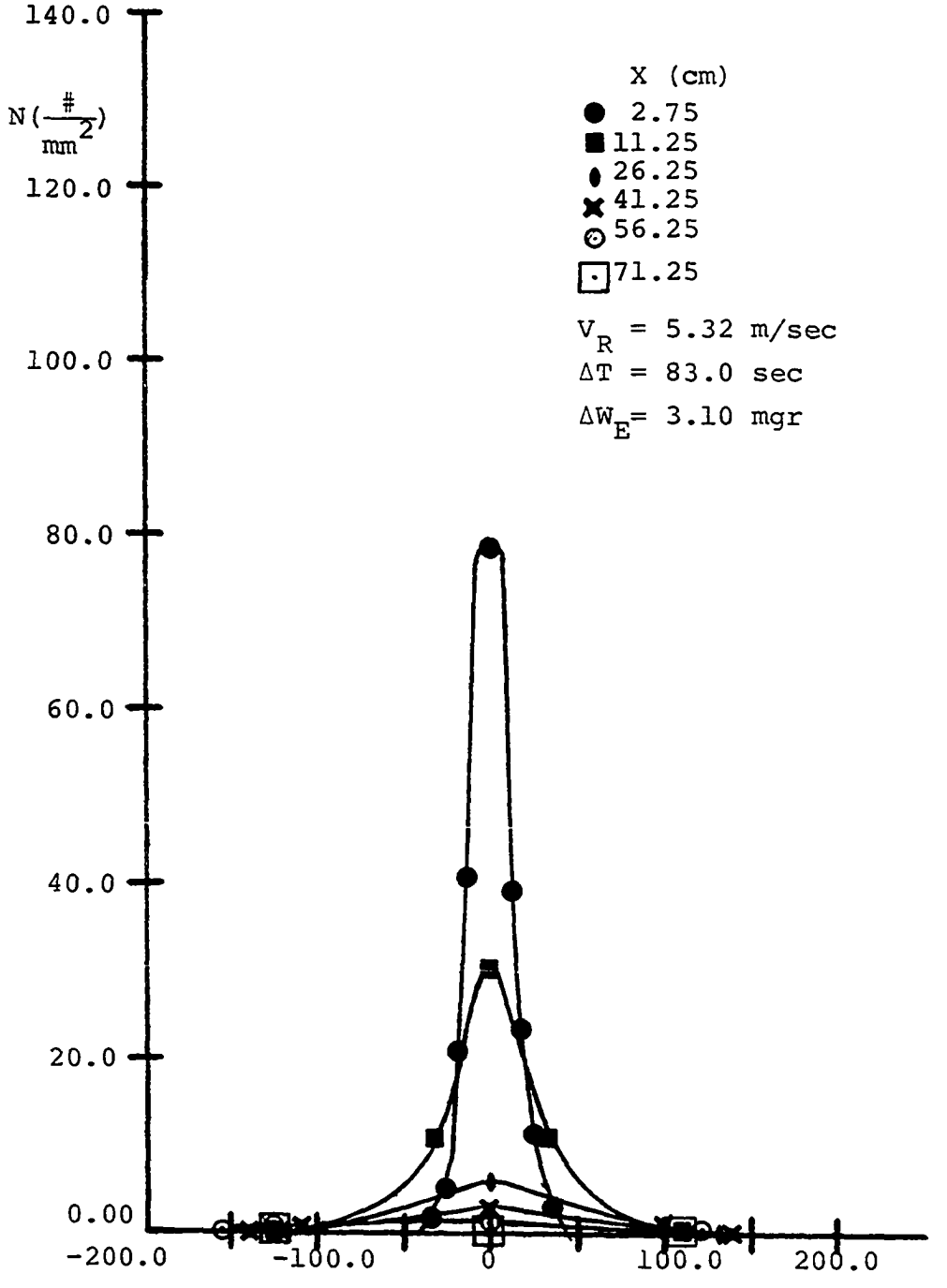

Figure A6a. N versus y (point source) y(mm)

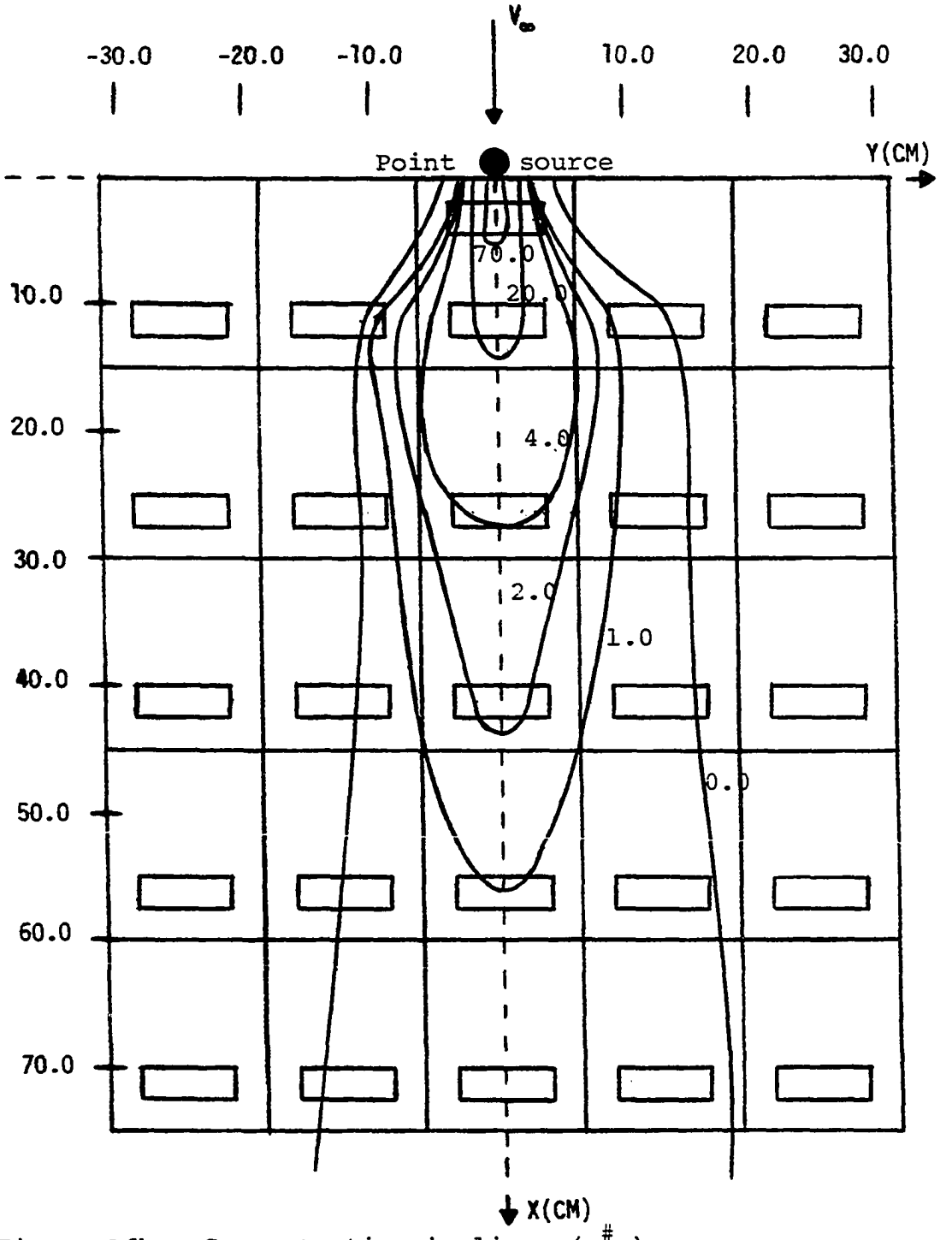

Figure A6b. Concentration isolines $(\frac{\#}{mm^2})$

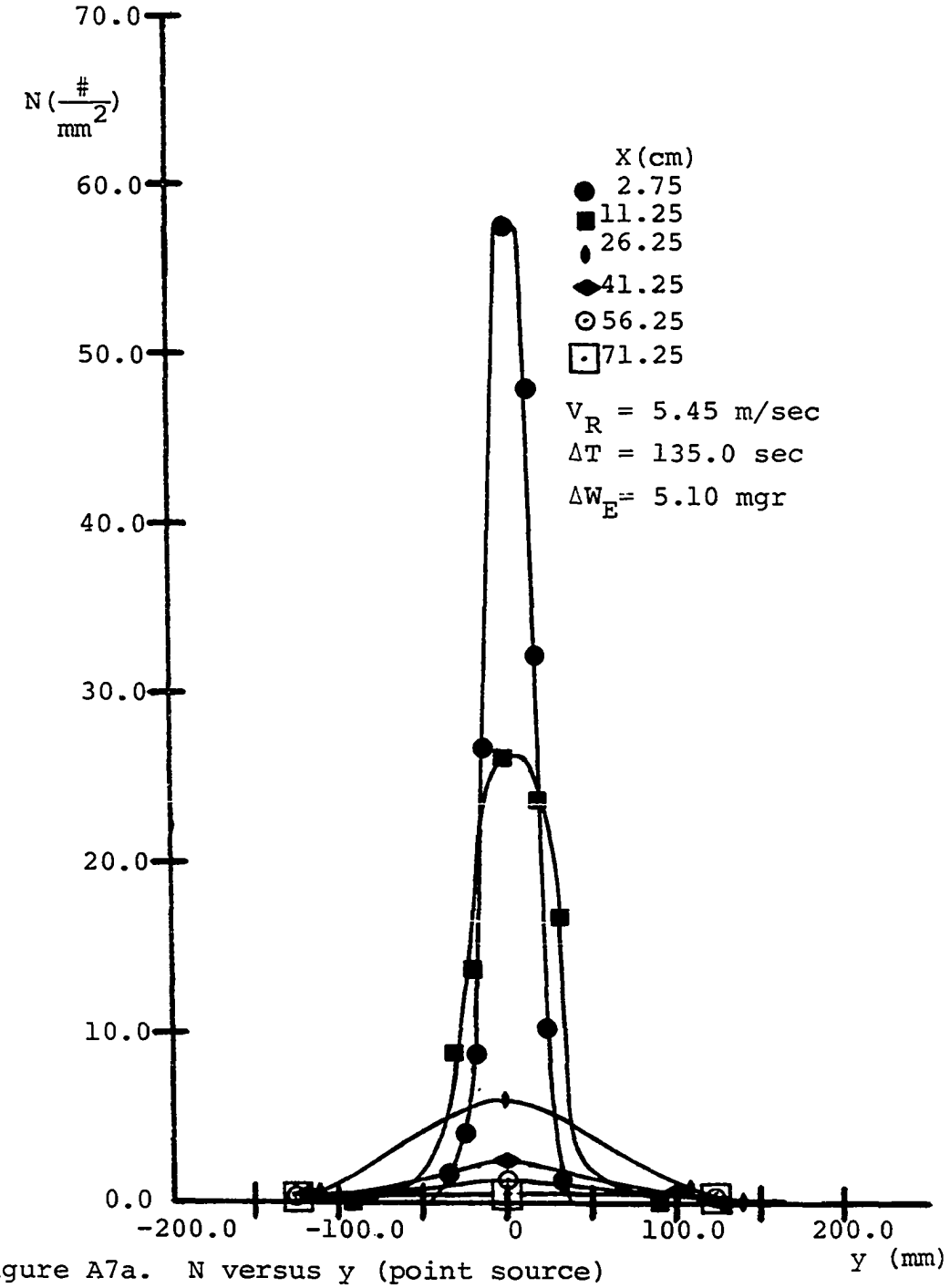

Figure A7a. N versus y (point source)

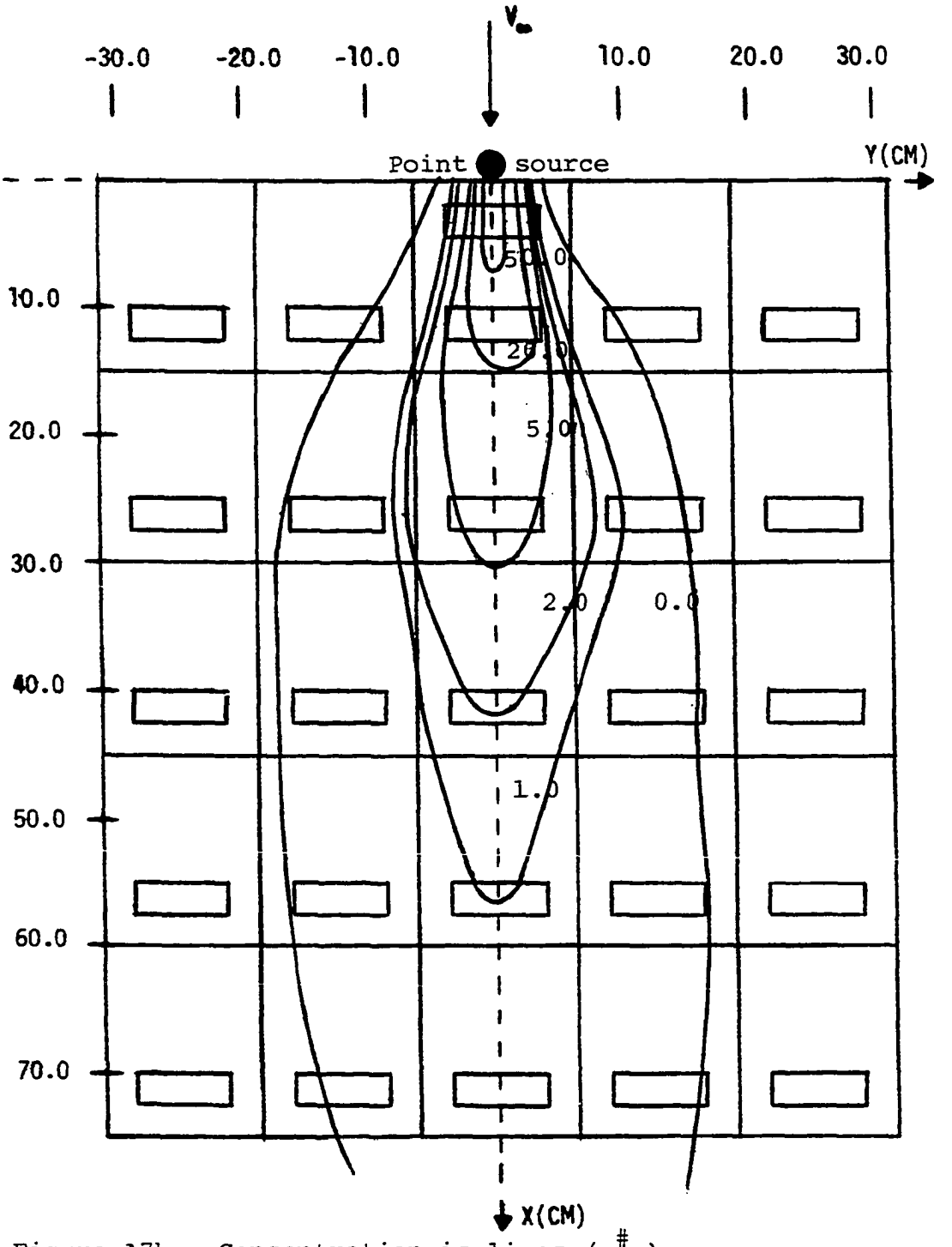

Figure A7b. Concentration isolines $(\frac{\#}{mm^2})$

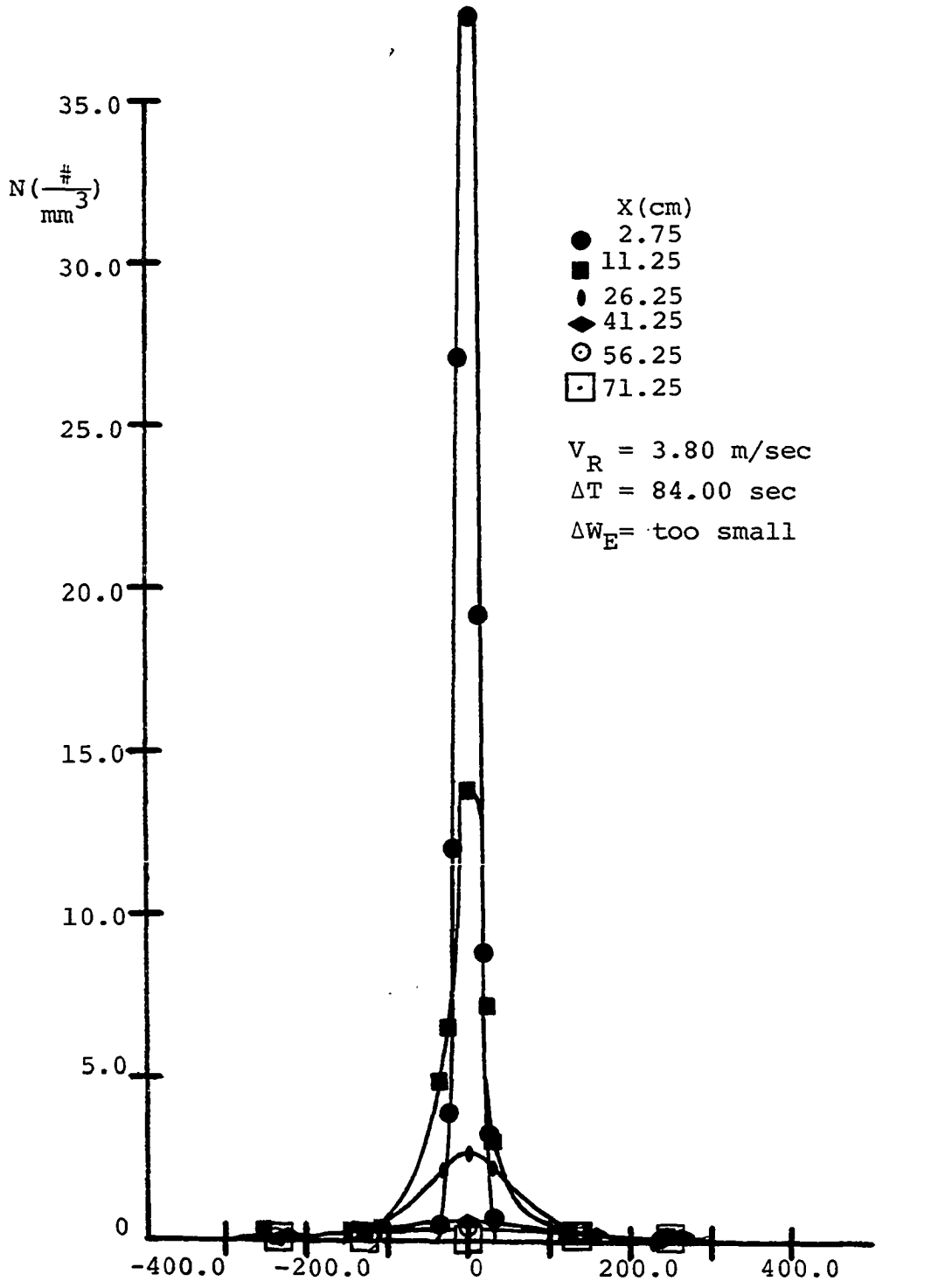

Figure A8a. N versus y (point source)

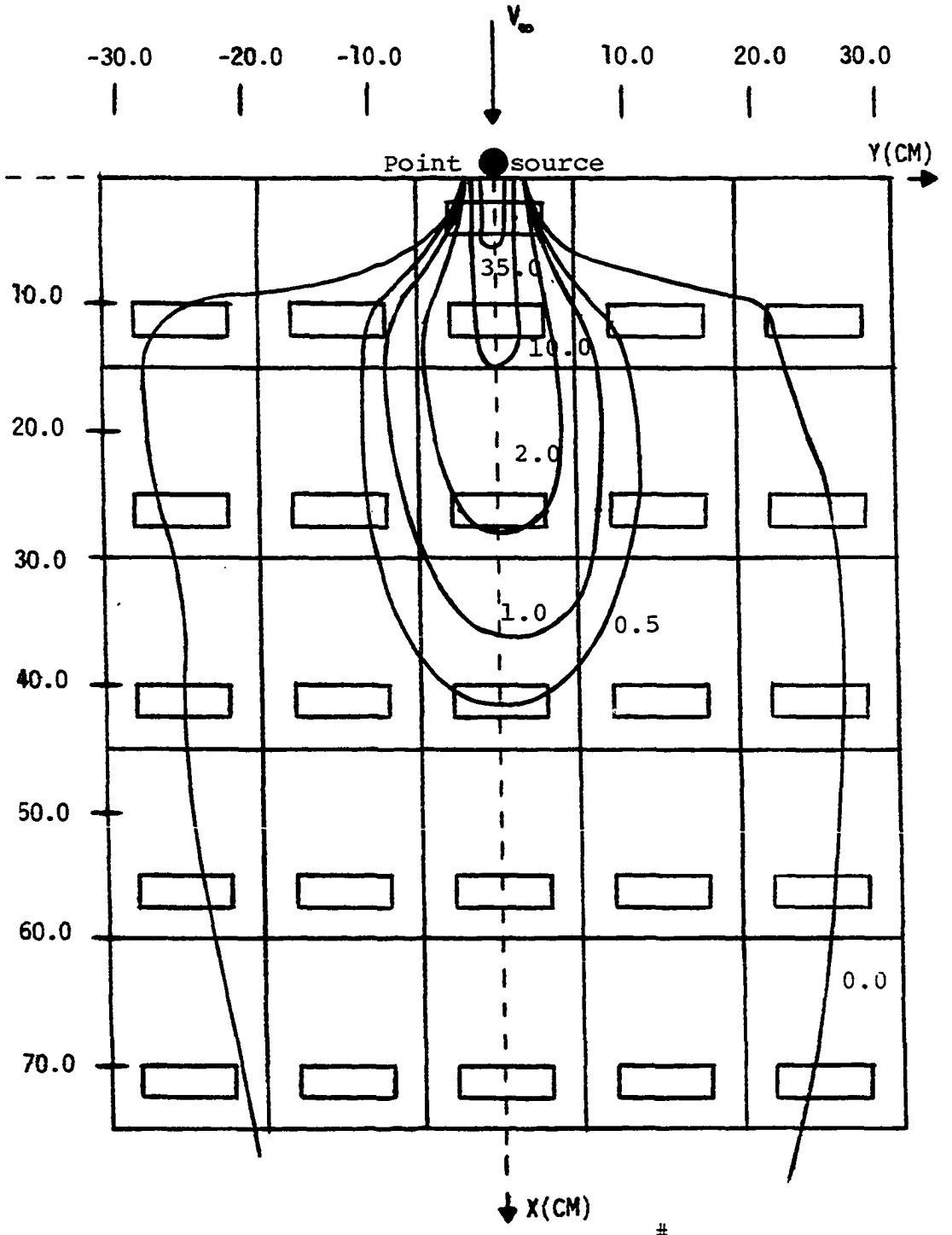

Figure A8b. Concentration isolines $(\frac{\#}{mm^2})$

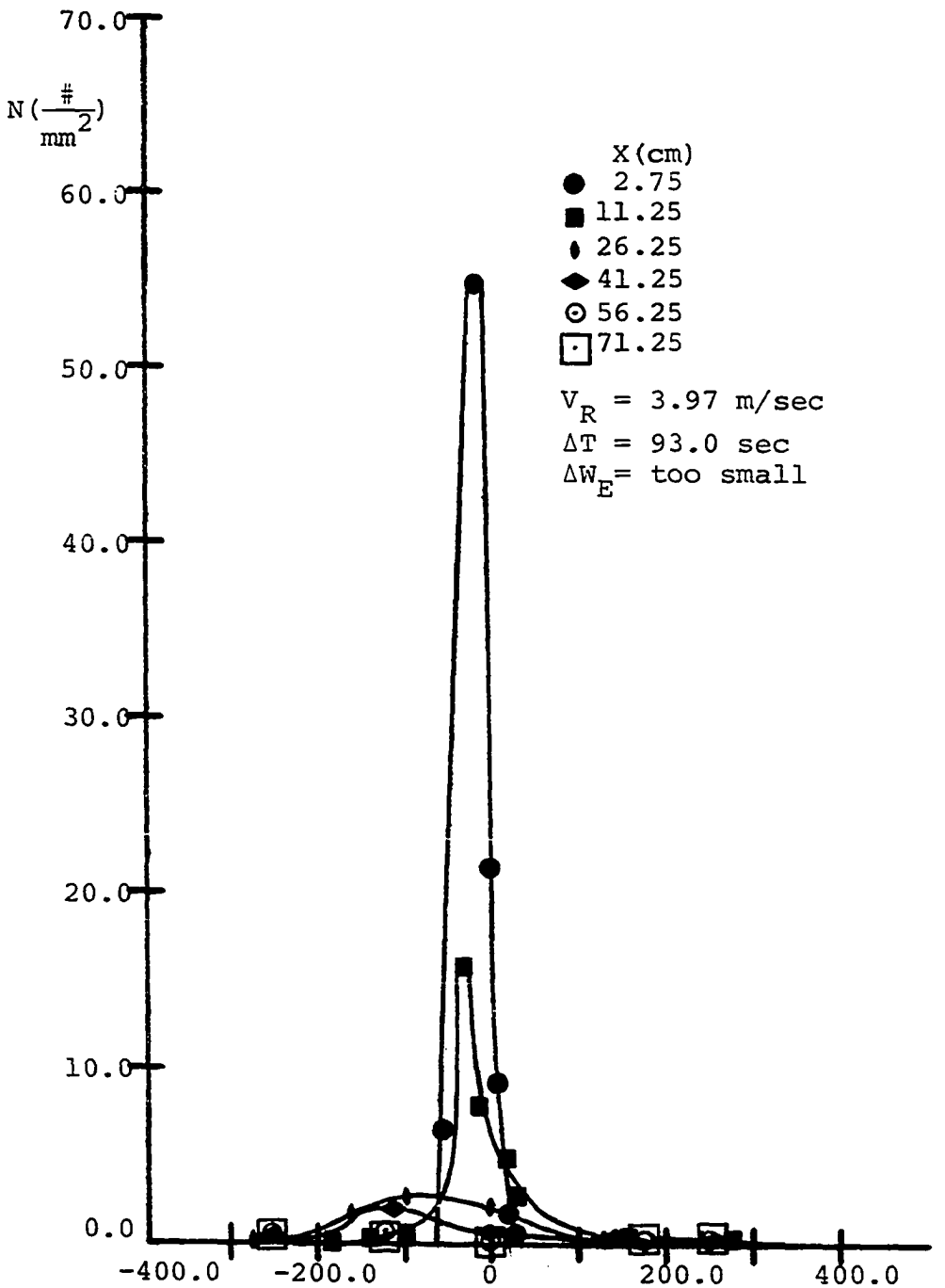

Figure A9a. N versus y (point source)

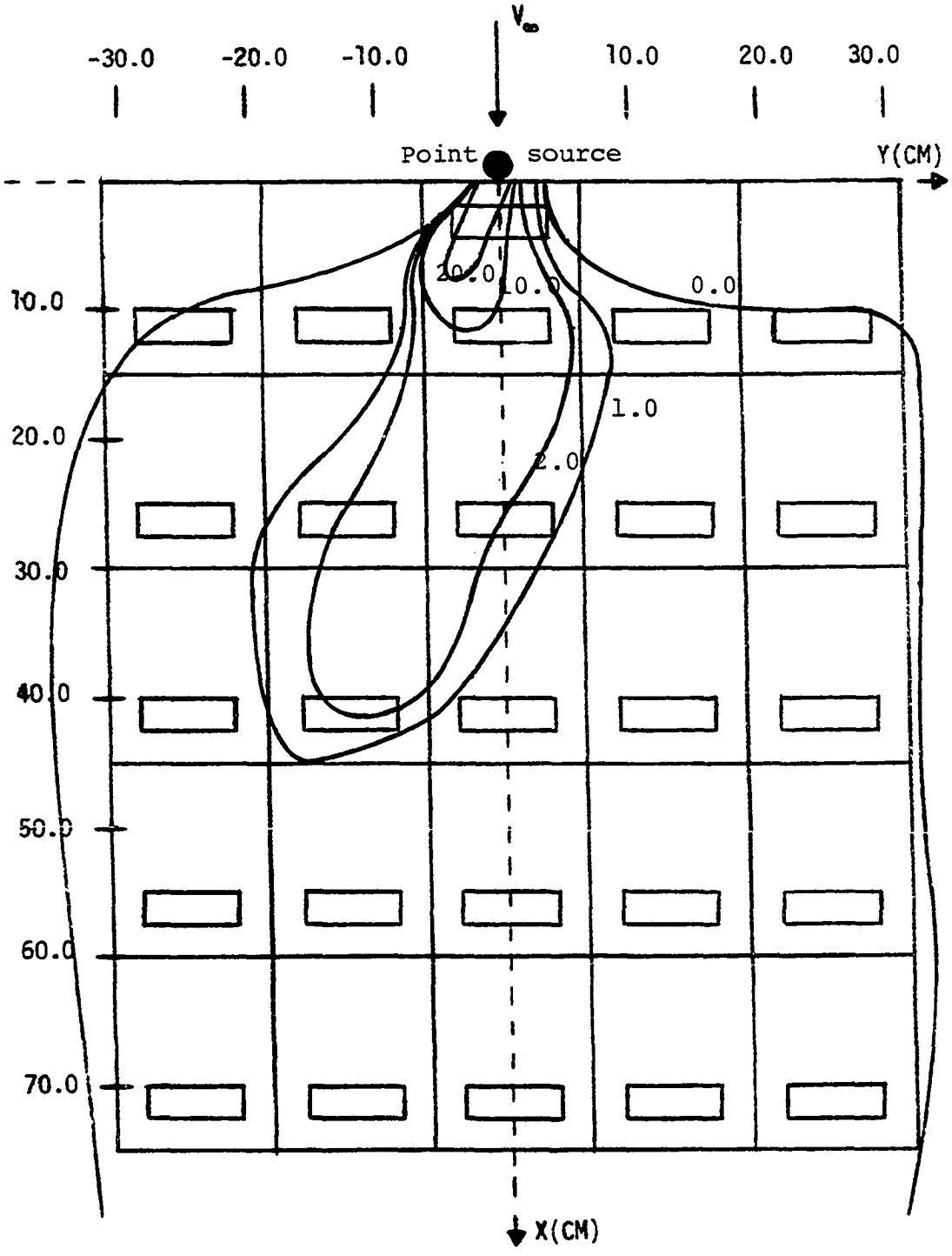

Figure A9b. Concentration isolines $(\frac{\#}{mm^2})$

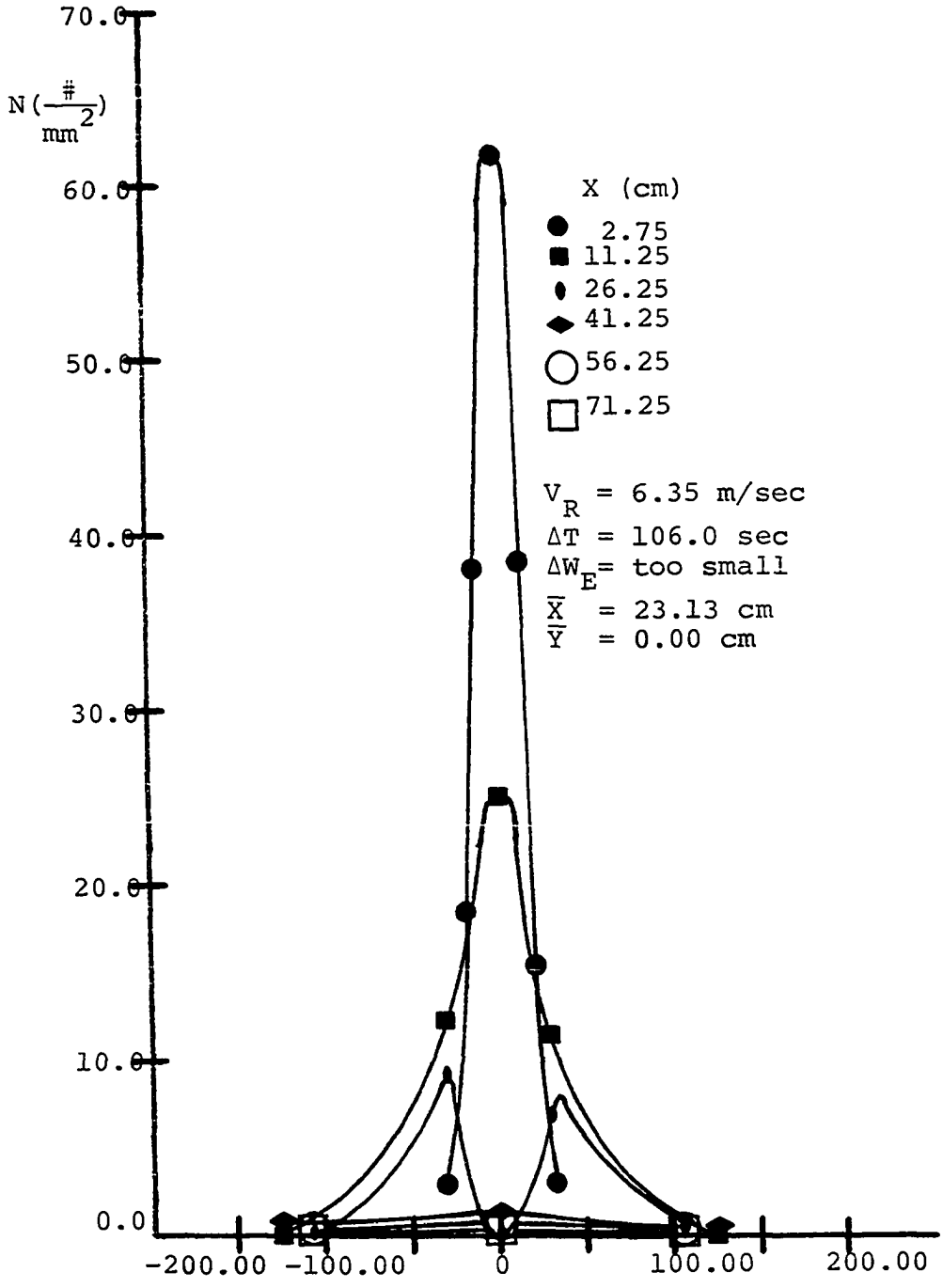

Figure A10a. N versus y (point source with three-dimensional obstacle)

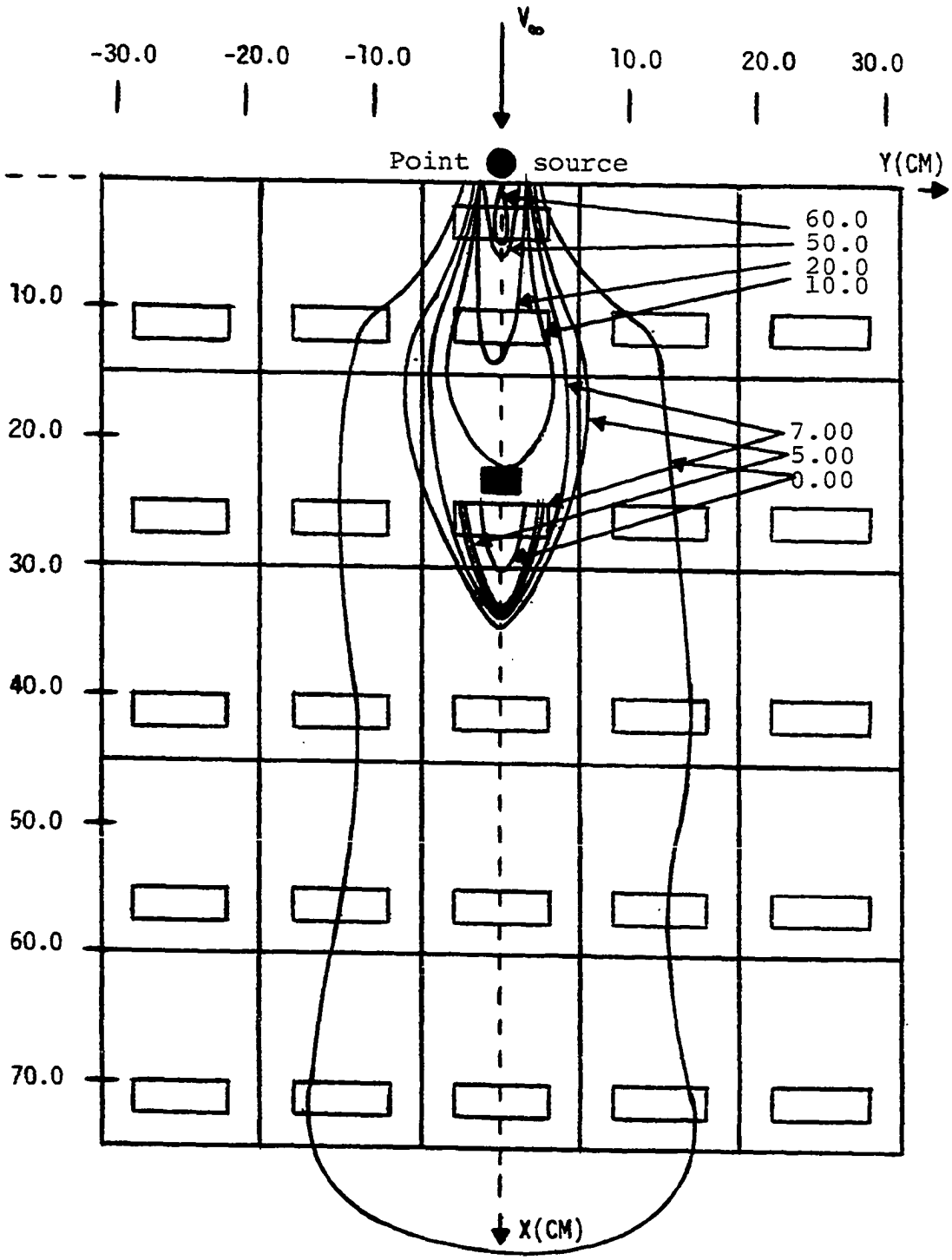

Figure A10b. Concentration isolines $(\frac{\#}{mm^2})$

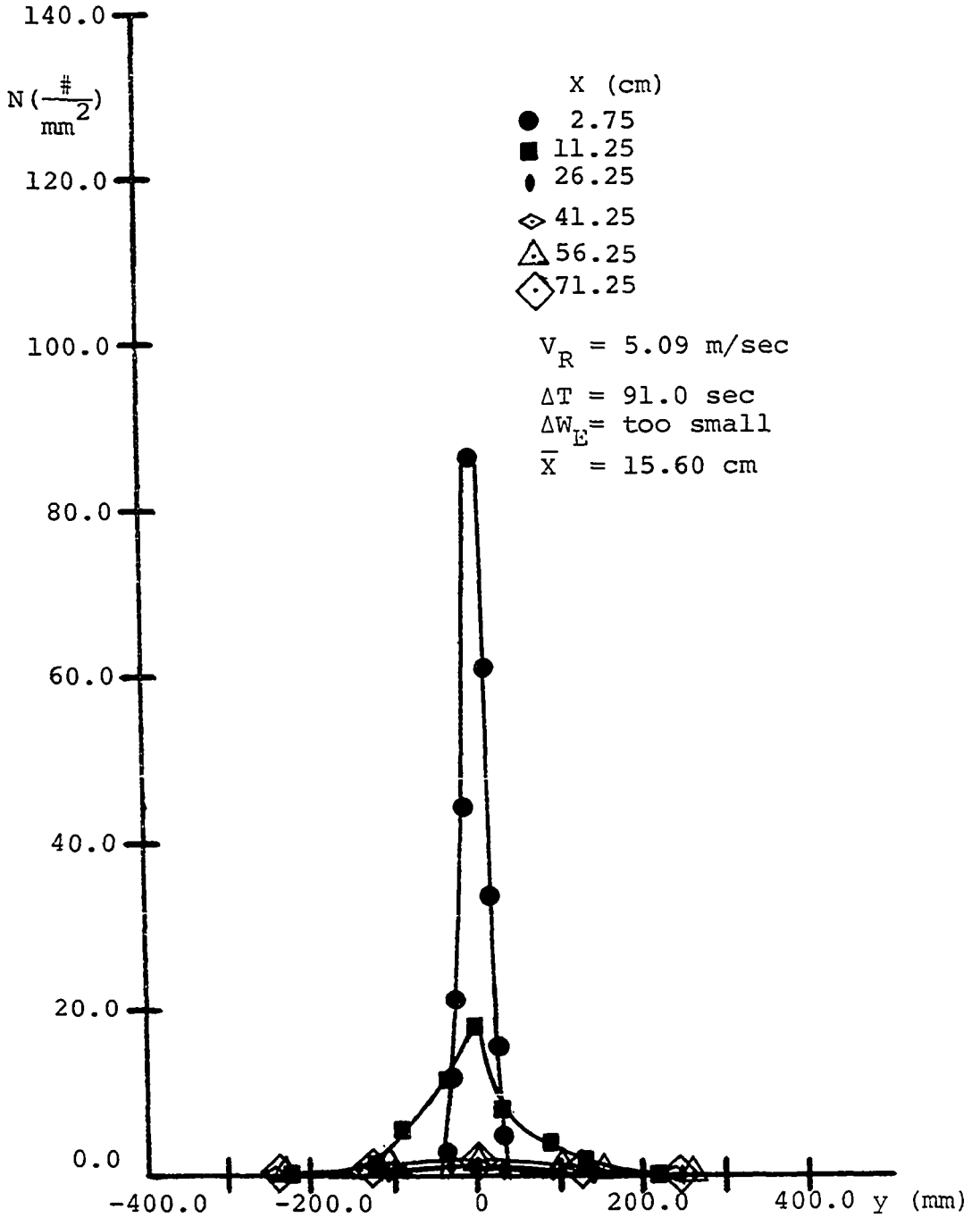

Figure A11a. N versus y (point source with two-dimensional obstacle)

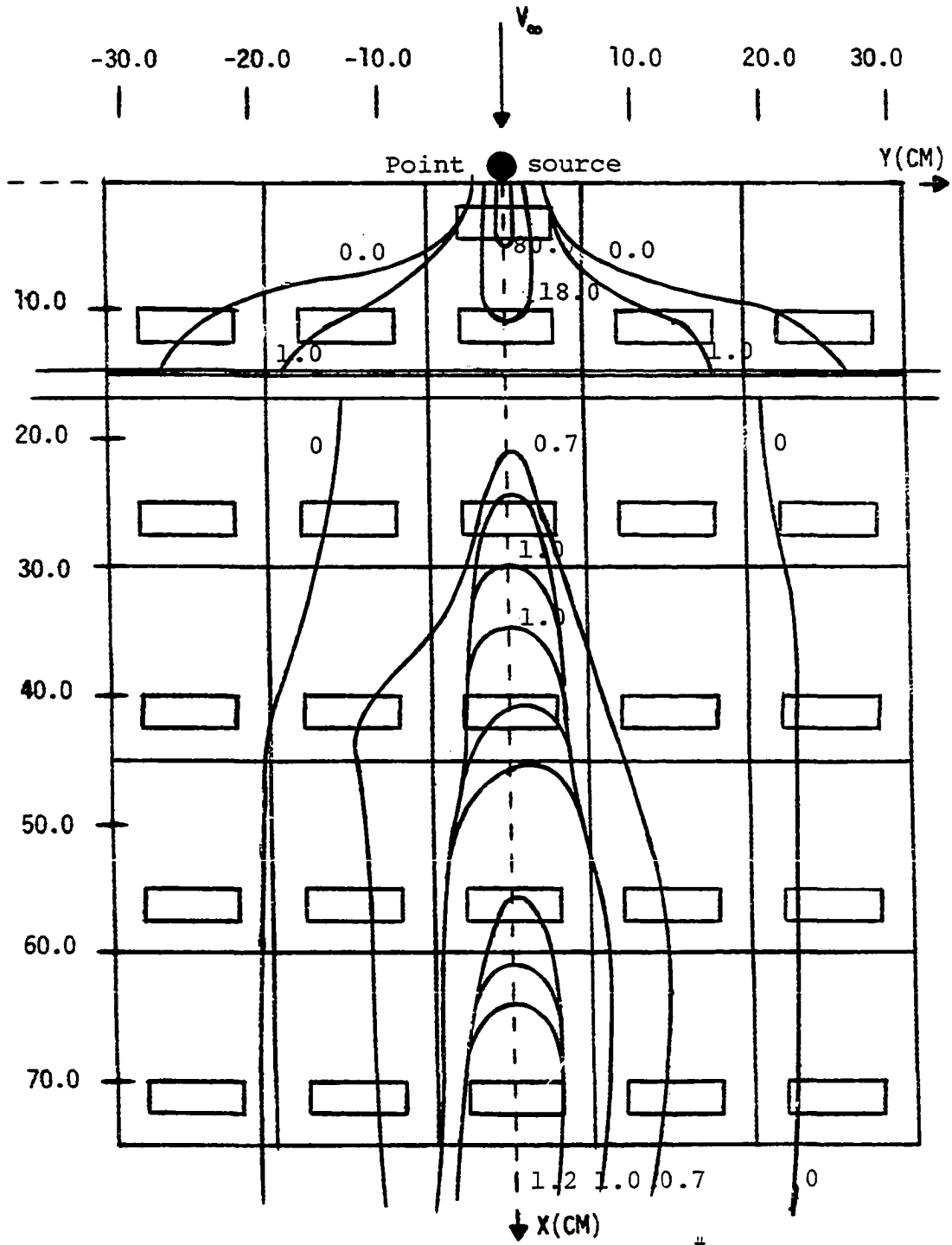

Figure A11b. Concentration isolines $(\frac{\#}{mm^2})$

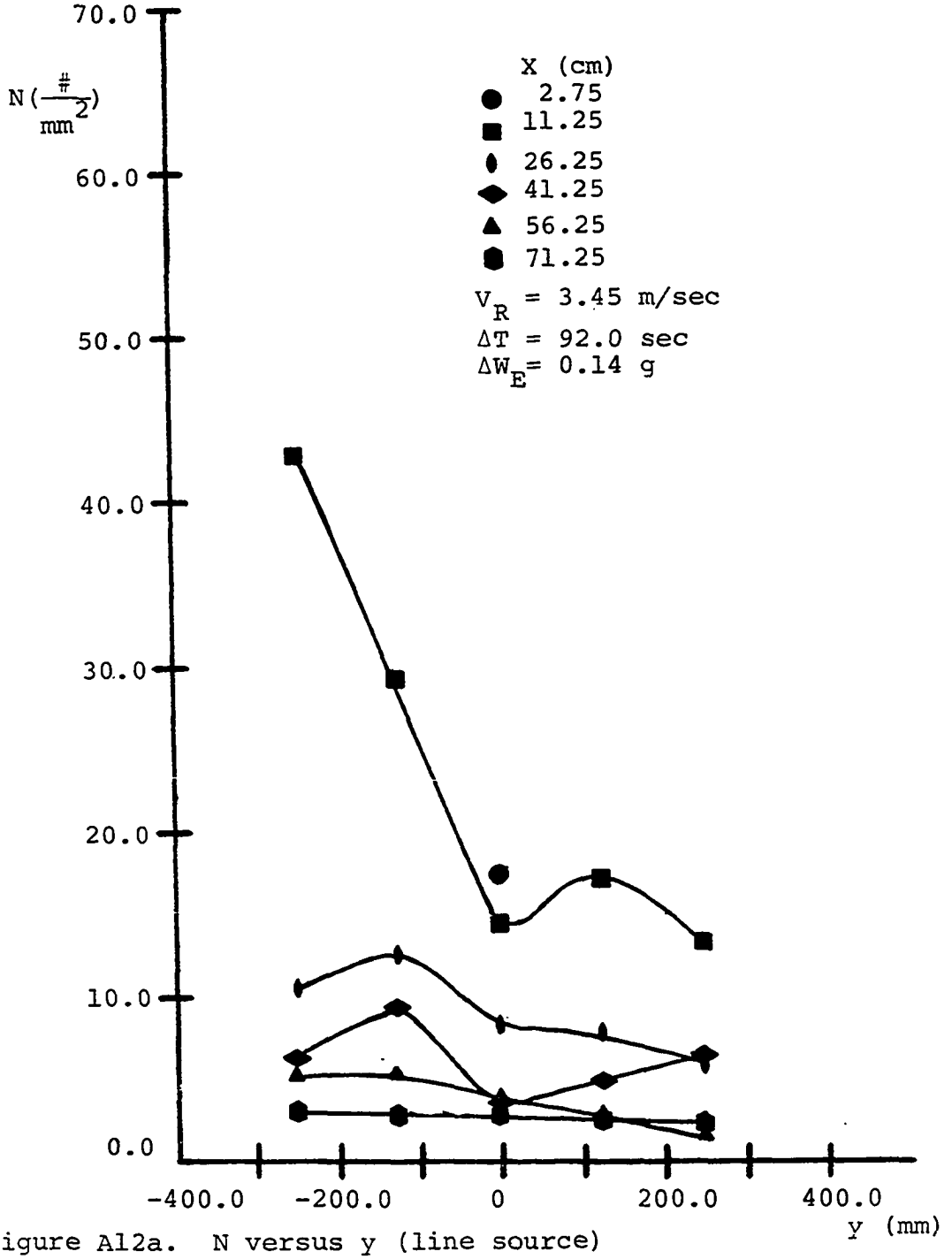

Figure A12a. N versus y (line source)

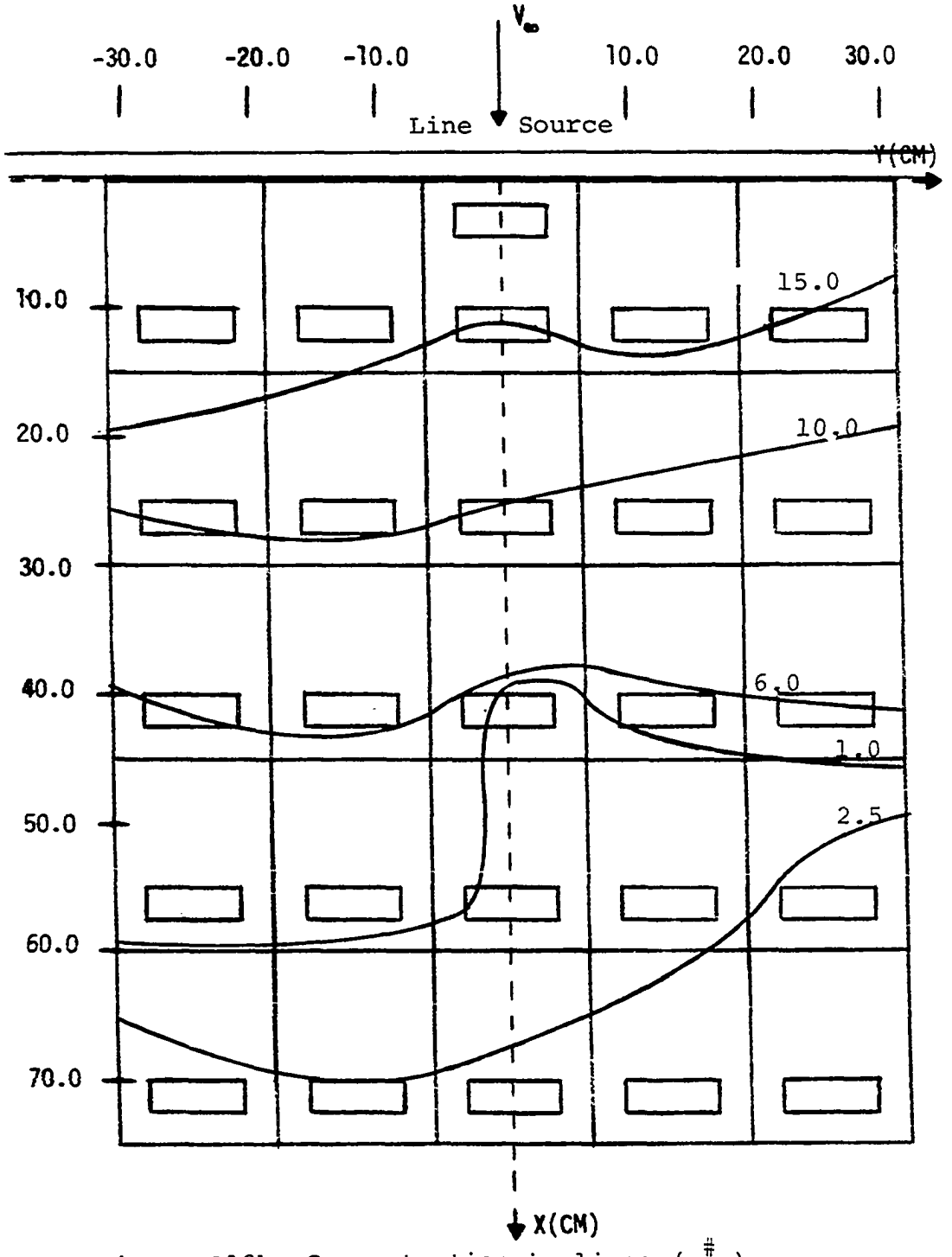

Figure A12b. Concentration isolines $(\frac{\#}{mm^2})$

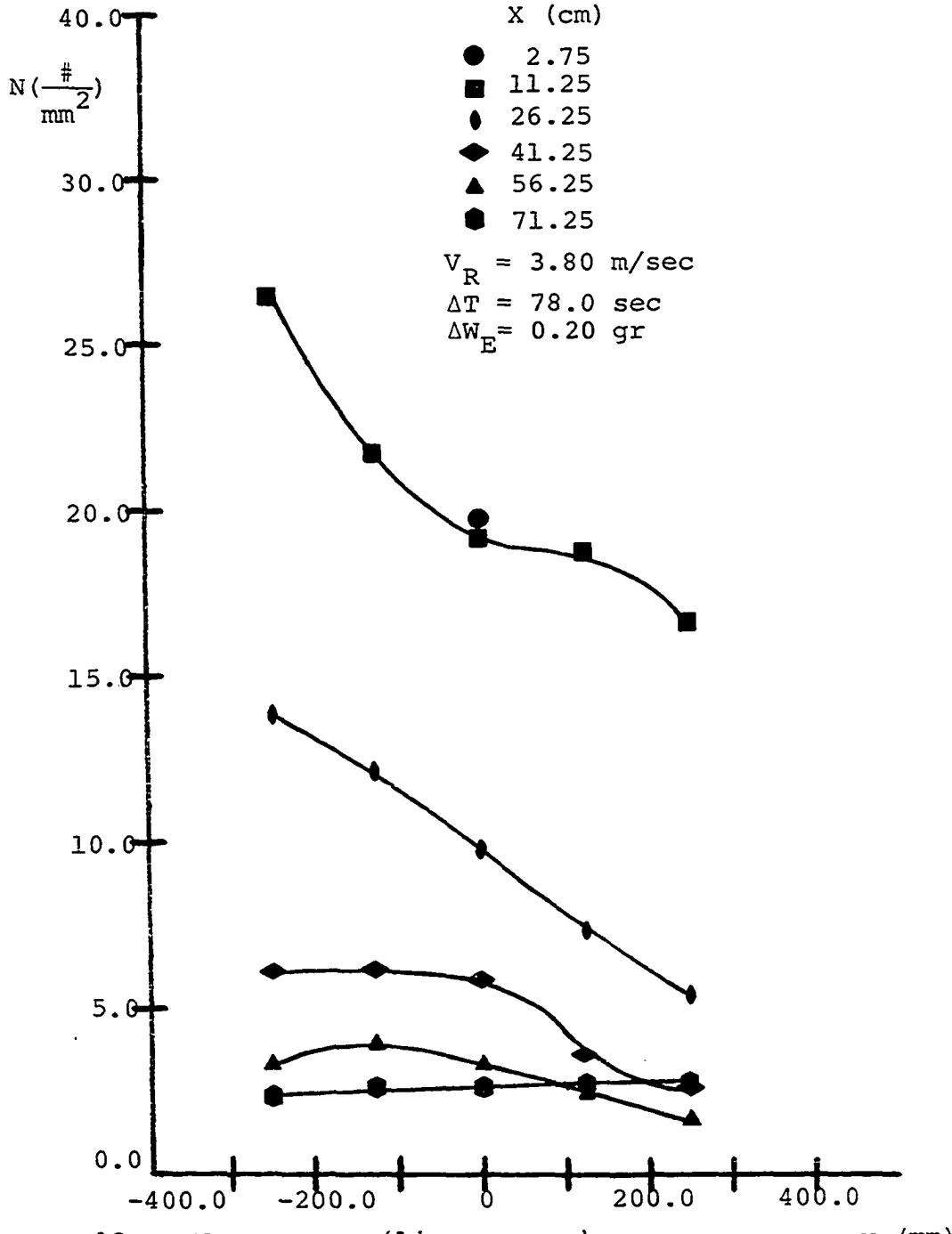

Figure A13a. N versus y (line source)

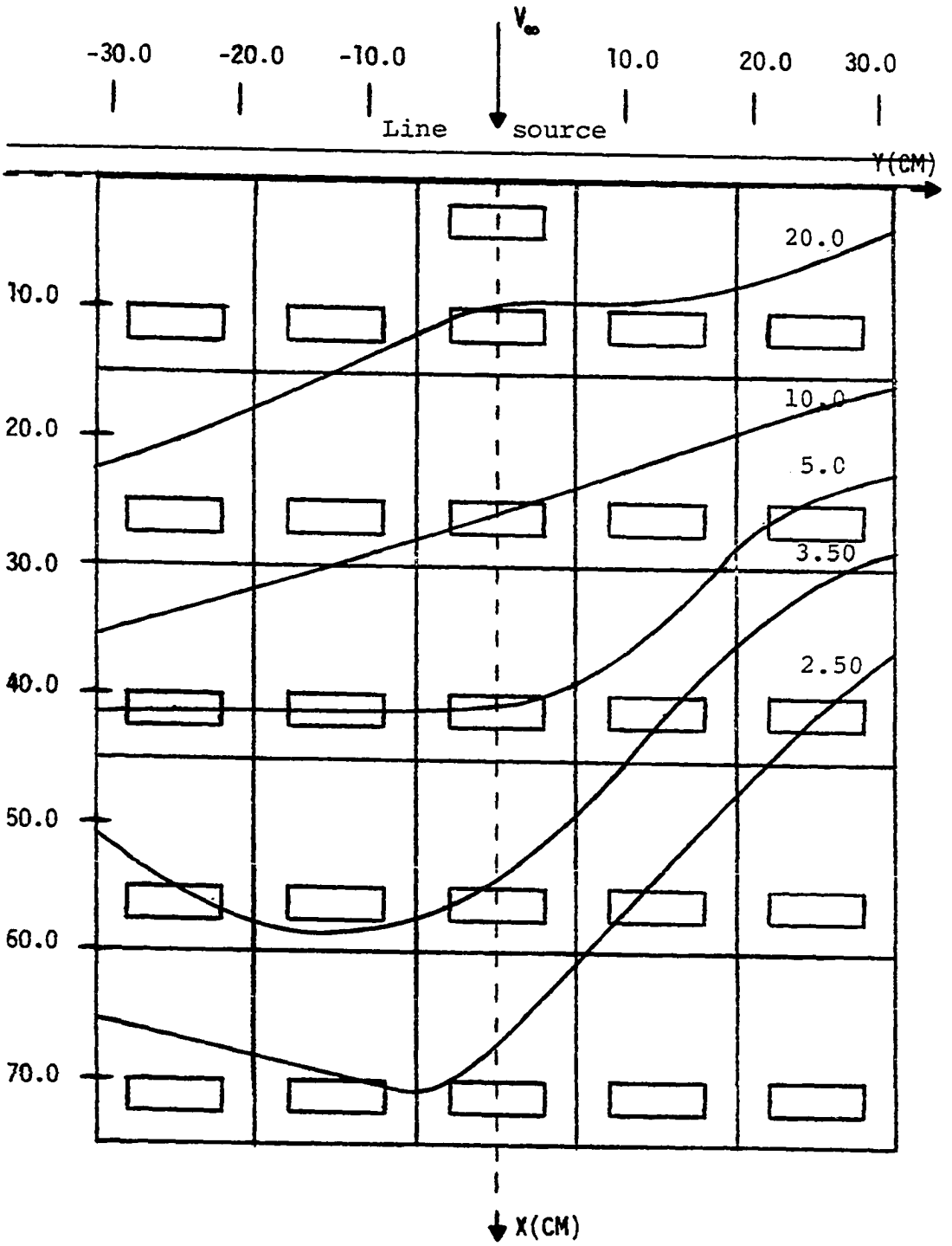

Figure A13b. Concentration isolines $(\frac{\#}{mm^2})$

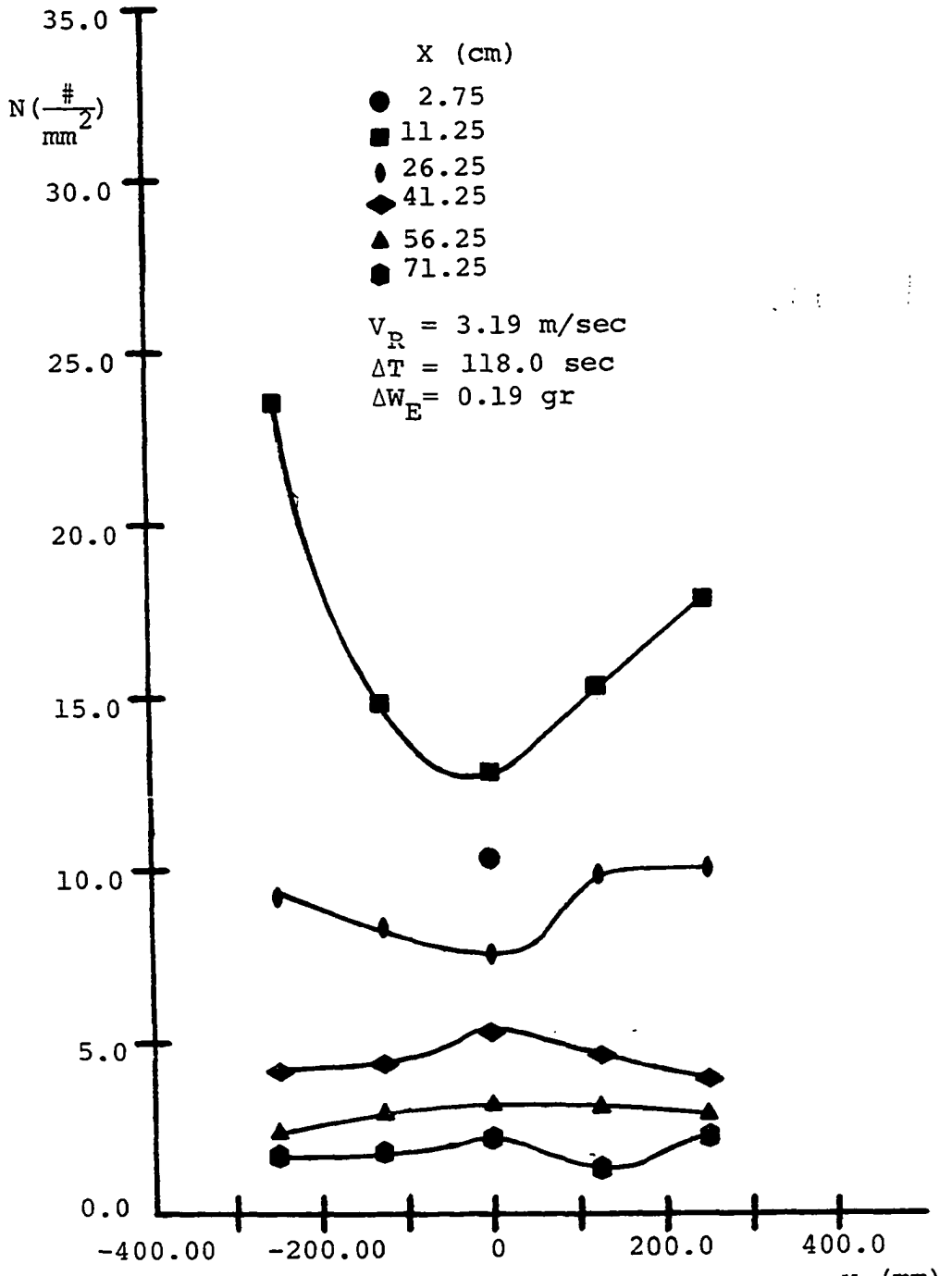

Figure A14a. N versus y (line source)

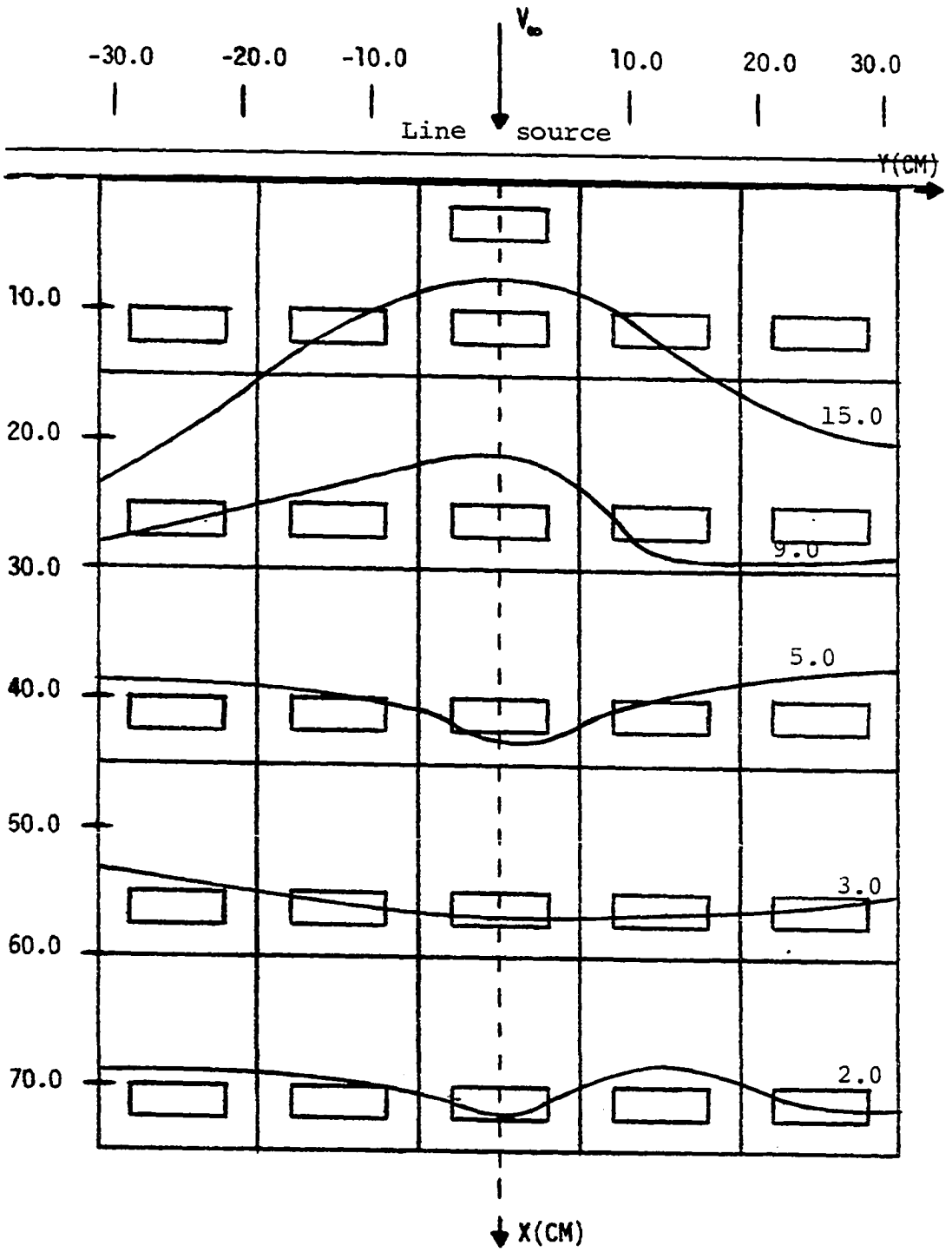

Figure A14b. Concentration isolines $(\frac{\#}{mm^2})$

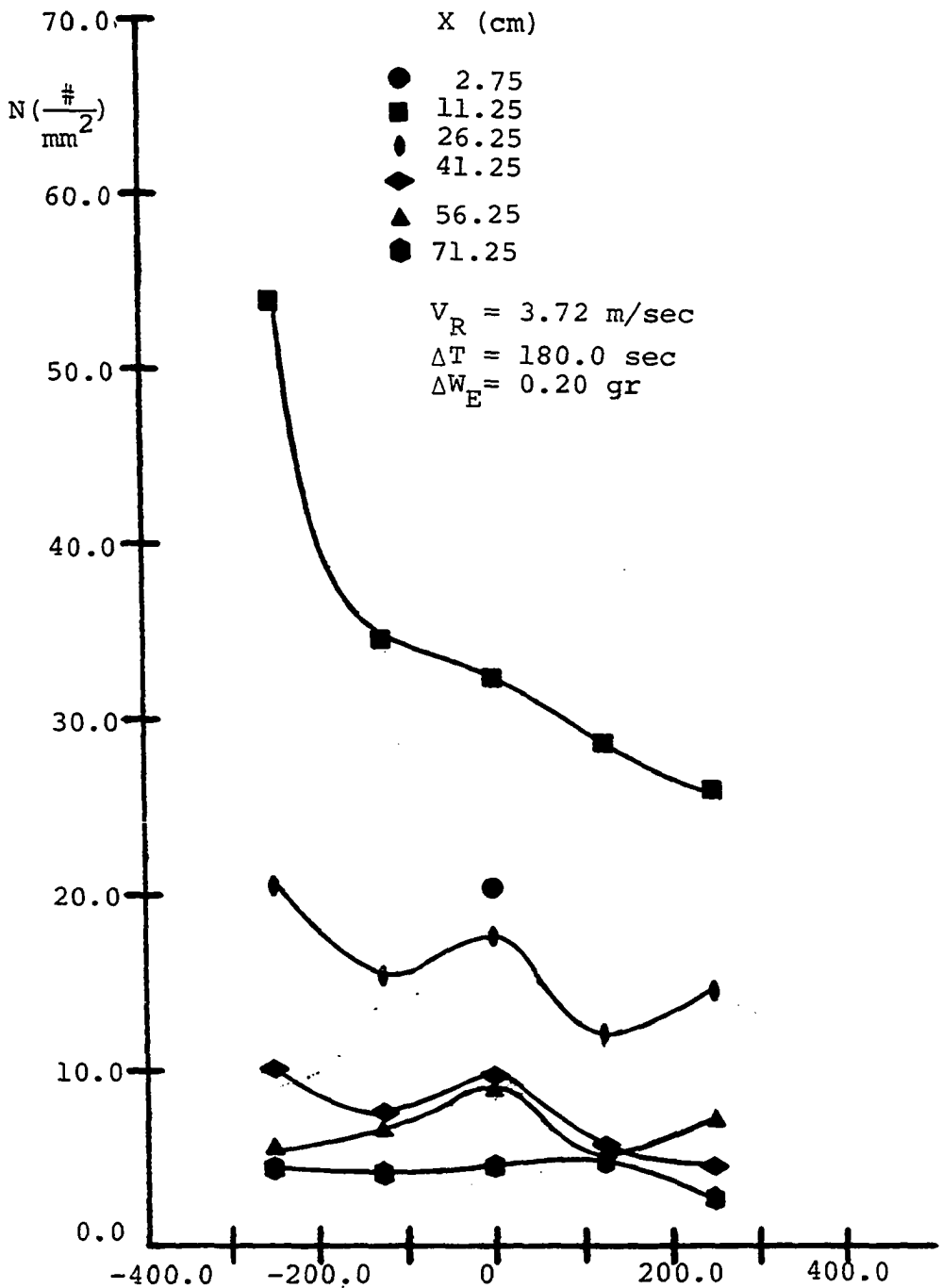

Figure A15a. N versus y (line source)

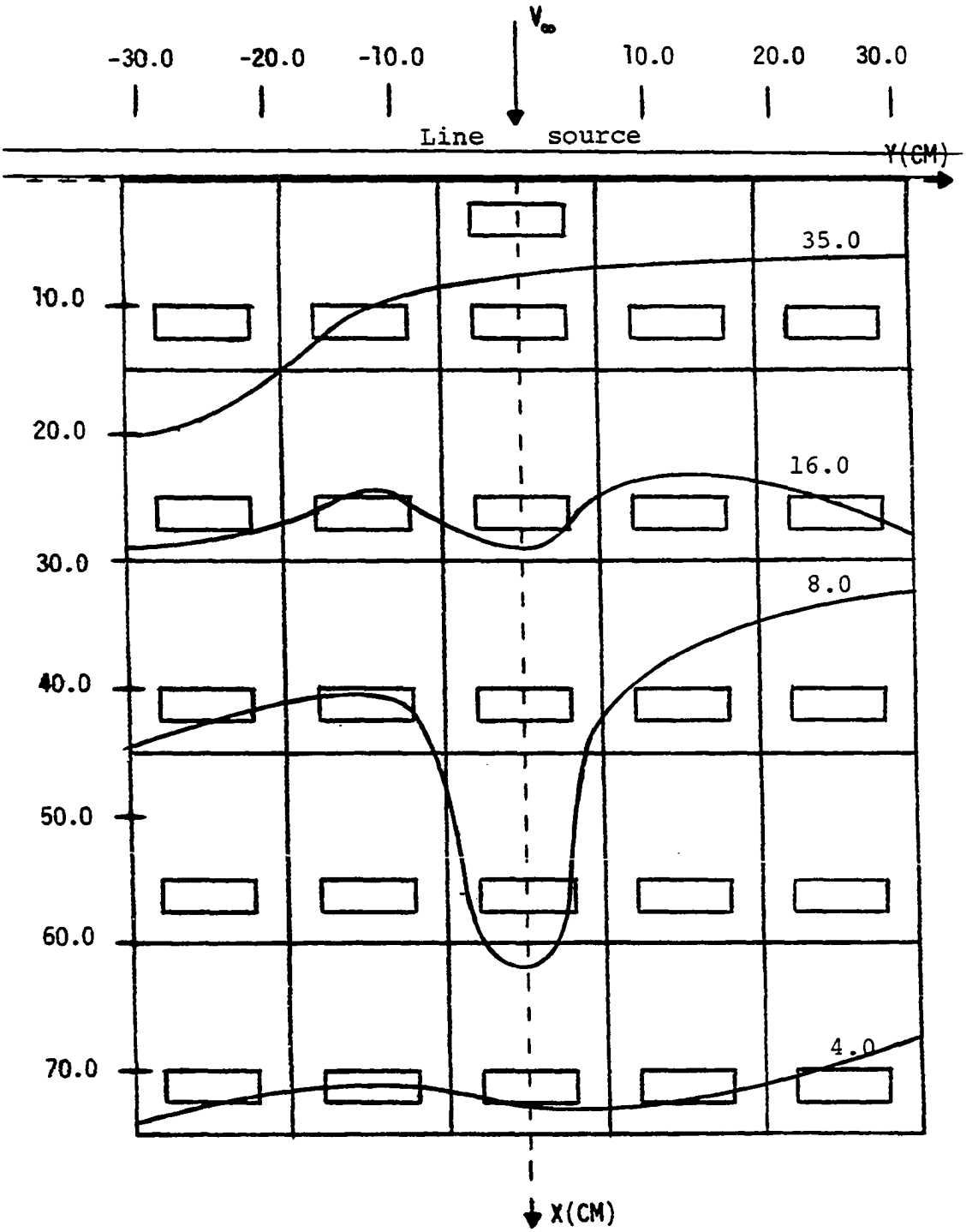

Figure A15b. Concentration isolines $(\frac{\#}{mm^2})$

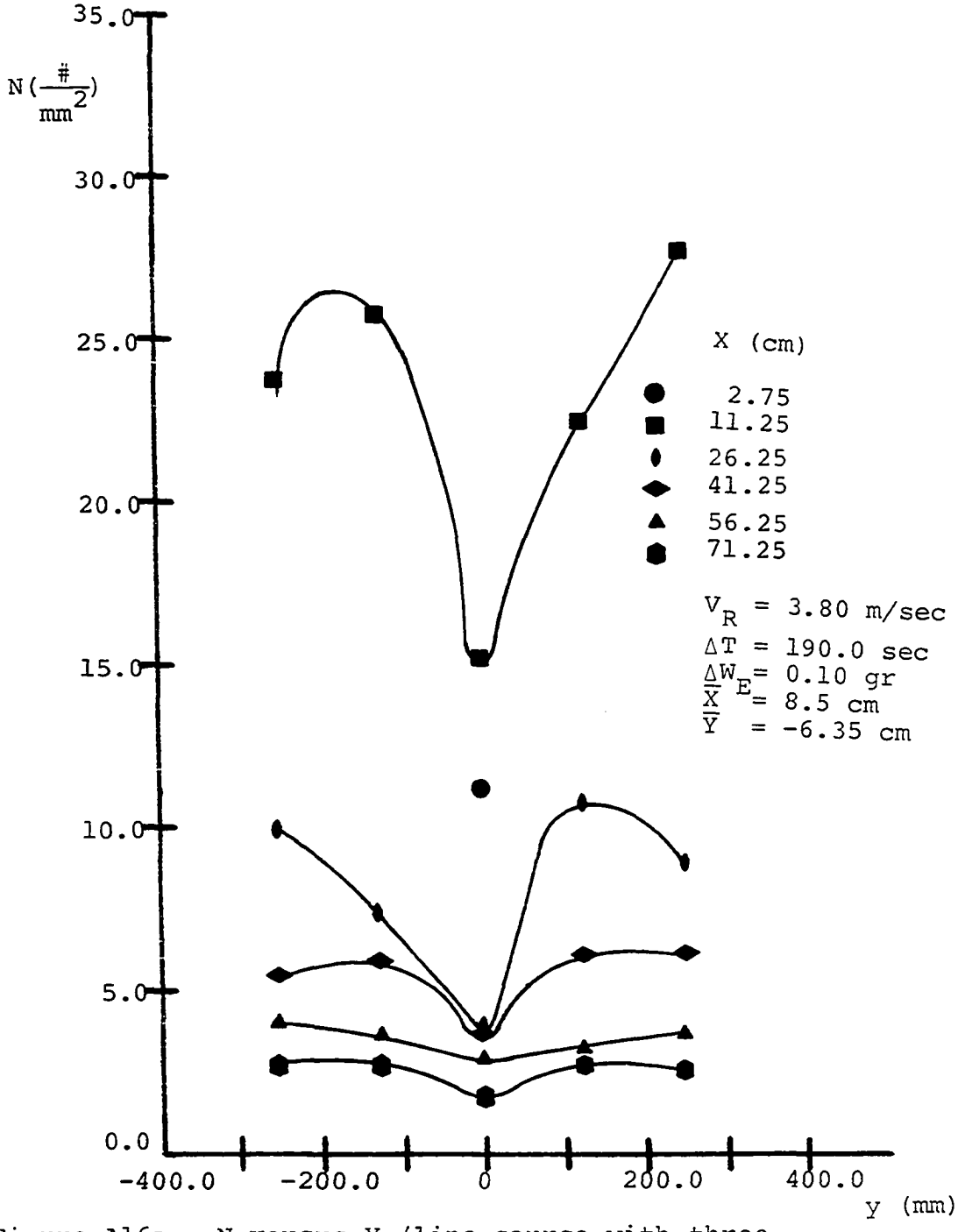

Figure A16a. N versus Y (line source with three-dimensional obstacle)

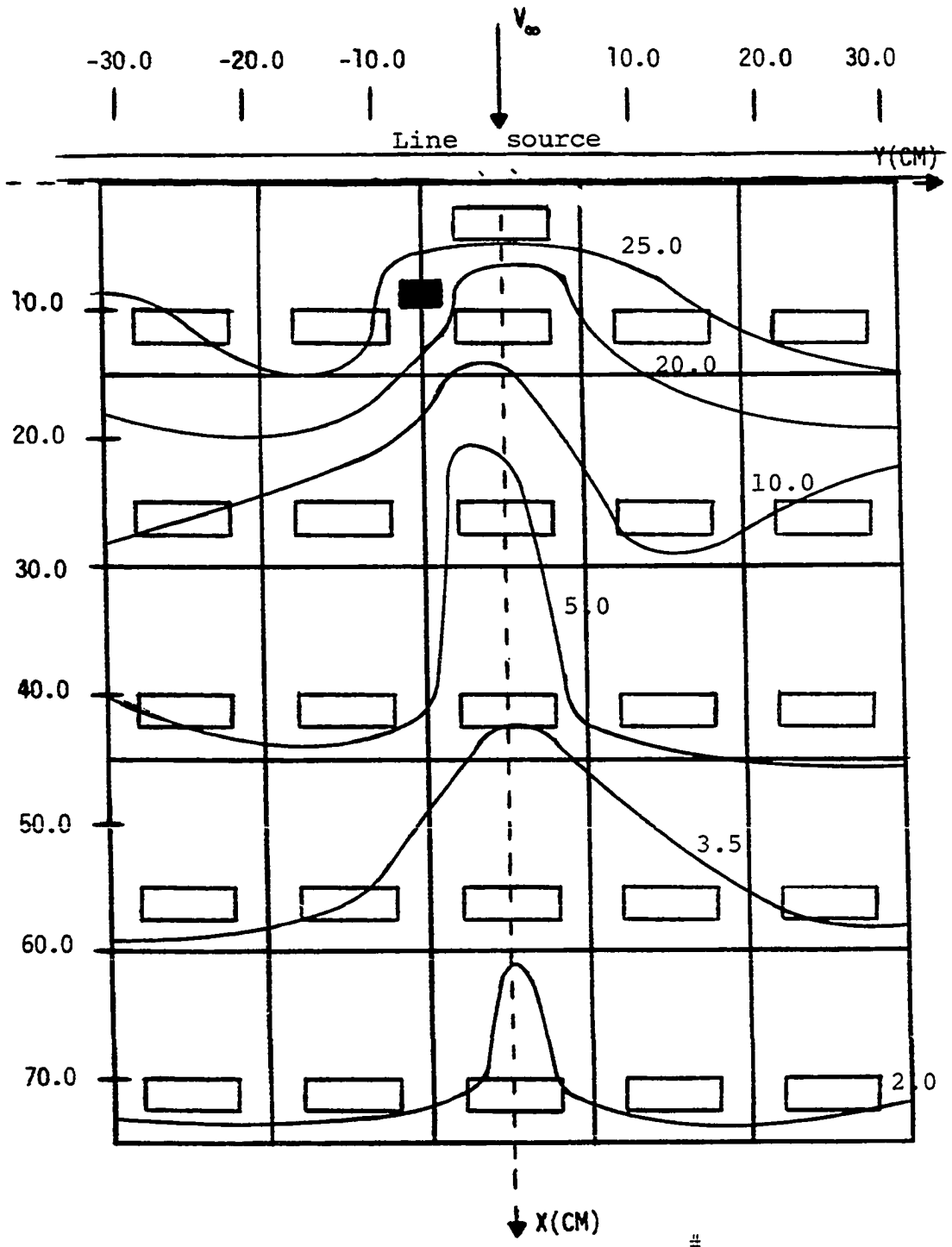

Figure A16b. Concentration isolines $\left(\frac{\#}{mm^2}\right)$

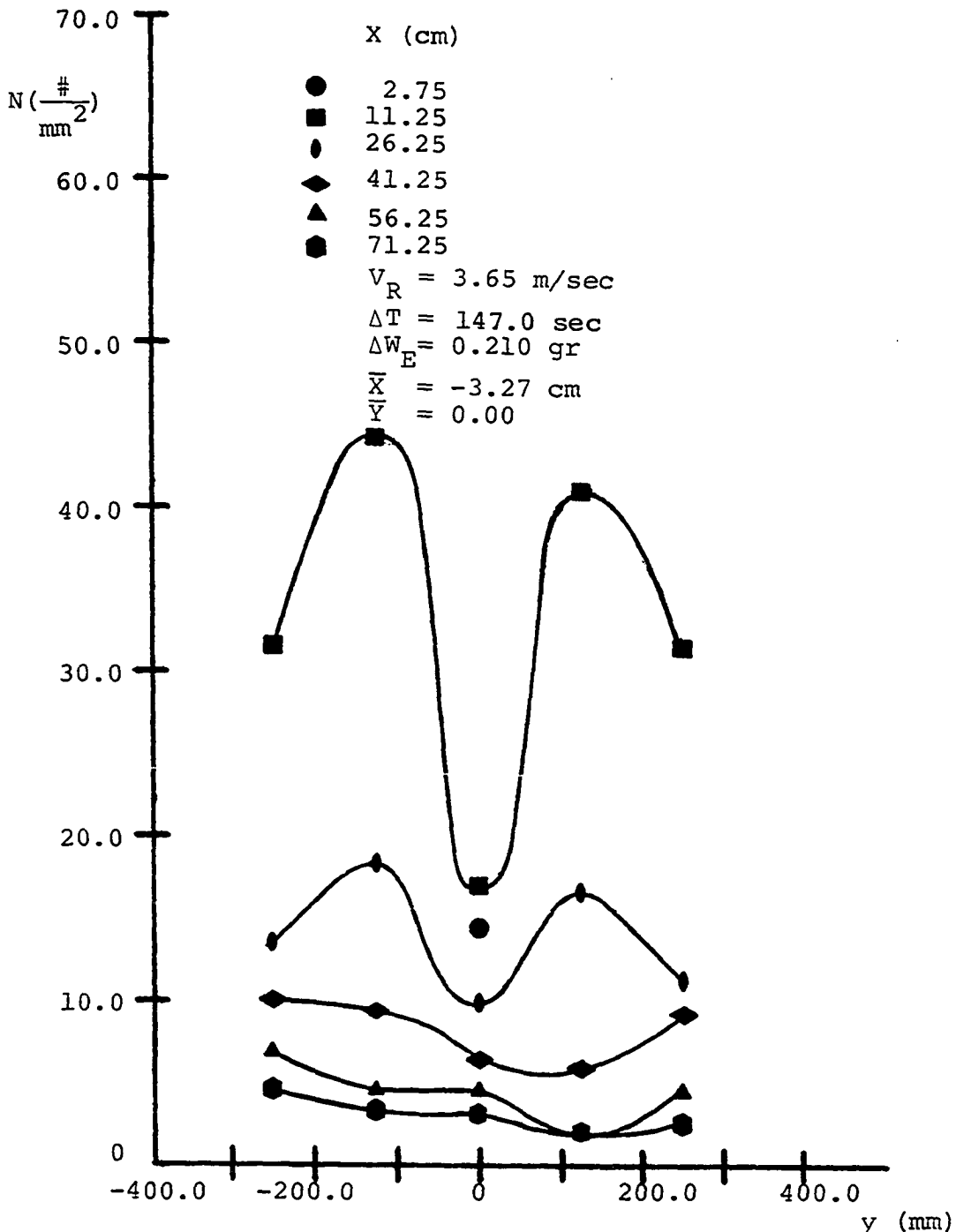

Figure A17a. N versus y (line source with three-dimensional obstacle)

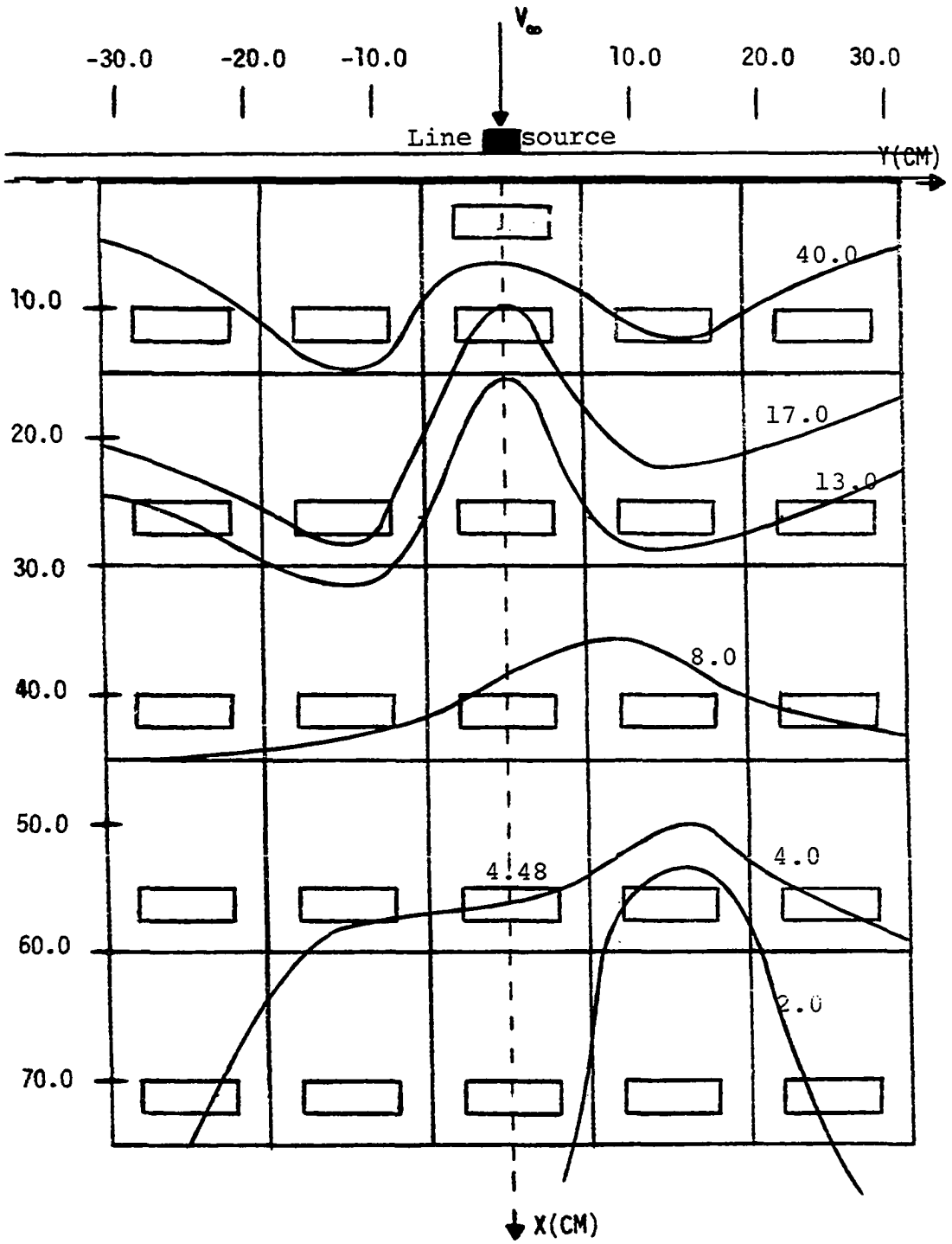

Figure A17b. Concentration isolines $(\frac{\#}{mm^2})$

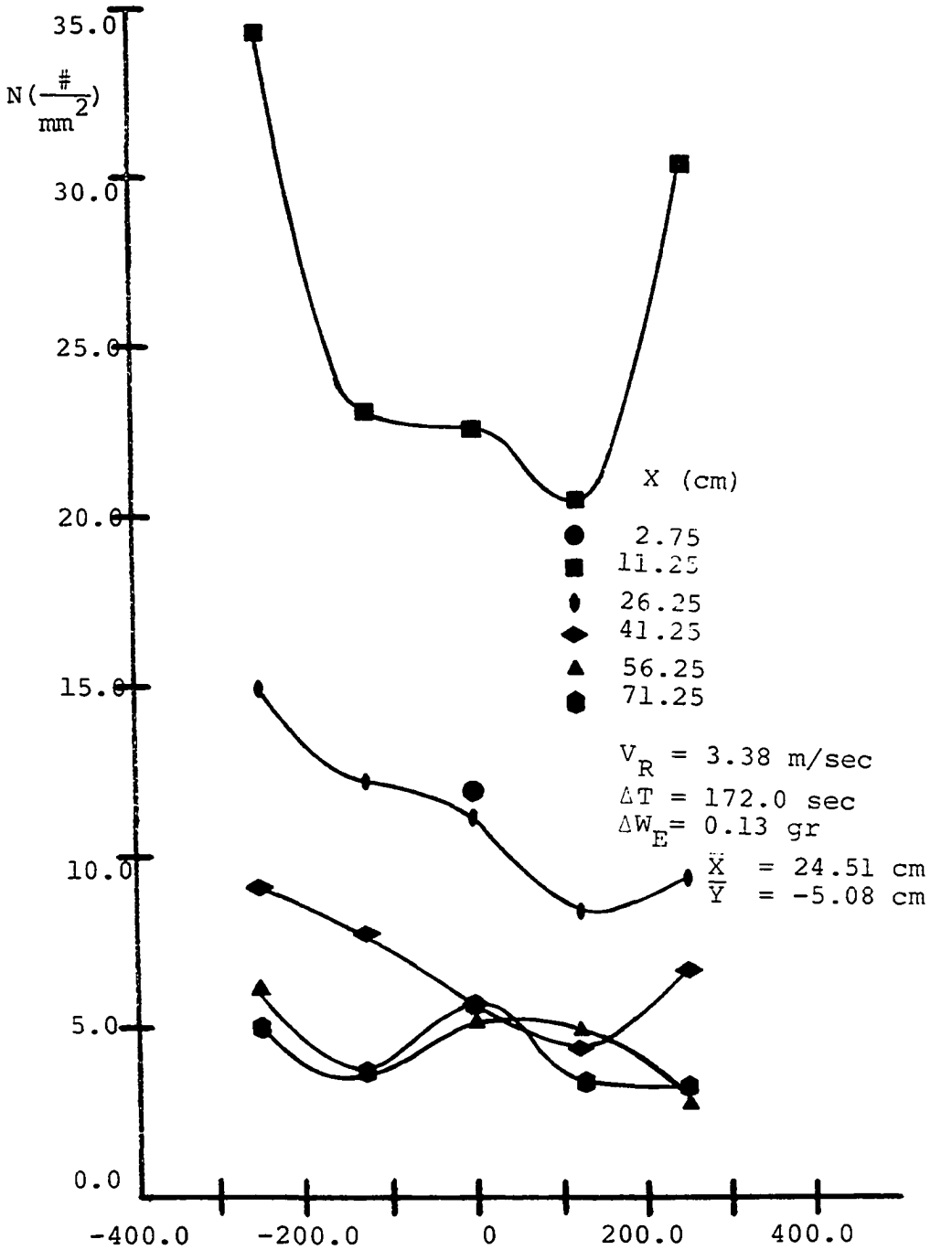

Figure A18a. N versus y (line source with three-dimensional obstacle)

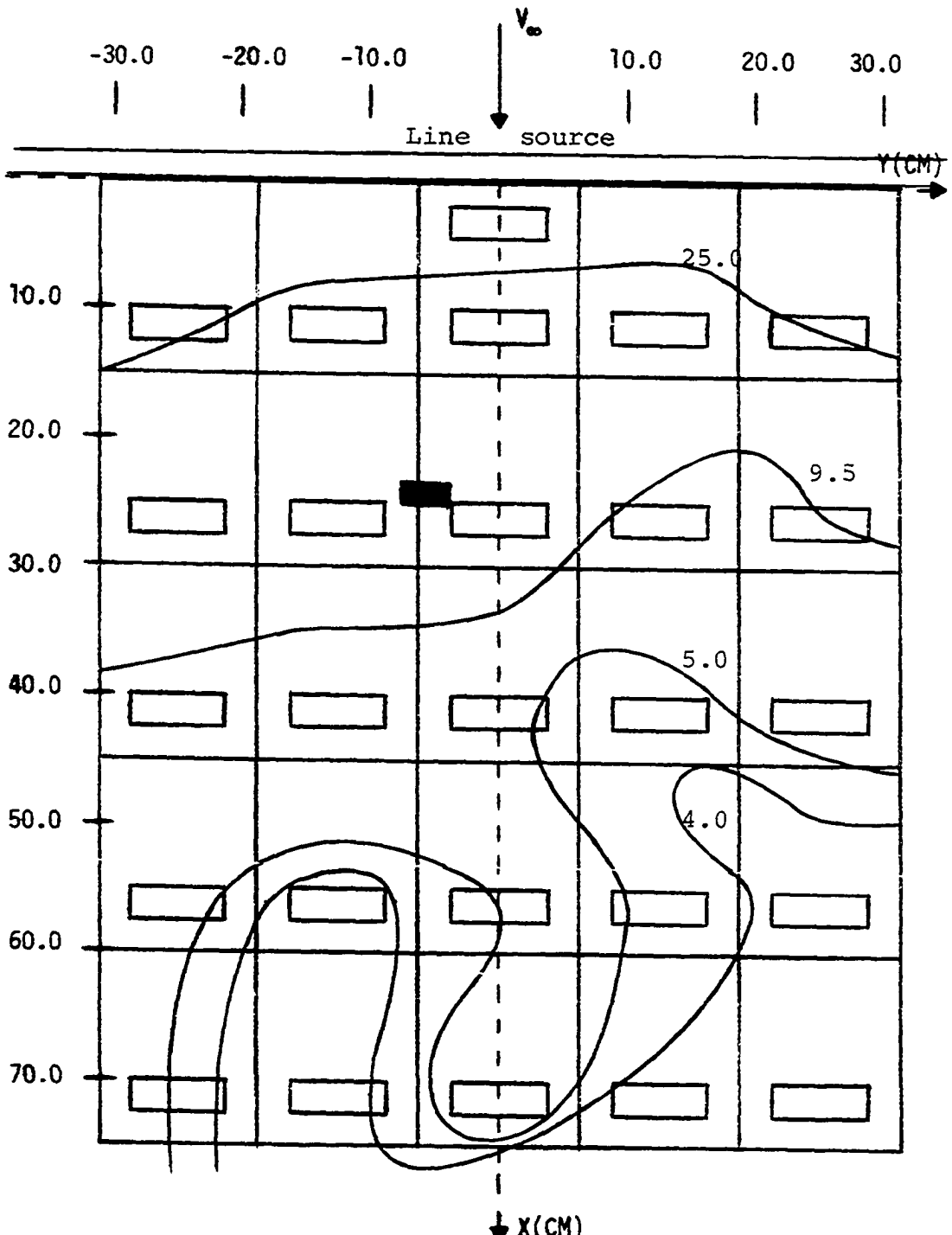

Figure A18b. Concentration isolines $(\frac{\#}{mm^2})$

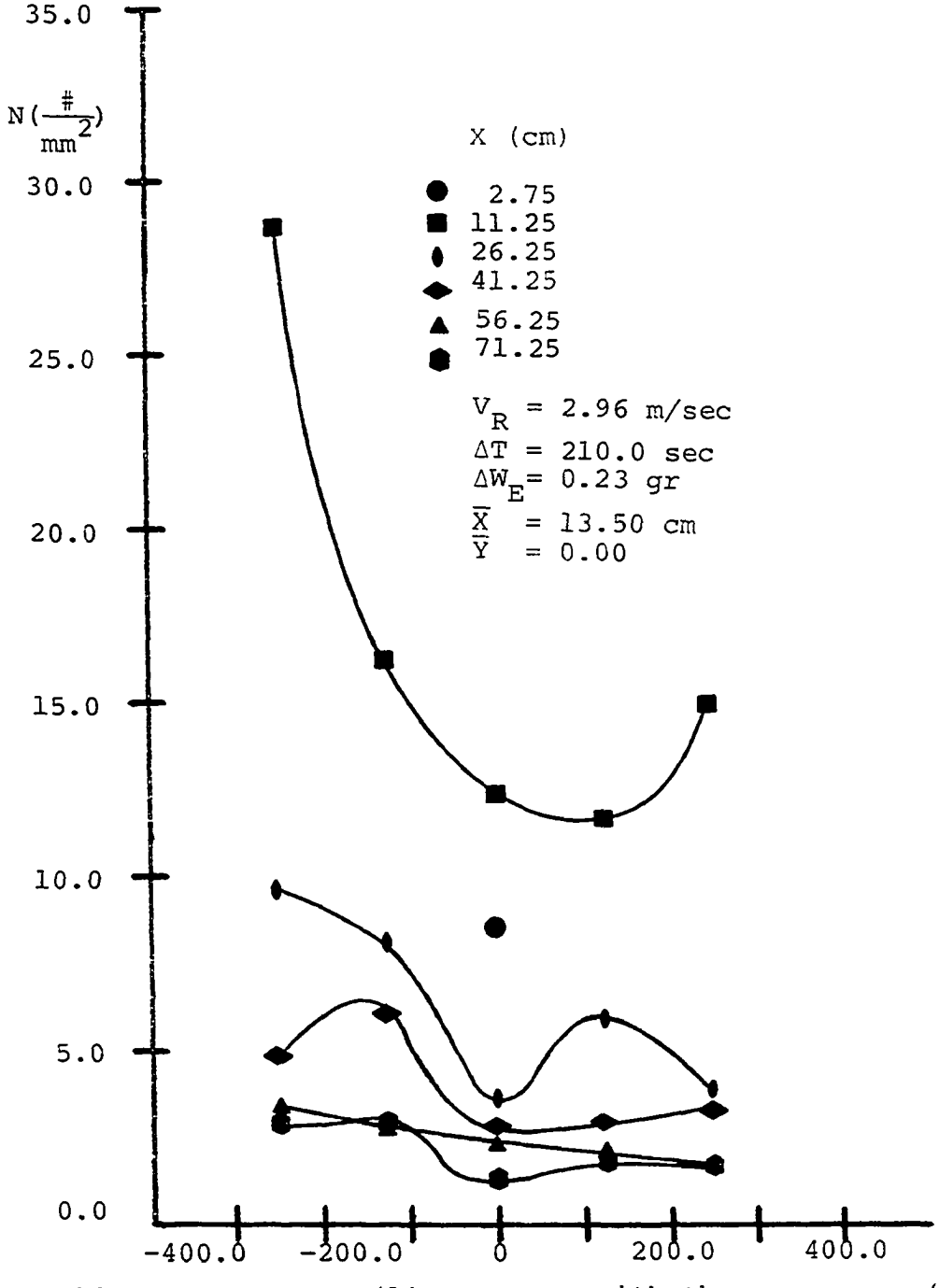

Figure A19a. N versus y (line source with three-dimensional obstacle)

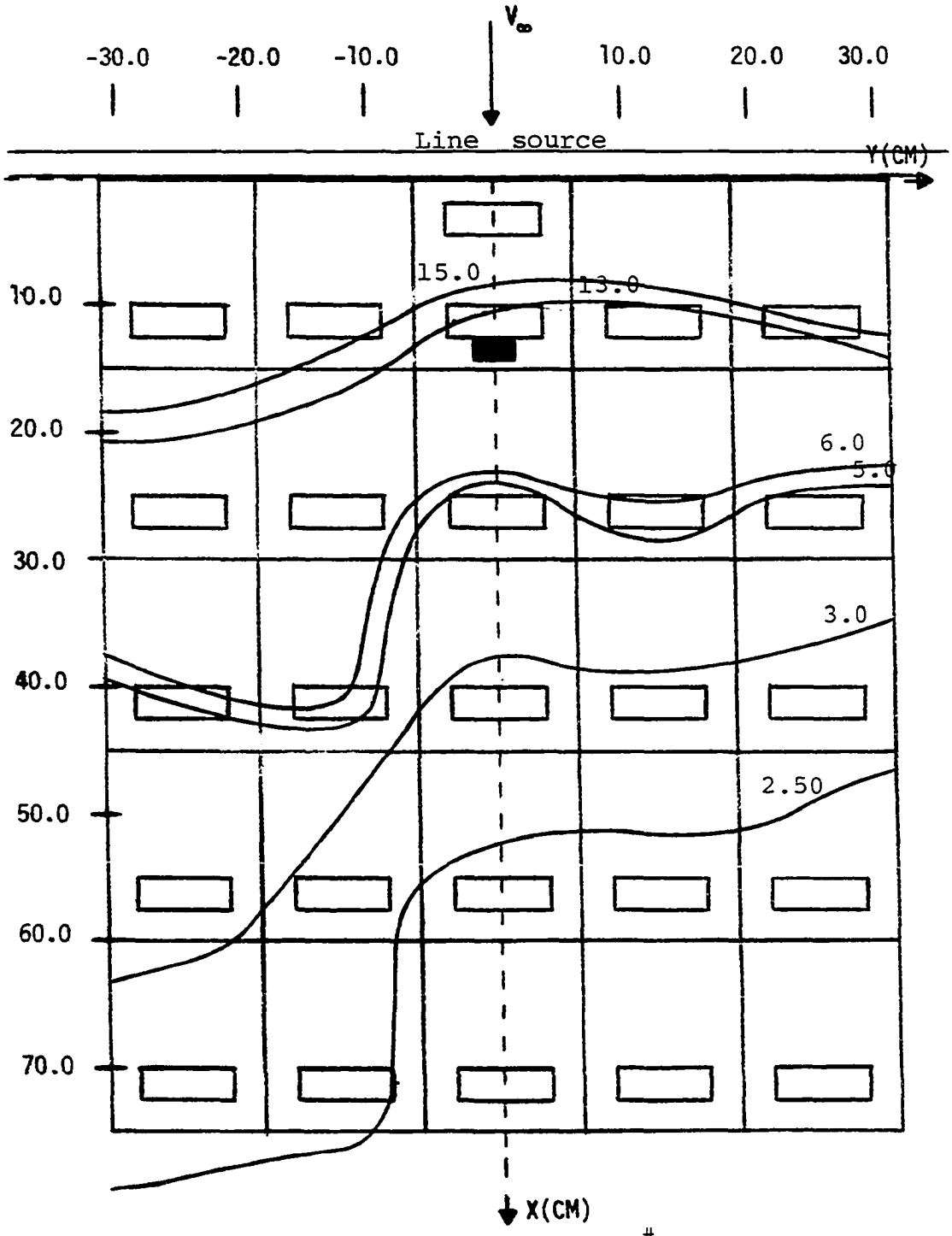

Figure A19b. Concentration isolines $(\frac{\#}{mm^2})$

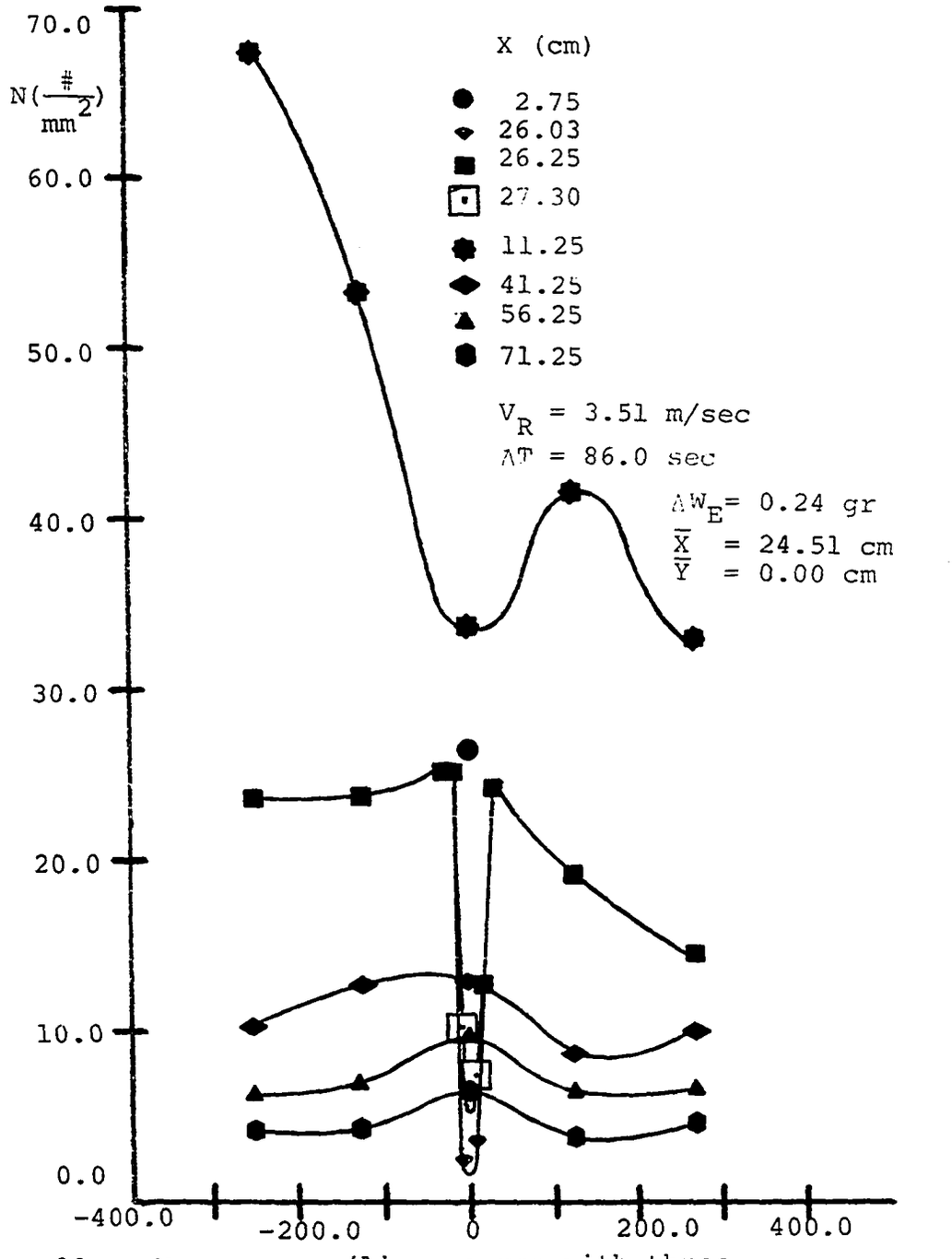

Figure A20a. N versus y (line source with three-dimensional obstacle)

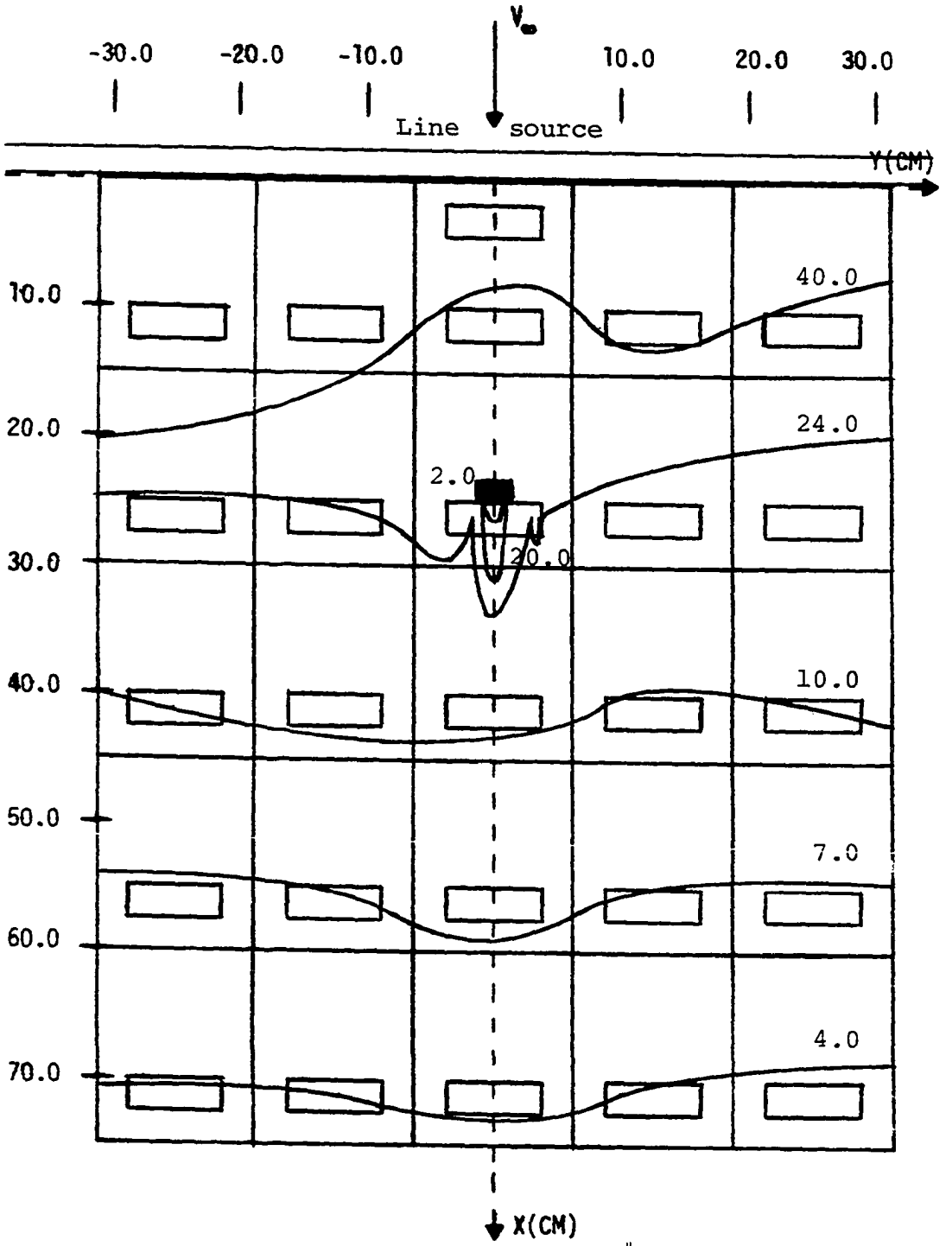

Figure A20b. Concentration isolines ($\frac{\#}{mm^2}$)

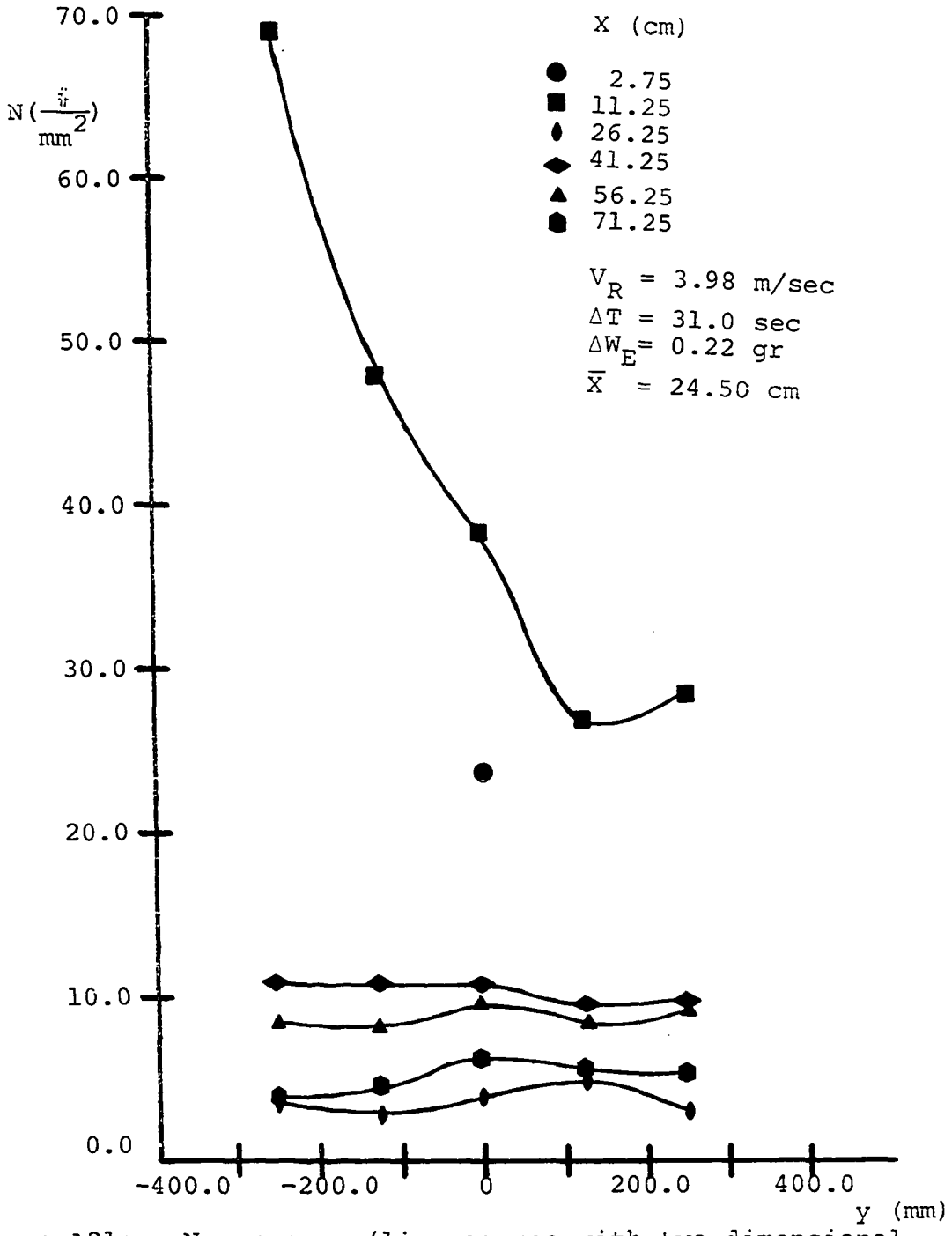

Figure A21a. N versus y (line source with two-dimensional obstacle)

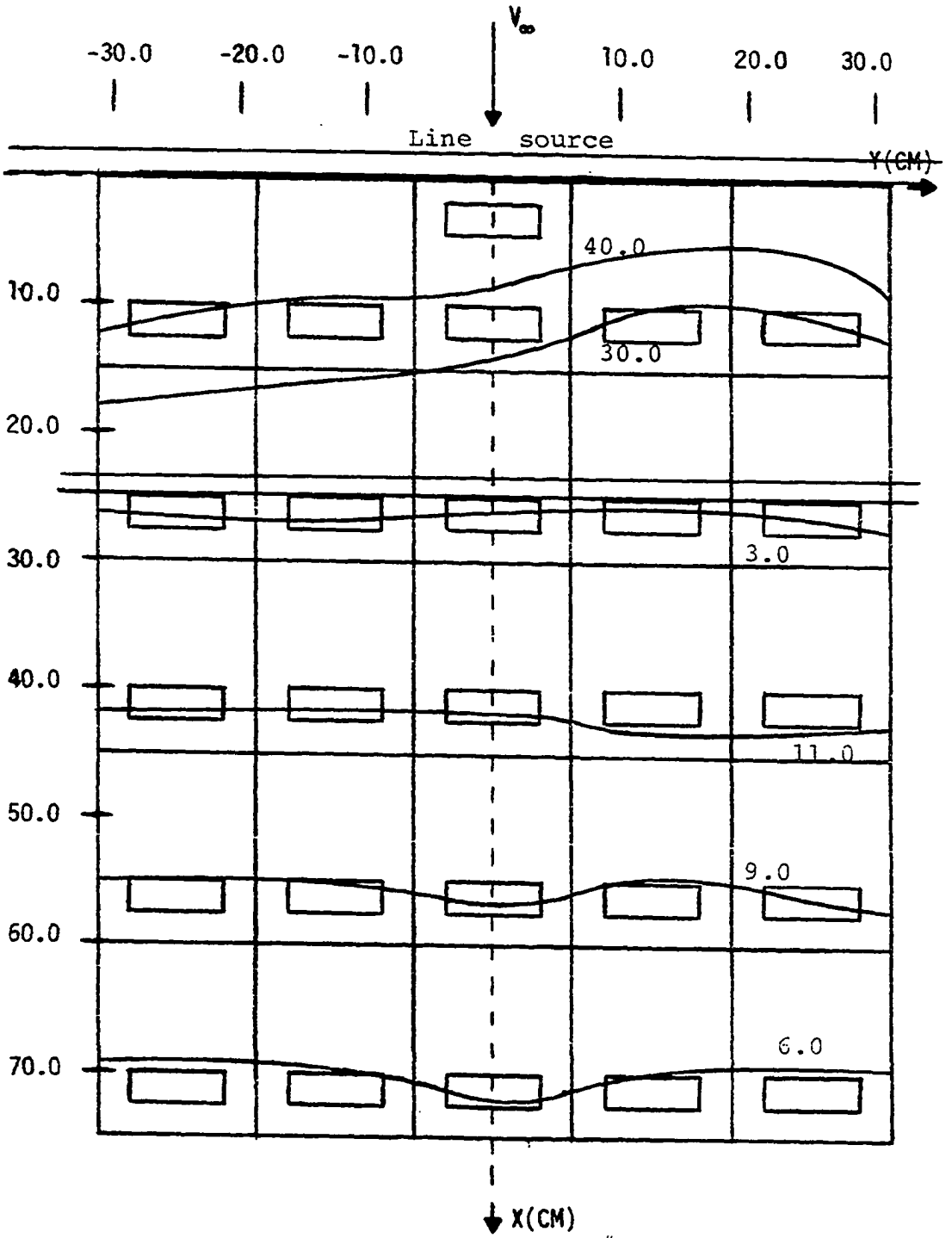

Figure A21b. Concentration isolines $(\frac{\#}{mm^2})$

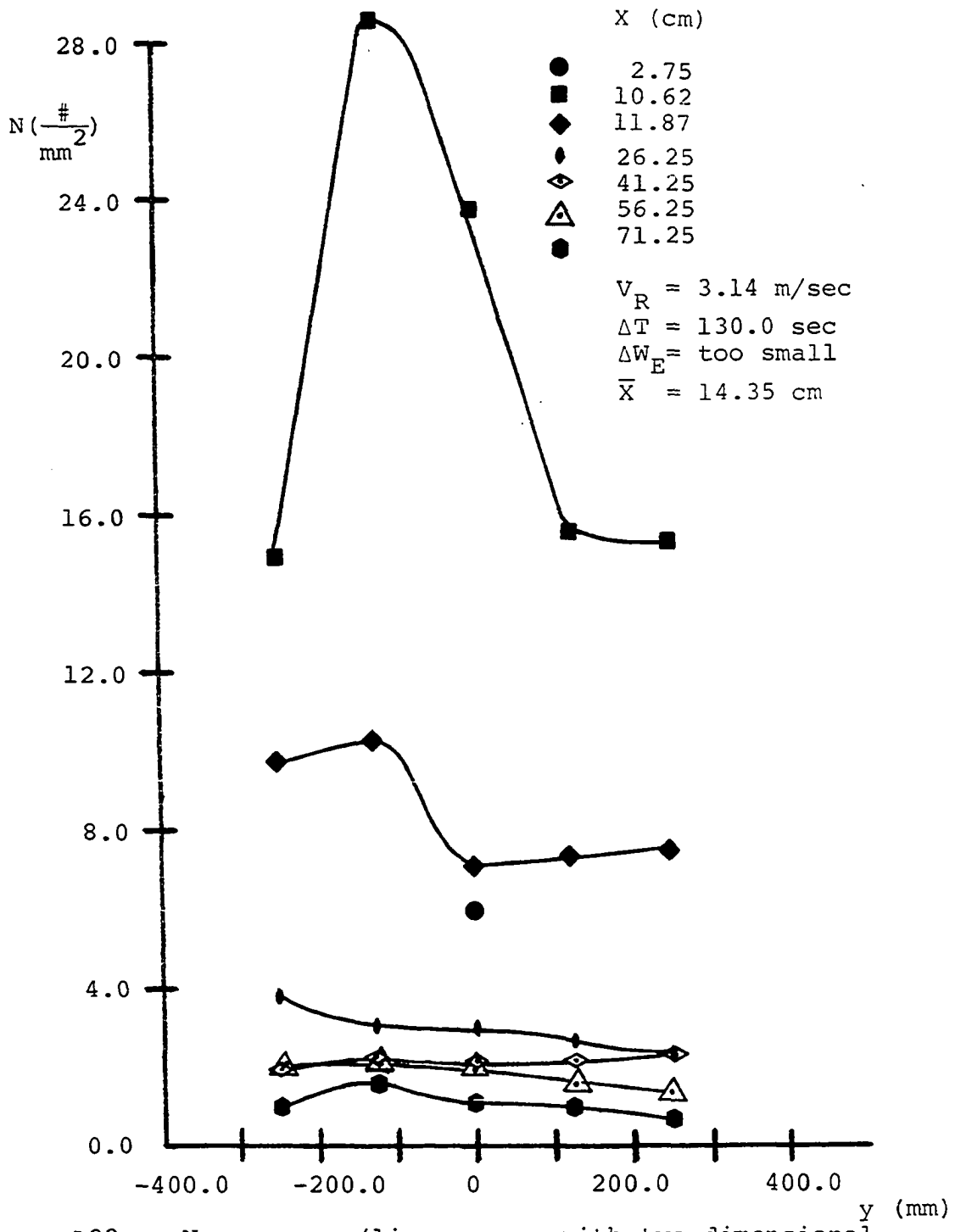

Figure A22a. N versus y (line source with two-dimensional obstacle)

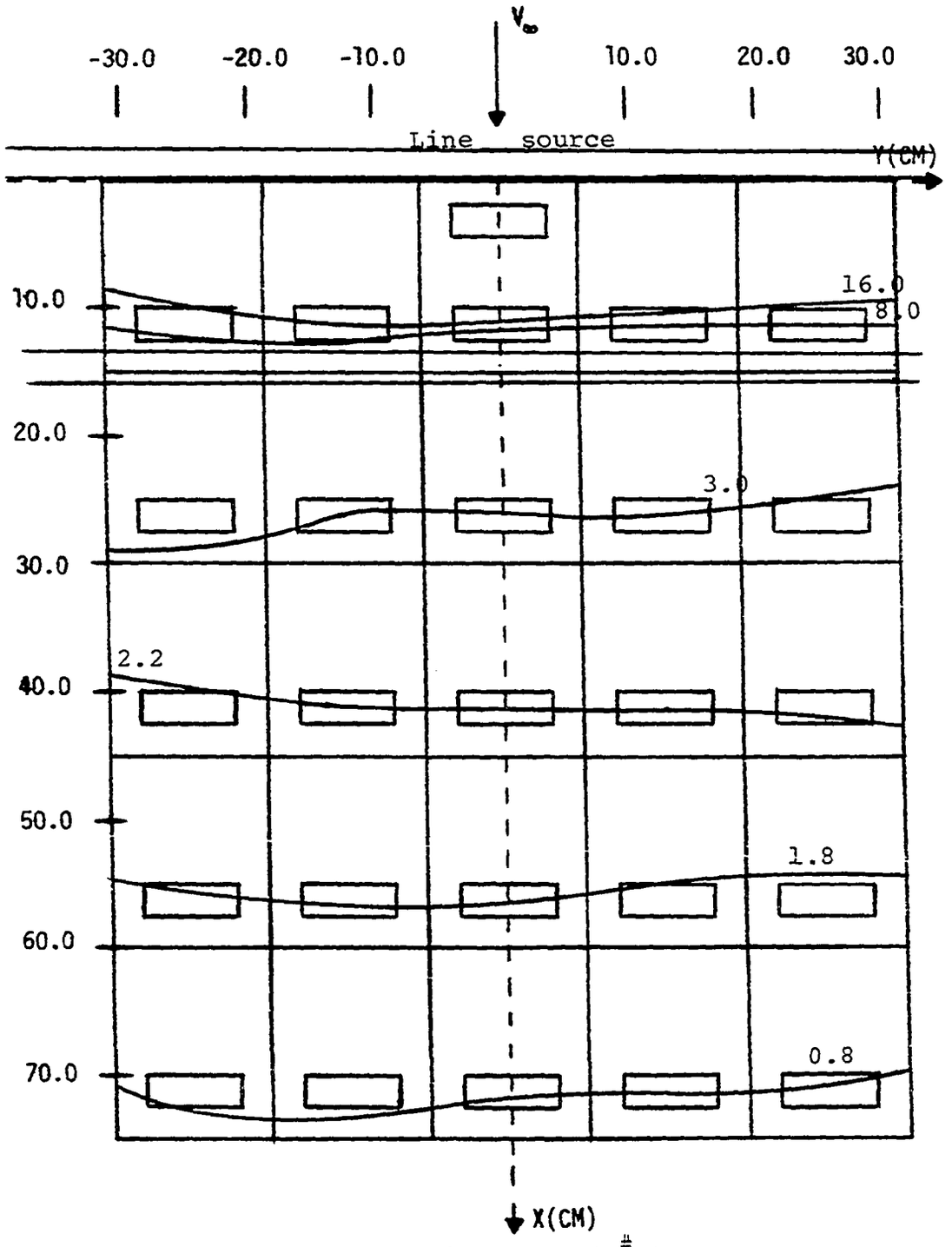

Figure A22b. Concentration isolines ($\frac{\#}{mm^2}$)

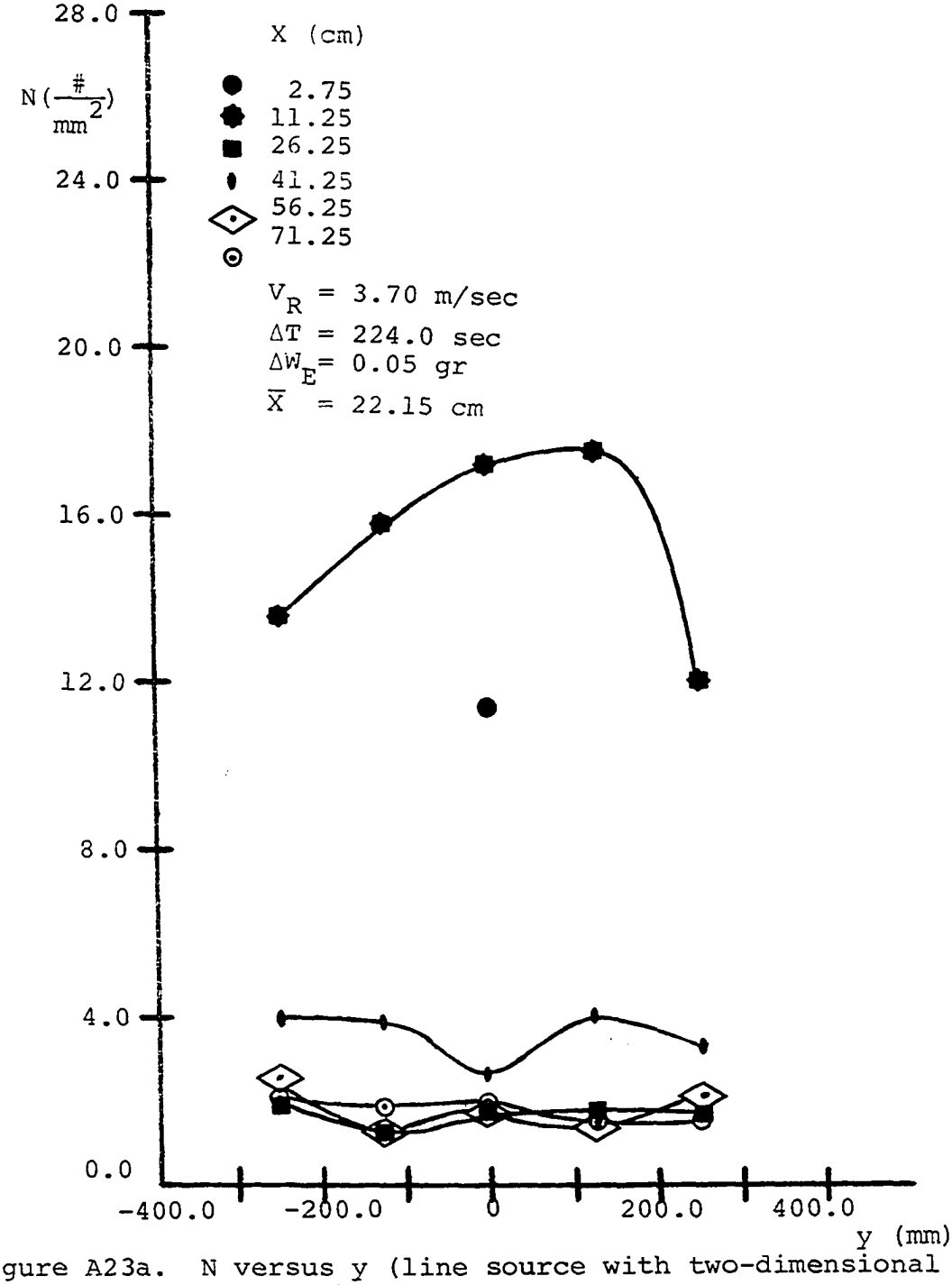

Figure A23a. N versus y (line source with two-dimensional obstacle)

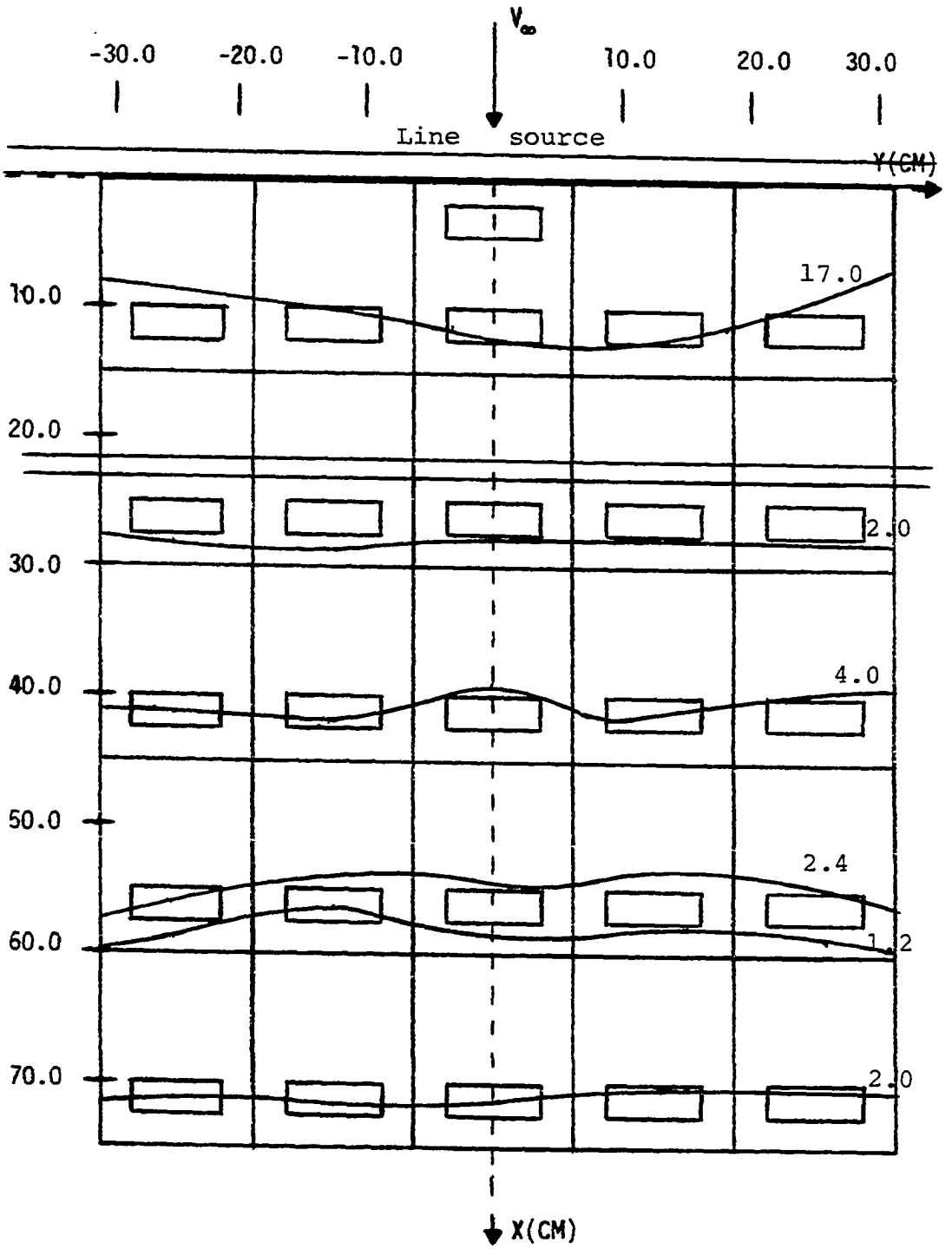

Figure A23b. Concentration isolines $(\frac{\#}{mm^2})$

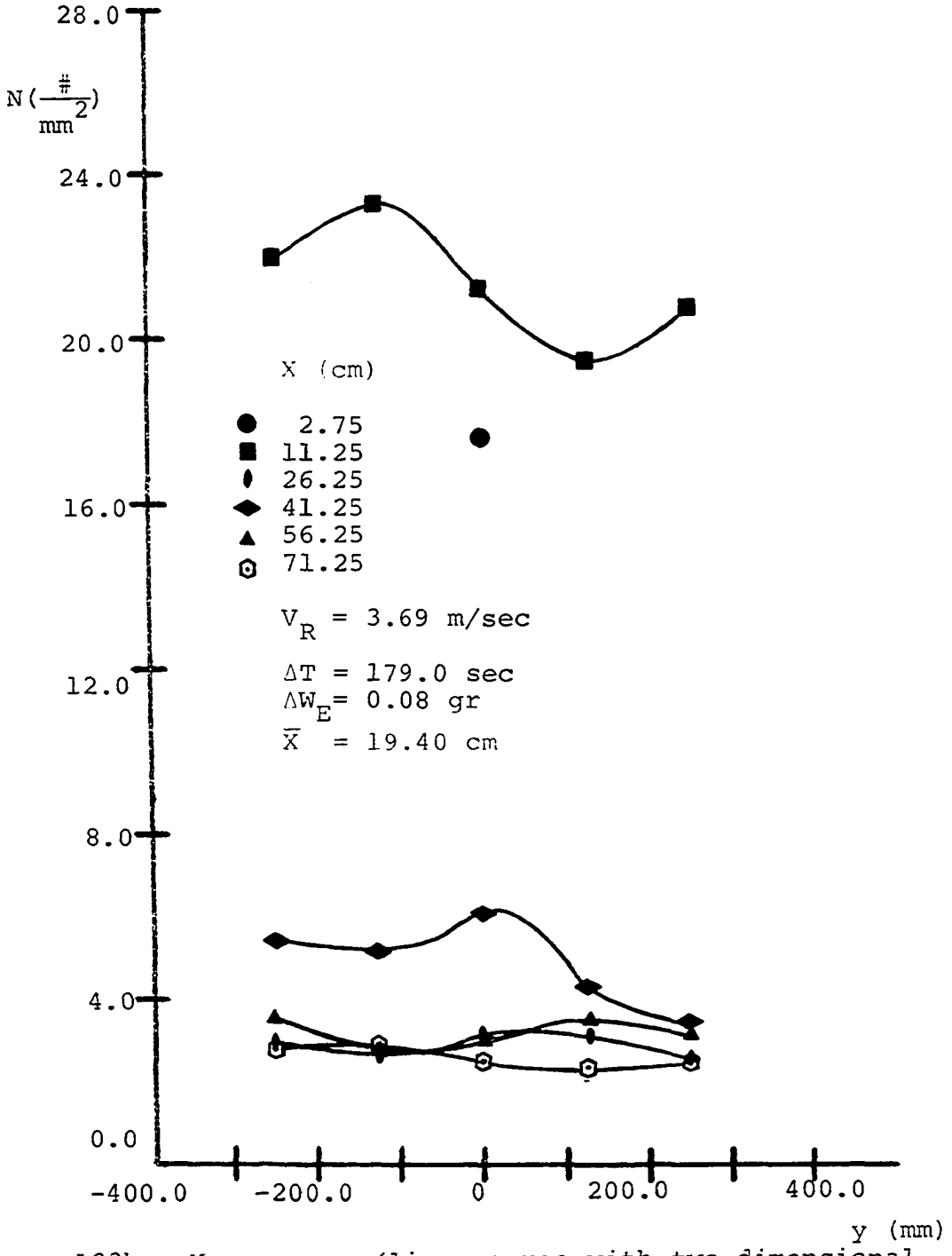

Figure A23b. N versus y (line source with two-dimensional obstacles)

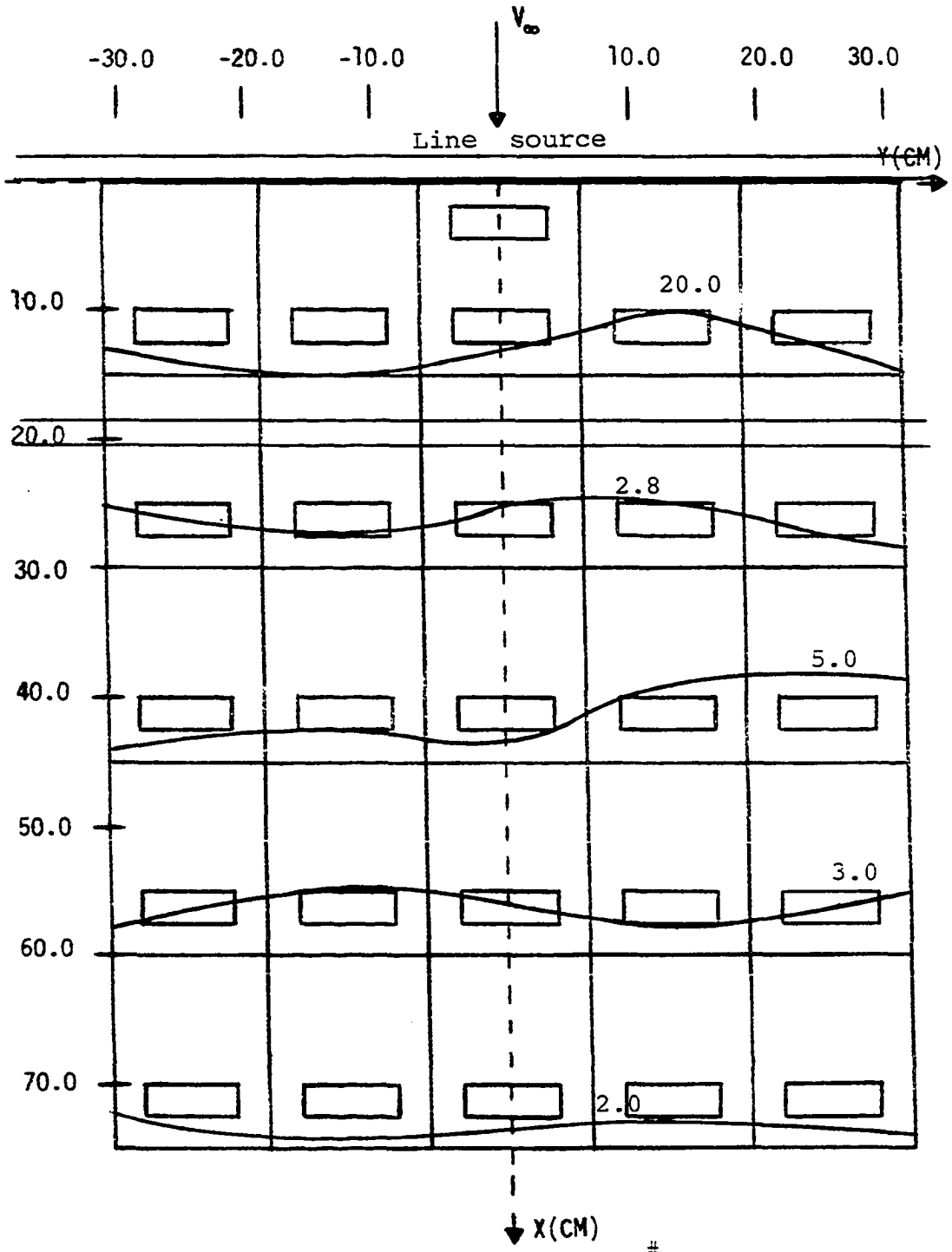

Figure A24b. Concentration isolines $(\frac{\#}{mm^2})$

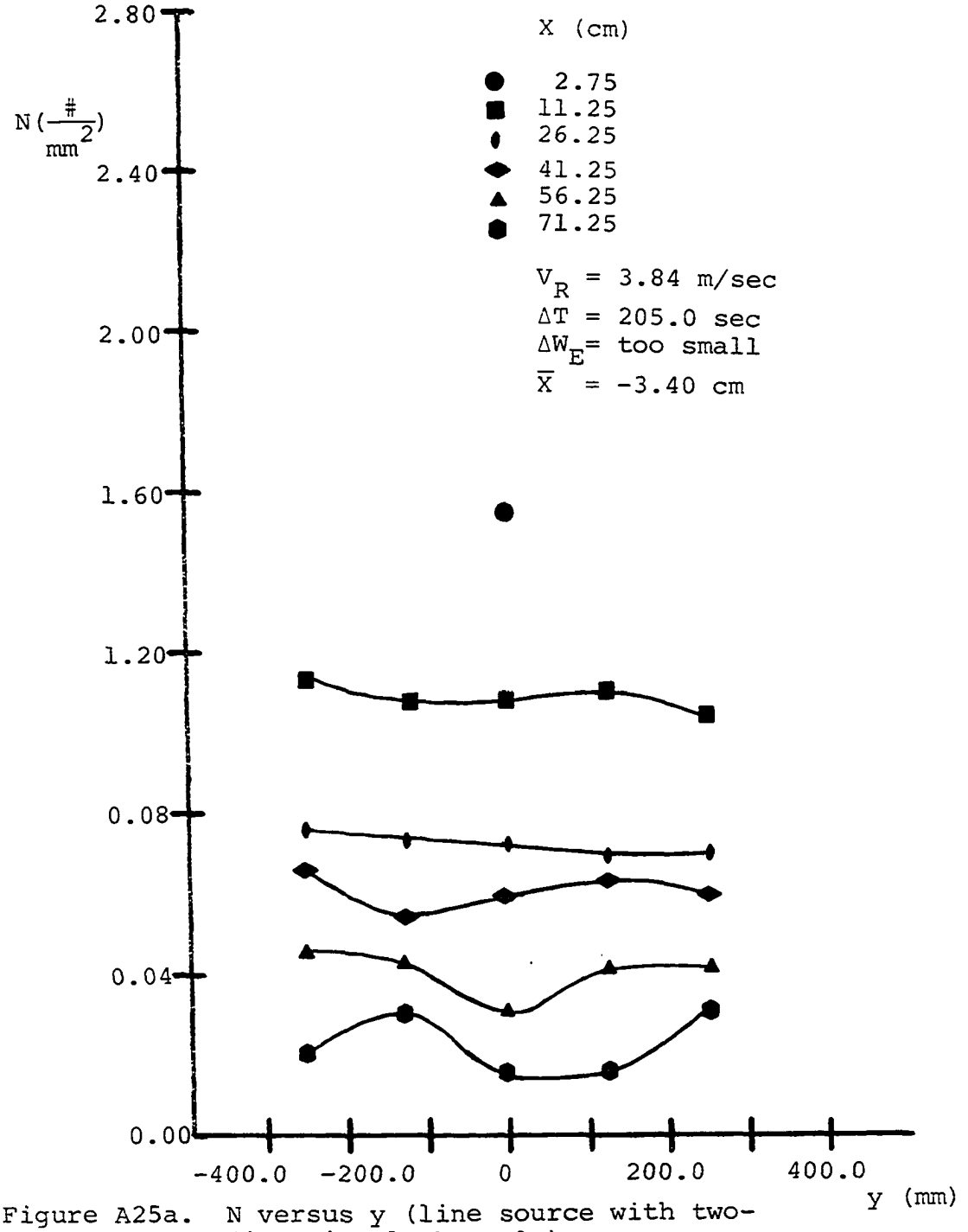

Figure A25a. N versus y (line source with two-dimensional obstacle)

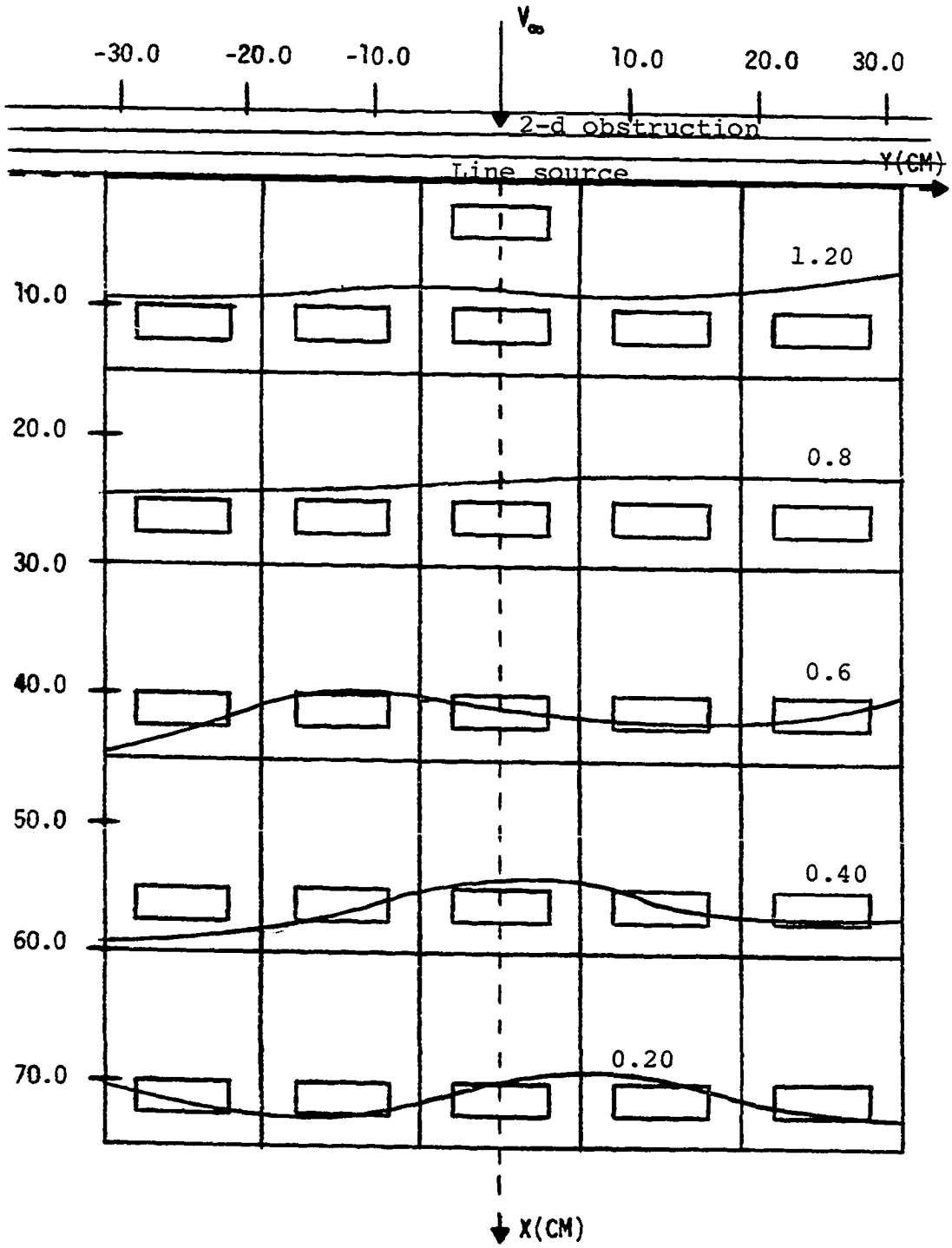

Figure A25b. Concentration isolines $(\frac{\#}{mm^2})$

APPENDIX B: BOUNDARY LAYER PROFILES

An axis system $o_1x_1y_1z_1$, with origin at o_1, and x_1, y_1, z_1 axes parallel to the x, y, z axes is used as a reference coordinate frame in which the centroidal positions of the obstacles are measured (Figure 10). The o_1z_1 axis coincides with the axis of the probe and is parallel with the traverse mechanism and the oz axis. It can be seen from Figure 10 that the hot wire is positioned such that it can measure any backflow which might encounter in the vicinity of the obstacles.

The distance oo' is 35.0 cm and was kept constant throughout the boundary layer survey measurements. The wind profiles were measured for line source with the three- (Figure B1) and the two-dimensional (Figure B2) obstacles. The longitudinal positions of the obstacles were varied along the o_1x_1 axis upstream and downstream of the hot wire, while their lateral position was fixed at $y_1=0$. The wind profiles were also measured for the point source with the three-dimensional (Figure B3) obstacle in the x_1y_1 plane. In this case, the position of the obstacle was varied on the tunnel floor. The obstacles were displaced at arbitrary increments of x_1 and y_1 until no apparent effects due to the obstacles were experienced by the hot wire. This procedure was used in all the test runs.

In Figures B1 through B3 the vertical axis corresponds

to the nonlinear voltage output from the hot wire. The horizontal axis is for the height measurements in units of centimeters. In order to obtain wind profiles in units of m/sec against height (Figure B4), the calibration of the hot wire is required. Equation B1 is the calibration (nonlinear) of the voltage in terms of wind speed in m/sec.

$$V_R = 12.436\ V_{HW}^{2.237}\ \text{m/sec} \qquad \text{(B1)}$$

The nonlinear voltage from the hot wire varies between 0.00 for zero wind to 0.78 volts for full scale wind (here 7.13 m/sec). The wind speed outside of the boundary layer (Figures B1 through B3) therefore is 0.78 volts and corresponds to 7.13 m/sec (from Equation B1). The height scale on the other hand varies from zero (on paper) corresponding to 0.25 cm height (actual) to full scale (on paper) for 32.86 cm height (actual).

Figure B4 is the boundary layer profile of the wind tunnel and corresponds to Figure B1 for x_1 = 20.32 cm. The value of z_o is assumed to be a constant since the Reynolds number $\frac{V_* z_o}{\nu}$ is larger than 7/3. The wind profiles for reference speeds other than 7.13 m/sec can be approximated by assuming that the boundary layer thickness does not change. Note that this approximation is not valid if $\frac{V_* Z_o}{\nu}$ becomes smaller than 7/3.

The wind profiles around the obstacles as shown in

Figures B1 through B3 need to be formulated individually. These profiles were obtained to eventually be used as input into the numerical methods described in Chapter IV.

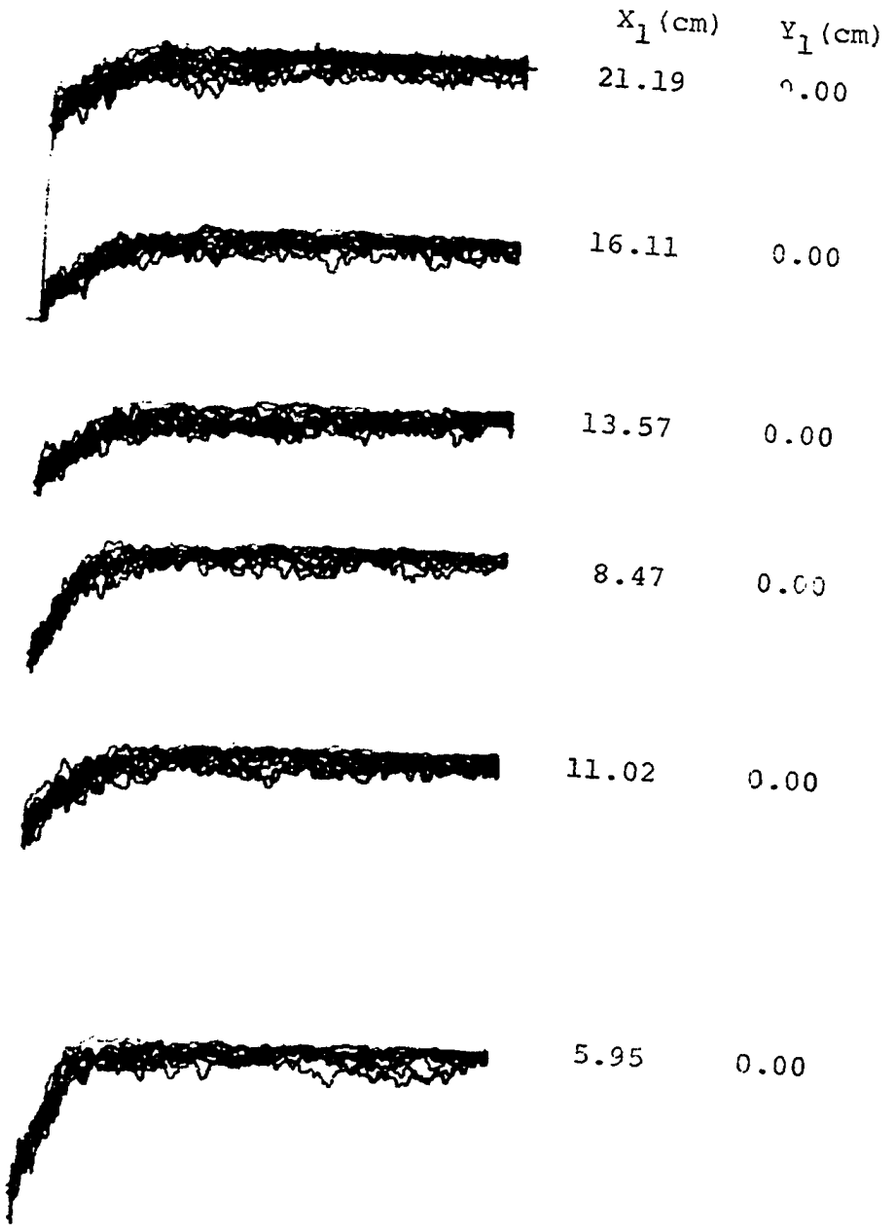

Figure B1. Boundary layer profiles of the three-dimensional obstacle at various X positions (line source was present)

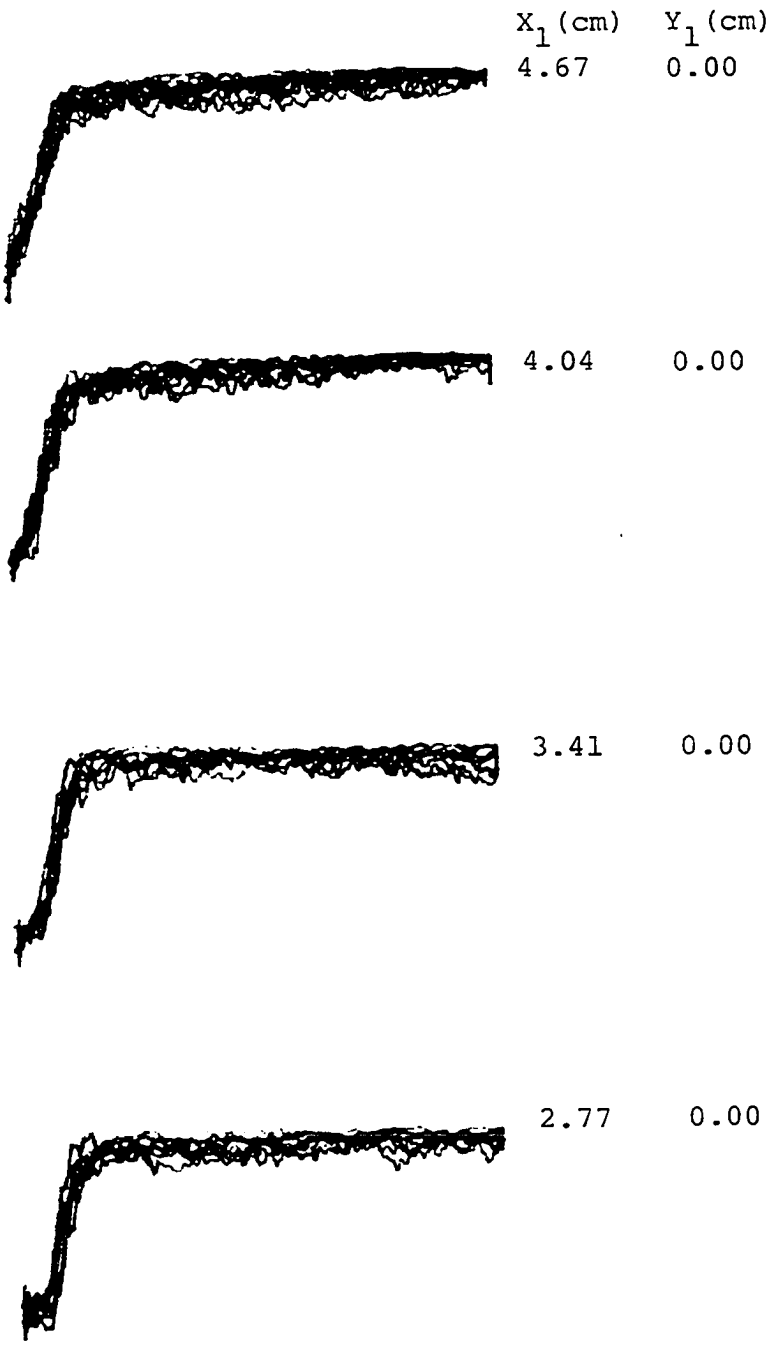

Figure B1 (Continued)

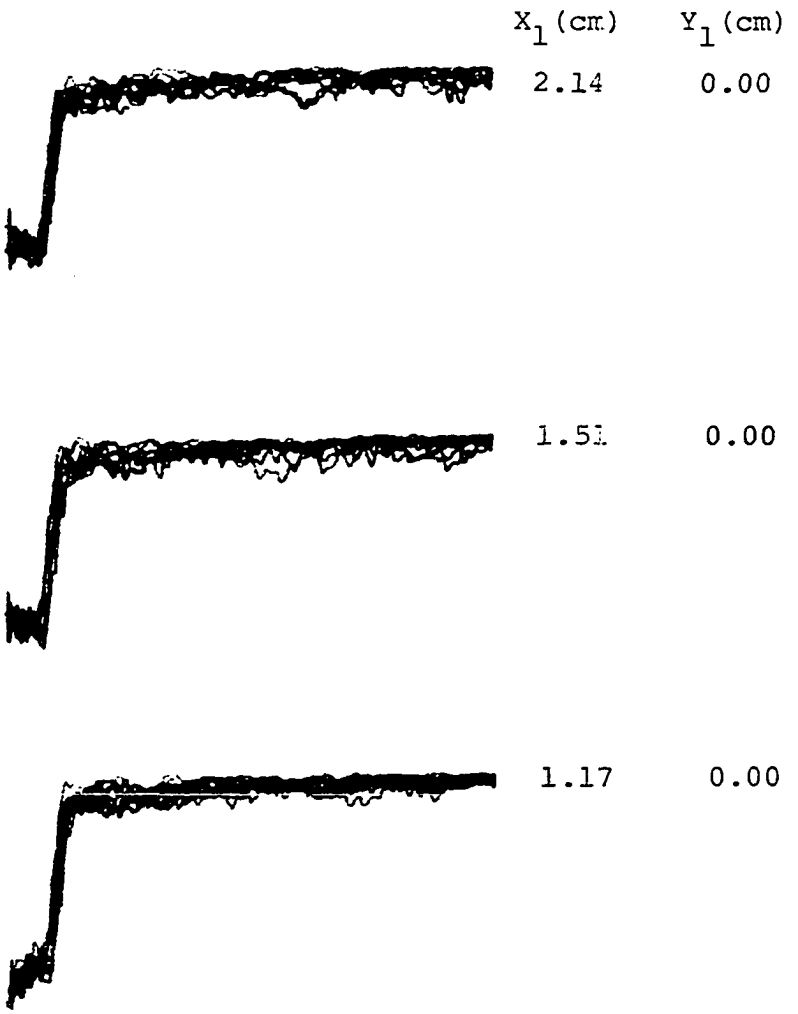

Figure B1 (Continued)

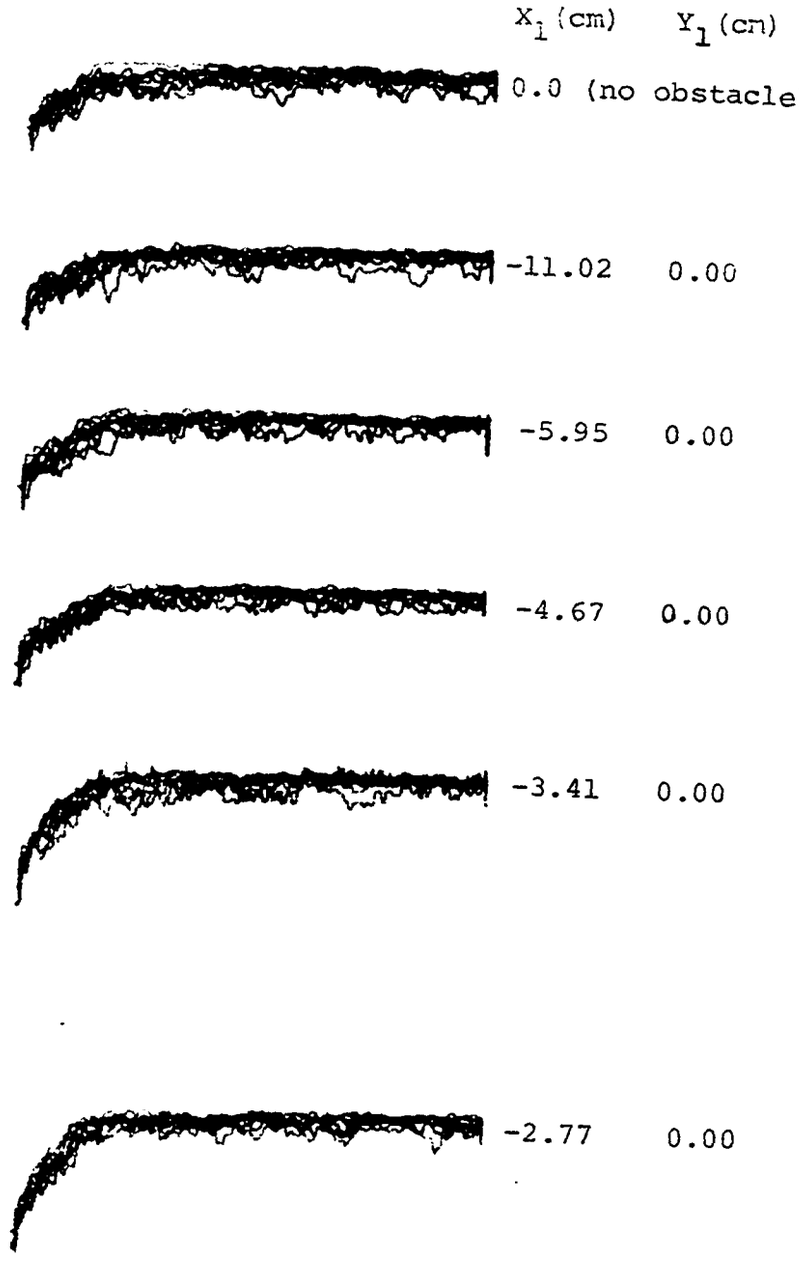

Figure B1 (Continued)

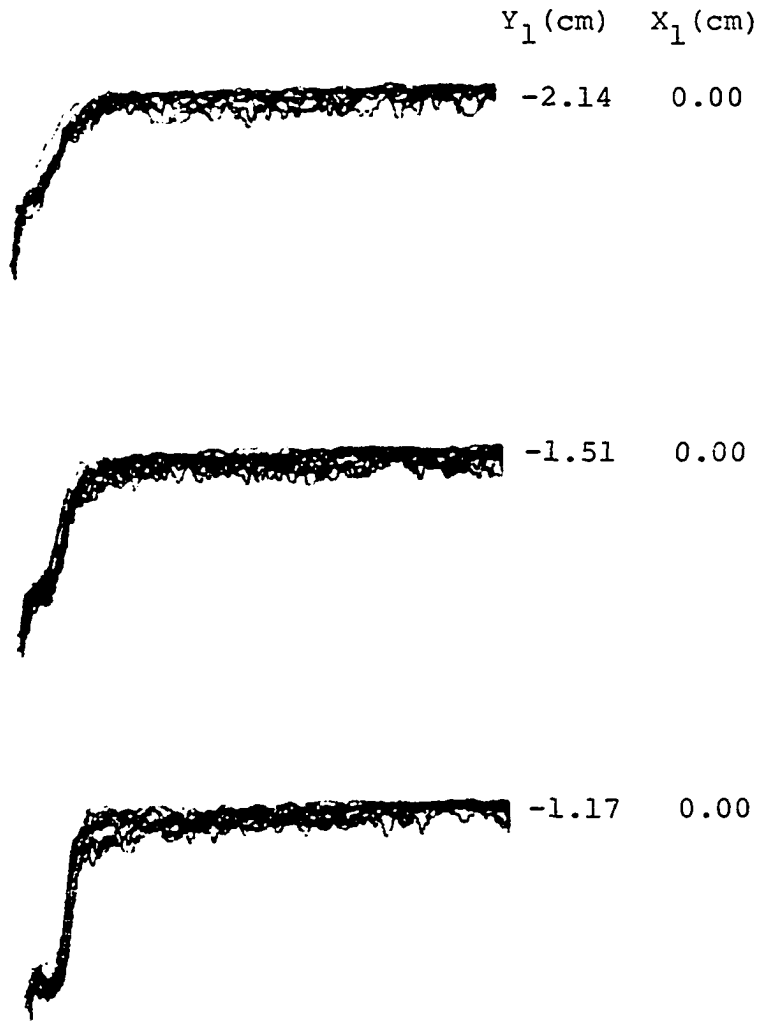

Figure B1 (Continued)

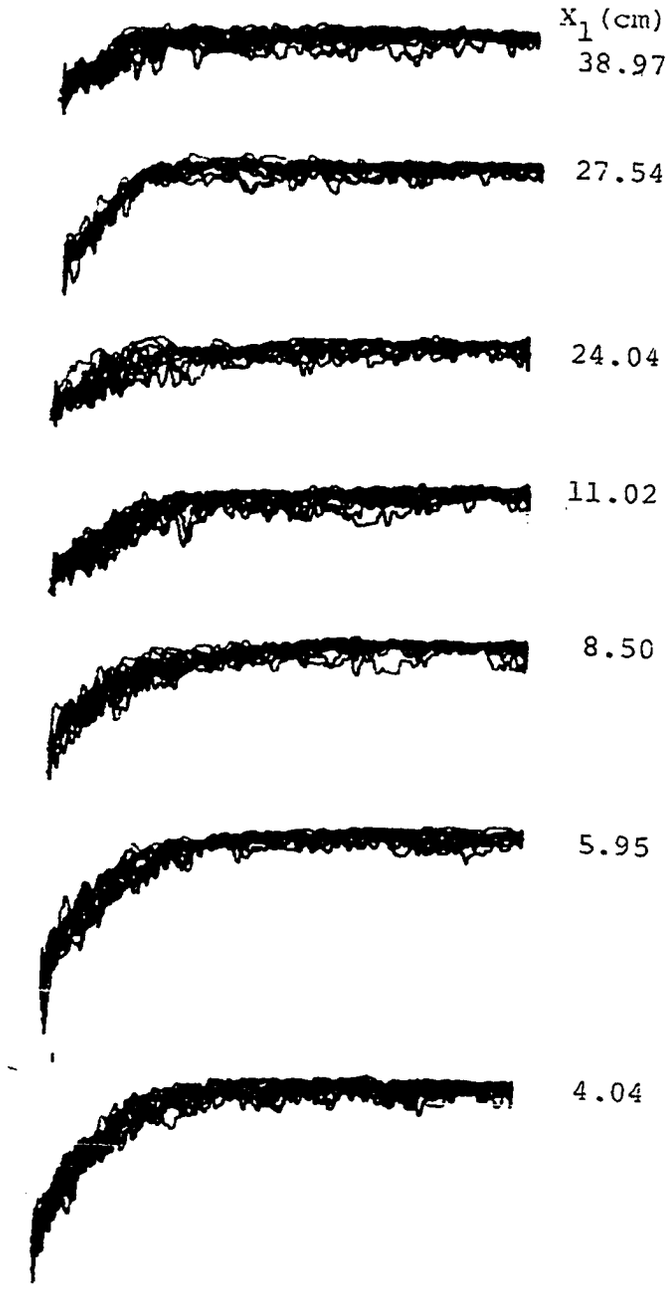

Figure B2. Boundary layer profiles of the two-dimensional obstacles at various X_1 positions (line source was present)

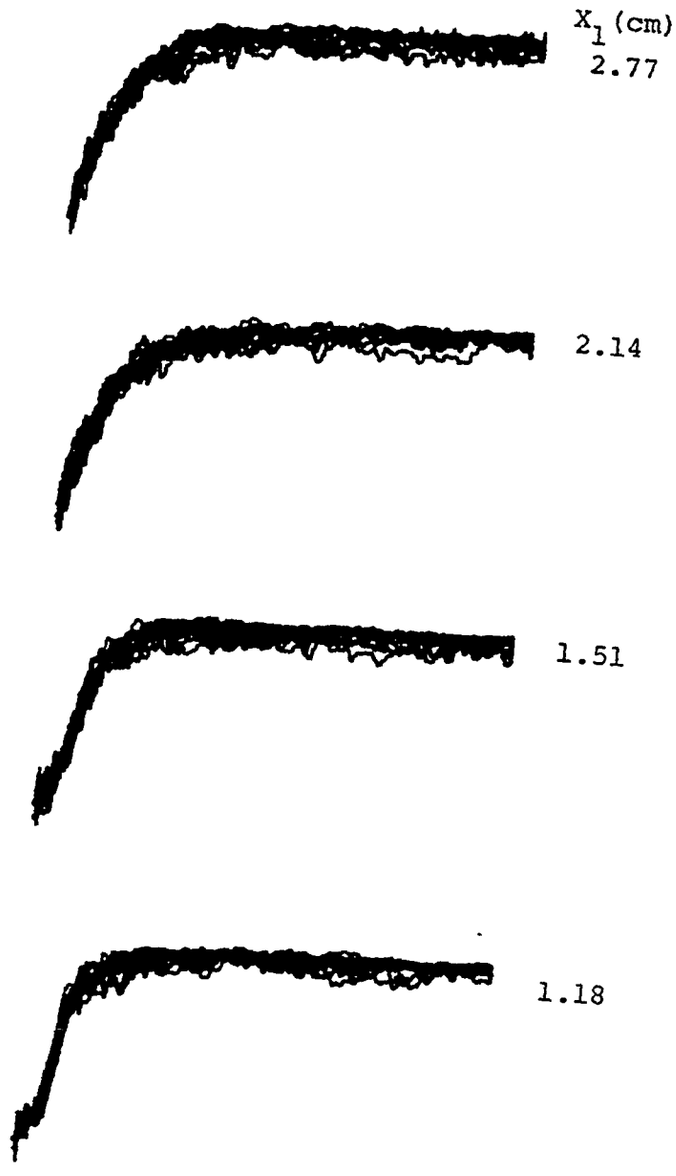

Figure B2 (Continued)

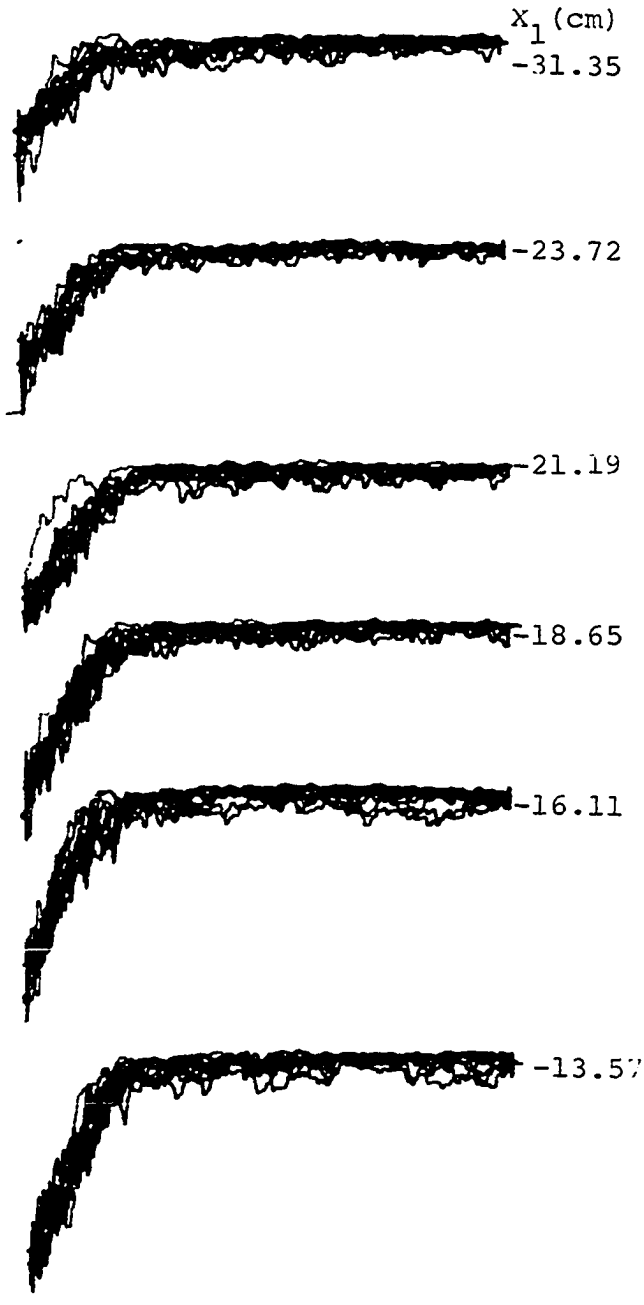

Figure B2 (Continued)

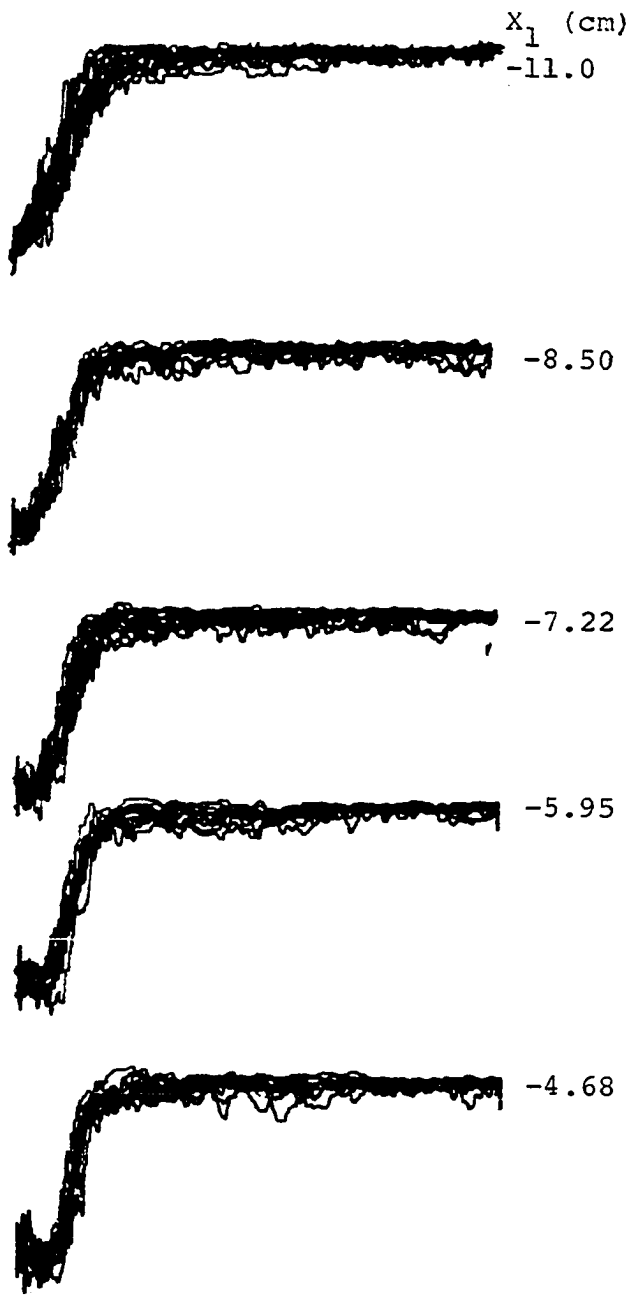

Figure B2 (Continued)

Figure B2 (Continued)

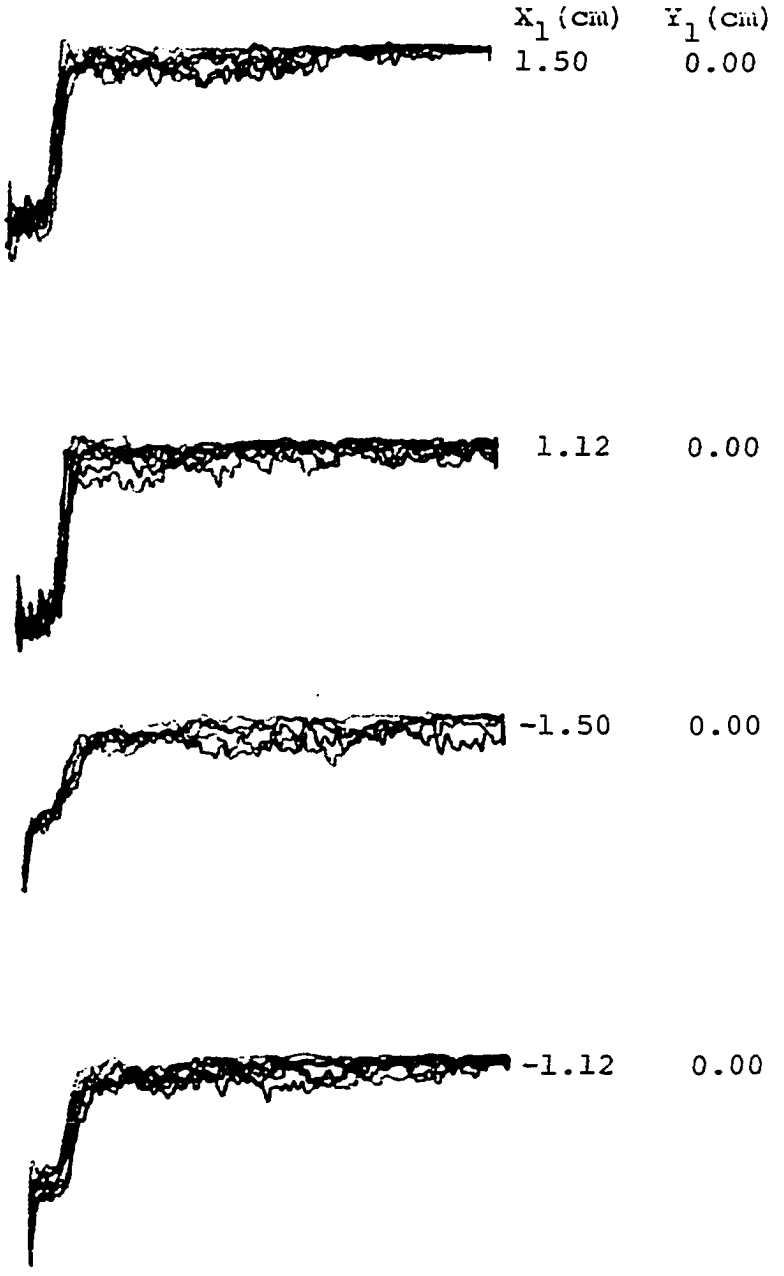

Figure B3. Boundary layer profiles of the three-dimensional obstacle at various X_1 and Y_1 positions (point source was present)

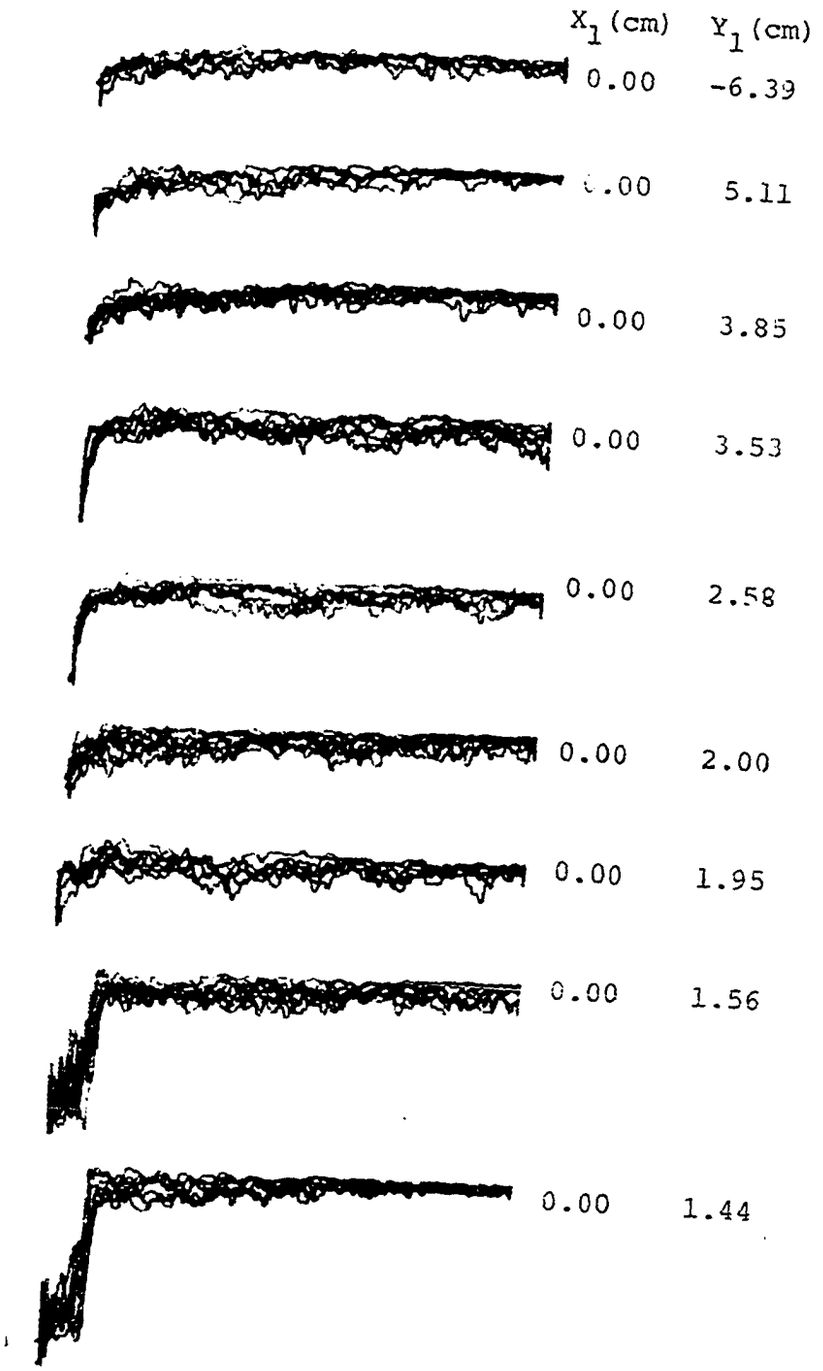

Figure B3 (Continued)

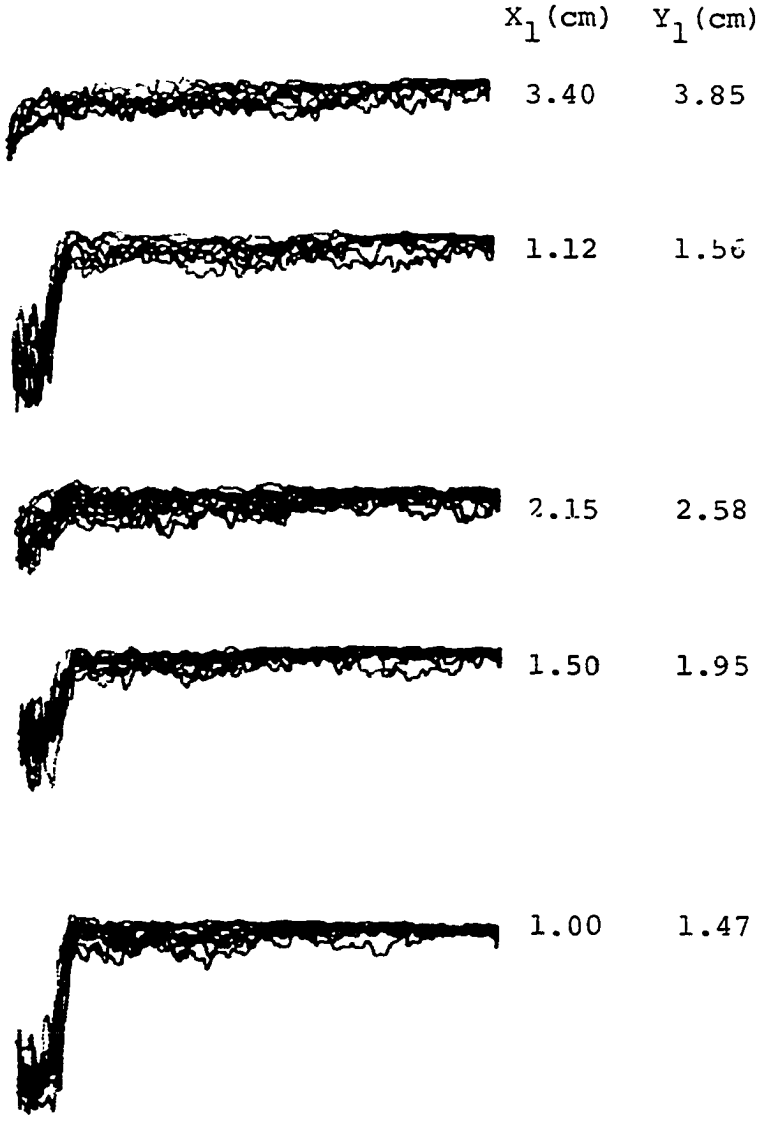

Figure B3 (Continued)

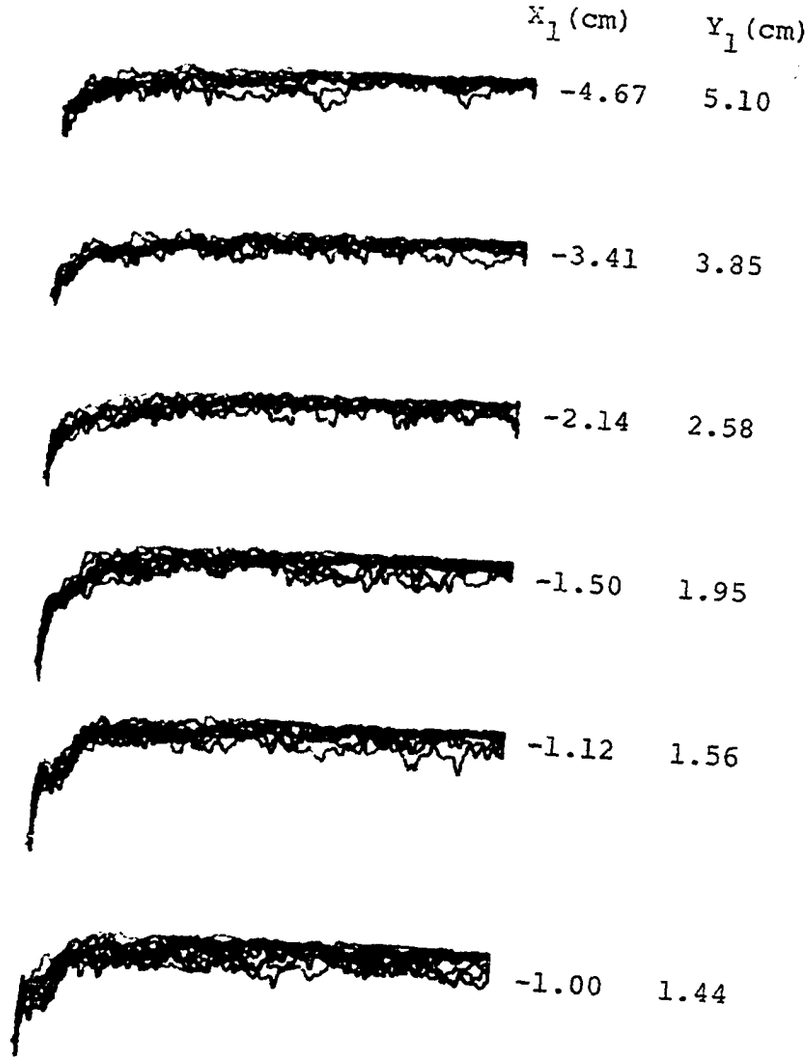

Figure B3 (Continued)

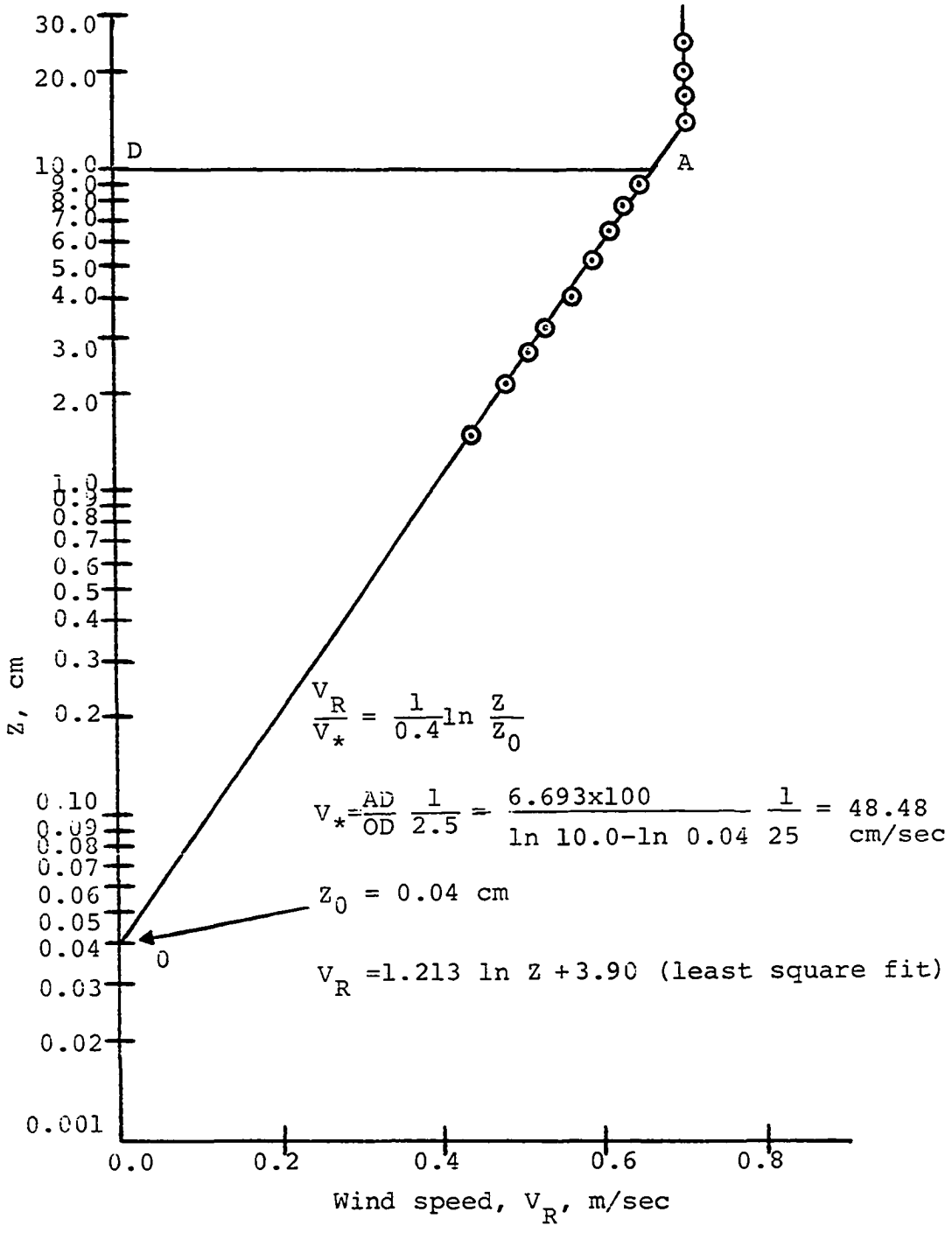

Figure B4. Test section wind profile at reference wind speed of 7.13 m/sec